Computed Tomography in the Modern Slaughterhouse

Mosbech, Thomas Hammershaimb

Publication date:
2011

Document Version
Publisher's PDF, also known as Version of record

Computed Tomography in the Modern Slaughterhouse

Thomas Hammershaimb Mosbech

Kongens Lyngby 2011
IMM-PHD-2011-258

Technical University of Denmark
Informatics and Mathematical Modelling
Building 321, DK-2800 Kongens Lyngby, Denmark
Phone +45 45253351, Fax +45 45882673
reception@imm.dtu.dk
www.imm.dtu.dk

IMM-PHD: ISSN 0909-3192

Abstract

The Danish pig meat industry has been seeing a growing international competition in the past years. In the quest to maintain both competitive prices and high product standards in spite of the higher Danish factor costs, a substantial effort is being put into innovation, research and development of technology. Recently, the use of X-ray computed tomography (CT) coupled with methods from image analysis has been introduced as a powerful means to optimise production, by providing detailed information on the raw materials. This thesis covers two aspects of the application of CT in the modern abattoir.

In the first aspect we use CT to analyse the biological diversity of carcass populations. The images form the basis for a data-driven tissue deformation model. The results provide valuable input to assist the development of an automated robotic tool for trimming the rind off pig backs.

The second aspect concerns measurements of each single carcass, to improve the raw material utilisation by individually adapted processing. Measurements performed online in the abattoir demand fast, robust and cost-effective imaging. We propose a tomographic reconstruction algorithm, enabling a substantial reduction of the subject-specific X-ray data needed to produce high quality images for accurate measurements. This is very beneficial for the abattoirs, as a reduction in acquired data translates directly into higher speed and a lower cost.

The thesis demonstrates the great potential of CT as a technology for improving the yield of the Danish pig meat industry. An introduction of efficient online CT will especially open a vast number of possibilities for optimising the production.

Resumé

Den danske svinekødsproduktion har været under hårdt pres fra udenlandske konkurrenter i den seneste tid. For at kunne opretholde konkurrencedygtige priser og høje produktstandarder, på trods af de højere danske produktionsomkostninger, har man satset solidt på innovation, forskning og udvikling af teknologi. I den forbindelse har man for nyligt rettet blikket mod røntgen computer tomografi (CT) som et middel til at forbedre produktionen via detaljeret viden om råmaterialerne. Denne afhandling omhandler to forskellige anvendelser af CT i det moderne slagteri.

Først ser vi på anvendelsen af CT til at undersøge biologisk diversitet i slagtekroppe. Således danner billeder grundlaget for en statistisk analyse af vævsdeformation. De opnåede resultater er yderst værdifulde i forbindelse med udviklingen af en maskine til automatisk afsværing af svinekamme.

Dernæst flyttes fokus til målinger udført på hver enkelt slagtekrop direkte i selve slagteriet. Med en sådan teknologi, kan forarbejdningen tilpasses den enkelte slagtekrop og dermed forbedre udnyttelsen af råmaterialerne. Denne type målinger kræver en hurtig, hårdfør og omkostningseffektiv billedteknologi. Vi udvikler en algoritme til effektiv tomografisk billeddannelse. Metoden gør det muligt at sænke den mængde røntgen data, som er nødvendig for at skabe billeder af høj kvalitet og dermed foretage nøjagtige målinger. Dette er yderst gavnligt for slagterierne, da en reducering af optaget data betyder højere hastighed og lavere driftsomkostninger.

Afhandlingen demonstrerer et stort potentiale i CT som en teknologi, der kan forøge afkastet for de danske svinekødsproducenter. Ved at indføre CT på slagtelinjen åbnes der for en lang række nye muligheder for optimering af produktionen.

Preface

This thesis was prepared at the Image Analysis and Computer Graphics group at DTU Informatics and submitted to the Technical University of Denmark (DTU), in partial fulfilment of the requirements for the degree of Doctor of Philosophy, Ph.D., in Informatics and Mathematical Modeling. The project was funded by DTU, the Danish Meat Association and the ITMAN Graduate School programme.

The work herein represents selected parts of the research work carried out in the Ph.D. period. The thesis consists of four research papers and an introductory part containing background information and an overview of the contributions.

The work was carried out in a close collaboration with the Danish Meat Research Institute of the Danish Technological Institute (previously of the Danish Meat Association) in Roskilde, Denmark. Part of the research was conducted at the Case Western Reserve University, Cleveland, Ohio, USA, under the supervision of Professor Daniela Calvetti and Professor Erkki Somersalo. The project was supervised by Professor Bjarne Kjær Ersbøll and Professor Rasmus Larsen, both DTU Informatics, and by Senior Researcher, Ph.D. Lars Bager Christensen, Danish Meat Research Institute.

Kgs. Lyngby, April 2011
Thomas Hammershaimb Mosbech

List of Published Papers

Listed here are the scientific publications prepared during the course of the Ph.D. program. The publications included in part II of the thesis are referred to by their respective chapter number.

Journal papers:

Ch. 9 [**77**] T. H. Mosbech, D. Calvetti, E. Somersalo, L. B. Christensen, B. K. Ersbøll. BASE-CT: Bayesian Adaptive Structure Enriched Computed Tomography. *Society for Industrial and Applied Mathematics, SIAM Journal on Imaging Sciences.* (Submitted, April 2011).

Conference papers:

Ch. 10 [**47**] M. F. Hansen, T. H. Mosbech, H. Ólafsdóttir, M. S. Hansen, R. Larsen. Can anisotropic images be upsampled? *5th International Conference on Computer Vision Theory and Applications, VISAPP.* 2010.

Ch. 8 [**78**] T. H. Mosbech, B. K. Ersbøll, and L. B. Christensen. An Efficient Data-driven Tissue Deformation Model. *IEEE 12th International Conference on Computer Vision, ICCV, 3DIM Workshop.* 2009.

Ch. 7 [**79**] T. H. Mosbech, B. K. Ersbøll, and L. B. Christensen. Quantification and validation of soft tissue deformation. *Society of Photo-Optical Instrumentation Engineers, SPIE Medical Imaging.* 2009.

Papers published outside the theme of the thesis are listed below:

[**40**] L. Frederiksen, K. Højlund, D. M. Hougaard, T. H. Mosbech, R. Larsen, A. Flyvbjerg, J. Frystyk, K. Brixen and M. Andersen. Testosterone therapy decreased subcutaneous fat and adiponectin in ageing men. *European Journal of Endocrinology.* (Submitted, March 2011).

[**80**] T. H. Mosbech, K. Pilgaard, A. Vaag, and R. Larsen. Automatic Segmentation of Abdominal Adipose Tissue in MRI. *17th Scandinavian Conference on Image Analysis, SCIA 2011.* (Accepted for publication).

[**95**] K. Pilgaard, T. H. Mosbech, L. Grunnet, H. Eiberg, G. Van Hall, E. Vallentin, T. Larsen, R. Larsen, P. Poulsen, A. Vaag. Differential non-genetic impact of birth weight versus 3rd trimester growth velocity on glucose metabolism and abdominal adiposity as determined by magnetic resonance imaging in young healthy twins. *Journal of Clinical Endocrinology & Metabolism, JCEM.* (Accepted for publication).

Co-authors of the publications in Part II and their affiliations are listed below in alphabetical order.

- DANIELA CALVETTI
  Department of Mathematics, Case Western Reserve University, Cleveland, Ohio, USA.
- LARS BAGER CHRISTENSEN
  Danish Meat Research Institute, Roskilde, Denmark.
- BJARNE KJÆR ERSBØLL
  DTU Informatics, Technical University of Denmark, Lyngby, Denmark.
- MADS FOGTMANN HANSEN
  DTU Informatics, Technical University of Denmark, Lyngby, Denmark.
- MICHAEL SASS HANSEN
  DTU Informatics, Technical University of Denmark, Lyngby, Denmark.
- RASMUS LARSEN
  DTU Informatics, Technical University of Denmark, Lyngby, Denmark.
- HILDUR ÓLAFSDÓTTIR
  DTU Informatics, Technical University of Denmark, Lyngby, Denmark.
- ERKKI SOMERSALO
  Department of Mathematics, Case Western Reserve University, Cleveland, Ohio, USA.

Acknowledgements

First and foremost, I would like to thank all current and former colleagues of the Image Analysis and Computer Graphics Group at DTU Informatics, for providing an inspiring working environment; spawning both friendships and collaborations. On this note, a special thank you goes to the other members of the first floor Image Group-outpost, for creating such a unique atmosphere.

I would also like thank my supervisor at DTU Informatics, Professor Bjarne Kjær Ersbøll, for his encouraging guidance and supervision throughout the project.

A warm thank you goes to the staff of the Danish Meat Research Institute in Roskilde, especially to my co-supervisor Lars Bager Christensen, for a productive collaboration with his great enthusiasm and interest in my work.

I thank Professor Daniela Calvetti and Professor Erkki Somersalo for their kind hospitality during my stay at Case Western Reserve University. I am grateful for our fruitful collaboration. I would also like to thank Jing Qin for her company as a fellow prisoner of Yost Hall.

Finally, I thank Mark Lyksborg and Jacob Lercke Skytte for spending their valuable spare time during a sunny weekend in April to proofread my thesis.

Contents

Part I

Summation

Chapter 1

Introduction

In 2009 19.3 million pigs were slaughtered in Danish abattoirs. This corresponds to 1.9 million tonnes of pig meat, of which 90% was exported to more than 100 countries all over the world. The export of pig meat products amounts to 26.6 billion DKK, accounting for almost half the value of the Danish agricultural export and 5% of the total Danish export [35].

The Danish pig meat industry has established itself as a worldwide leader, well known for its high standards. However, with this export-oriented profile, the industry is under constant pressure, to remain globally competitive with respect to quality, product safety and price. A current challenge is to maintain both competitive prices and product standards, in spite of the high factor costs of Denmark.

Figure 1.1 shows the distribution of cost and profit of the Danish production of pigs. The two most dominant items are raw materials and production wages. Reducing the price paid for the raw materials (the pigs) is not desired, as the slaughterhouses are owned by the Danish pig producers themselves. Instead, it is of great interest to optimising the utilisation of the raw materials. In 2005 the wages of British and German slaughterhouse workers were half of the Danish, with similar level of productivity [96]. An angle of approach, to minimise the expenses, is therefore to reduce the use of manual labour in the production, e.g. by automation.

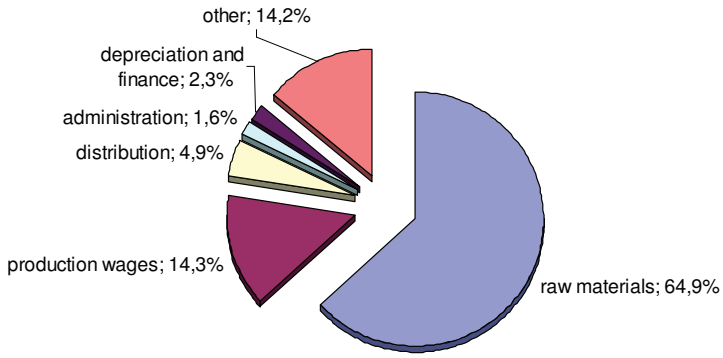

Figure 1.1: Distribution of cost and profit of the Danish production of pigs. Chart courtesy of Kjærsgaard [67].

Innovation, research and development of technology has for long been a successful means to achieve these goals [53]. The work is carried out by the Danish Meat Research Institute (DMRI). The unit was founded in 1954, owned by the industry organisation of Danish slaughterhouses, an ownership structure giving rise to a close collaboration with the pig producers. In late 2009 DMRI merged into the Danish Technological Institute. However, a key focus area remains the development of methods and technologies for efficient production of safe meat products of a high quality at competitive prices [5].

Handling raw materials with natural biological variation in the industrial environment of modern abattoirs is a difficult task. Moreover, the process is *reversed* in comparison to e.g. car factories, where products are assembled from the materials. In the slaughterhouse the inhomogeneous carcasses are cut apart to form homogeneous products. Optimising this procedure therefore demands knowledge of the raw materials. Both information regarding the biological variation across populations and each individual pig is of interst.

In modern abattoirs, existing equipment characterises carcasses by weight and a prediction of the lean meat percentage (LMP). The latter is estimated by AutoFom [16, 21] performing ultrasound (US) measurements along the back of the pig. These measurements are carried out online in the abattoir, and form the basis for the sorting of carcasses for differentiated processing. However, the LMP estimate contains a large degree of uncertainty, given its global nature. It fails to provide any direct measures of the local carcass composition, e.g. size of specific muscles. Information, that could be used to gain a better utilisation

of raw materials, as shown in [67].

To address these shortcomings, DMRI turned towards the use of non-invasive imaging by X-ray computed tomography (CT) [65]. The well-known medical imaging modality can provide highly detailed three-dimensional images of the inner structures of carcasses. Furthermore, CT images enable a clear distinction between the tissue types of interest in the abattoir; bone, fat and meat.

In 2004 DMRI acquired their first CT scanner. The scanner had previously been used by a hospital, and was installed in a trailer for direct attachment to the slaughterhouses. In 2006 the Virtual Slaughterhouse project (VSH) was launched in collaboration with DTU Informatics and other parties. VSH demonstrated the applicability of CT and methods from image analysis in the context of the abattoir [29, 48, 116].

The work in VSH included methods for accurately measuring both local and global carcass composition for classification and optimal sorting, as well as analysis and modelling of biological variation in relation to the design of tools for automated processing. These valuable results opened the door for future work in many aspects; this thesis stands on the shoulders of VSH in continuing the development of new applications of CT to improve the abattoirs.

1.1 Objectives

The overall goal of the thesis is to investigate and develop applications combining CT and methods from image analysis for optimising production in the modern abattoir. The specific objectives are:

- To analyse the biological diversity of pig carcasses by data-driven statistical modelling of tissue deformation, in relation to the design of automated processing tools.

- To develop an efficient algorithm for CT image reconstruction. Providing fast, robust and cost-effective imaging equipment for accurate measurements of carcasses performed online in the abattoir.

1.2 Thesis Outline

The thesis consists of two parts. Part I introduces and summarises the work carried out during the Ph.D. program. Part II contains a selection of the scientific publications prepared. As the papers document the work in a self-contained fashion, overlap occurs between the two parts.

Part I

Chapter 2 gives an introduction to the background and perspectives of the work, introducing online CT and aspects of automation in the abattoirs.

Chapter 3 introduces concepts of tissue deformation modelling, and provides an overview of an image-based statistical method.

Chapter 4 reviews foundations of the CT imaging modality. Methods from statistical inversion are presented in the context of tomographic image reconstruction. The chapter also presents a method for enhancing anisotropic slice-based images.

Chapter 5 gives a summary of the results of part II and the main contributions of the thesis.

Chapter 6 contains a discussion of the contributions in relation to the objectives as well as future work. Finally, the chapter concludes the thesis with some closing remarks.

Part II

Chapter 7 describes the use of CT for image-based modelling of soft tissue deformation in pig backs. Deformation induced by a known external source is quantified by steel markers inserted into the tissue. The movement of the steel markers is parameterised to form the basis of a statistical model. The empirical model is built using principal component analysis, and is successfully validated using leave-one-out cross-validation by subject.

Chapter 8 uses the data-driven tissue deformation model of chapter 7 to analyse specific muscle movement in the pig back. The deformation explained by specific modes of the model is isolated and compared to relevant measurements of carcass composition. We find a useful association between lateral muscle movement and a ratio of meat-fat quantity.

Chapter 9 presents an algorithm for CT image reconstruction from a reduced amount of X-ray data. The reconstruction is formulated in a Bayesian

framework, allowing for convenient augmentation of the sparse data by means of an adaptive prior. The image is estimated as the most probable realisation, and the uncertainty can be assessed with random sampling. The performance is illustrated by phantom data and two measurements of carcass composition.

Chapter 10 addresses anisotropy in slice-based three-dimensional imaging. An image function of cubic B-splines is fitted to the slices, while accounting for their thickness to handle the partial volume effect. The proposed method is inspired by registration-based interpolation, but extends the concept by penalising lines of correspondence featuring image gradients. A phantom data example shows promising results.

1.3 Abbreviations

ART	Algebraic Reconstruction Technique
BASE-CT	Bayesian Adaptive Structure Enriched Computed Tomography
CGLS	Conjugate Gradient method for Least Squares
CI	Cubic Interpolation
CT	X-ray Computed Tomography
DMRI	Danish Meat Research Institute
DTU	Technical University of Denmark
FBP	Filtered Back Projection
HU	Hounsfield Units
LMP	Lean Meat Percentage
MAP	Maximum a Posteriori
MCMC	Markov Chain Monte Carlo
MIP	Maximum Intensity Projection
MRI	Magnetic Resonance Imaging
MSE	Mean Squared Error
PCA	Principal Component Analysis
RBF	Radial Basis Function
RBI	Registration-based Interpolation
ROI	Region of Interest
TV	Total Variation
UP	Upsampling
UPWP	Upsamping With Prior
UPNP	Upsamping with No Prior
US	Ultrasound
UTS	Uniform Tensor Splines
VSH	Virtual Slaughterhouse

Chapter 2

Background

This chapter serves to provide a background and perspective of the work of the thesis; automation in the abattoirs and the use of online CT in this context.

2.1 Automating Abattoirs

The international competition in the meat industry has moved the processing from small local facilities into large centralised slaughterhouses. This development has stressed to the limit traditional manual slaughtering techniques, which would lead to physically demanding and repetitive procedures in the new labour-intensive industrial working environment.

Since 1998, DMRI has taken part in a large scale program for automating abattoirs, with the strategy to achieve a higher production efficiency combined with a better working environment. The latter can be achieved by replacing the most arduous work with automated processing. Furthermore, the reduction in manual handling can improve the hygiene and thereby the food safety; reducing the risk of spreading bacteria, as the equipment can be sterilised more effectively between each carcass. This ongoing program has covered 30 development projects with a budget exceeding 40 million EUR [83].

Several advanced innovative tools have been successfully implemented for the slaughter line, carcass cutting and boning procedures [34, 46, 53, 83], also demonstrating an improvement in raw material utilisation, as a high level of precision and repeatability of the machinery enhances the product yield. Given the size of the production, even the smallest improvement can lead to large profits.

The design of automated tools for the abattoir is a highly complex task, qua the inherent diversity of the raw materials. Previously, a trial-and-error approach has been favoured in the development; making adjustments on the basis of tests performed on a limited number of subjects (Figure 2.1).

Figure 2.1: Trial-and-error; designing a tool for trimming the fat layer on pig backs to a given thickness. Image courtesy of DMRI.

However, designing cutting tools in this iterative manner is inefficient. Comparing adjustments can be hard, since the procedures by definition are destructive. This way it is difficult to validate the performance of a tool across the entire population.

A solution to this is to resort to methods for modelling the variability in the carcasses, and including this information to optimise the design phase and to assess the performance. As part of VSH, Erbou et al. [31] demonstrated CT-based tool development through studies of biological variation in bones.

Part of this thesis continues along this path of using CT for modelling biological variation of pig carcasses. We consider the development of an automatic cut-

ting tool for pig backs to produce bacon with a given fat layer thickness. The transition between fat and meat is far from smooth and highly variable between carcasses, thus a robot trimming the fat layer must be able to adjust accurately (Figure 2.2). The corresponding manual procedure is physically demanding and repetitive; the rind layer is repeatedly trimmed and measured until the wanted thickness is achieved.

(a) (b)

Figure 2.2: Volumetric model of a pig back created from a CT scan. (a) Model distinguishing between the loin and streaky (top) and the rind (bottom). (b) 'Virtual cut' showing only the rind; the variation of the contours in the transition is evident. From chapter 8.

Moreover, the yield can be improved by accurately automating the cutting; if too much fat is cut off, the slaughterhouse loses profit as the product is sold by weight and an established target percentage of fat and meat, and meat is more valuable than fat. On the other hand, trimming too little fat will result in dissatisfied customers and possible losses in future sales. Furthermore, trimming the fat layer in one piece, results in less waste as it makes the fat valuable as a separate by-product.

Figure 2.3 shows a conceptual drawing of such a tool. The machine consists of cylinders pulling the meat towards a fixed horizontal knife, which trims the rind. The amount to be cut off is controlled by a series of stamps pressing onto the skin surface.

Initial stages of the development process have identified the need for information on the tissue deformations caused by handling the pig back. Lateral movement in the loin muscle has been observed, making it difficult to perform accurate cuts (Figure 2.1).

This is the theme of chapters 7 and 8, where we combine CT images with statistical methods to develop a data-driven tissue deformation model to aid the tool design.

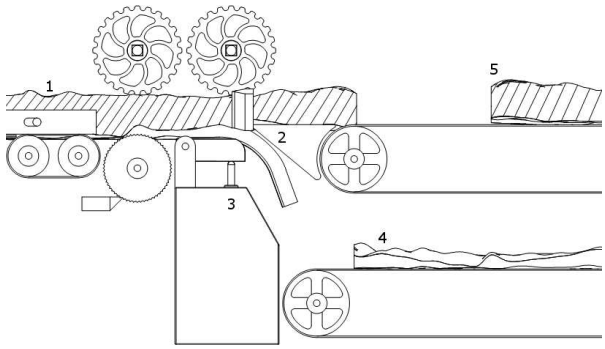

Figure 2.3: Conceptual drawing of the machine for trimming the fat layer on pig backs to a given thickness. Main items are labelled with numbers. 1; unprocessed pig back, 2; horizontal knife, 3; stamps, 4; excess fat, 5; processed pig back. From chapter 7.

2.2 Online CT

Figure 2.4 illustrates the future vision for the abattoir: Each carcass is CT scanned, and methods from image analysis are used to determine carcass composition. The measurements form the basis of determining the optimal use, but the decission is also based on current orders, market demand and prices. The determined optimal partitioning is then passed to the robotic tools for automated processing, adapting to the individual carcass to produce end products with less variability.

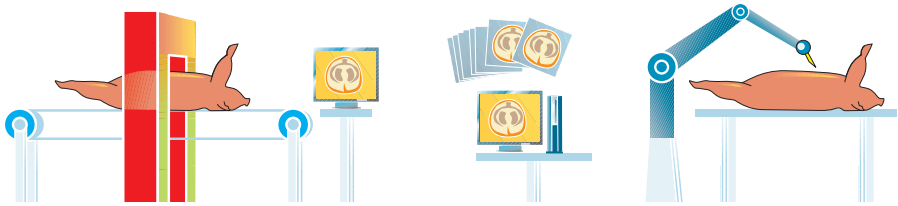

Figure 2.4: Online CT in the abattoir; a combination of CT scanning equipment, software for image analysis, and automated cutting tools. Illustration courtesy of *Ingeniøren* [43].

In VSH, Hansen et al.[49, 50] demonstrated the use of *virtual cuts* as part of predicting the optimal utilisation. As mentioned above, efficient tools have already been developed for automation. Several of these existing facilities have

been designed to be able to adapt to each individual carcass, and benefit from any additional information extracted from the CT images.

In comparison with the existing US-based equipment, used for estimating the LMP [21], CT can provide information with a much higher level of detail. US forms images by measuring the reflection of sound waves in layers between different tissues [60]. In the abattoir, US has a low running cost and the equipment is robust enough to handle the environmental conditions and capacity requirements. But the modality is limited by the depth penetration, and US images are difficult to interpret automatically.

However, scanning carcasses online with the existing medical CT scanner of DMRI is not feasible. It is too expensive, too slow and not robust enough. Recent technological advance has cleared the way for the next step in extending VSH within the field of automation: To develop and implement a robust, cost-effective CT scanner, functioning online under the aggressive environmental conditions and capacity requirements, found in a Danish pig slaughterhouse.

This forms the background of chapters 9 and 10, where we consider efficient online CT image acquisition, suitable for the high speed and high productivity tools in the modern abattoir.

Chapter 3

Tissue Deformation Analysis

This chapter provides an introduction and a brief overview of methods for modelling tissue deformation, related to the papers in chapters 7 and 8. Specific choices are made based on the objectives of the work; to analyse the deformation of soft tissue in pig backs, in relation to designing an automatic cutting tool.

3.1 Introduction

The concept of modelling soft tissue deformation has been, and currently is, subject to extensive studies. Many of the applications are related to the field of medical imaging:

In virtual reality surgery for training simulators, to create three-dimensional biomechanics and physical models of organs and tissue to provide realistic feedback to haptic devices used in operation room-scenario simulations [27, 28, 70, 111].

In robotic and robot-assisted methods for minimally invasive surgery, where it is important to incorporate knowledge of tissue deformation in order to have

correct motion compensation and stabilisation during operations [10, 55, 85, 110, 114].

In general studies of tissue properties and behaviour when exposed to external mechanical loading, e.g. related to patients developing pressure sores and optimal seat cushion design [14, 15, 72, 91, 113].

Several of these facets are also relevant in industrial automation; prediction of subject behaviour during handling can be valuable, when machinery is interacting with deformable materials.

For modelling soft tissue deformation, a popular choice is physically-founded models based on continuum mechanics, e.g. finite element methods. Famaey and Sloten [32] present an extensive overview of variants of such models, discussing their different properties.

An alternative to the physics-based approach, is the use of basis functions to model the tissue deformation — a technique related to non-rigid image registration [3, 37, 103]. Here, the deformations are parameterised by warp functions, formed as a linear combination of smooth basis functions defined in knot points. Wachowiak et al. [117] applies such methods for simulation of needle insertion in prostate brachytherapy.

The finite elements models use material constants to model the biomechanical properties of the tissue, whereas the non-physical models can control deformation behaviour by the choice of basis functions and their weights in the linear combination. For both types of models, parameters are often estimated by experiments; monitoring tissue deformation induced by external forces in a controlled environment, e.g. by a tracked surgical instrument or compression tests with indenters [1, 112]. For the experiments, imaging techniques can provide accurate measurements of the tissue deformation, as described in the next section.

3.2 Image-based Tissue Modelling

Different methods have previously been applied for *image-based* tissue modelling:

Tada et al. [112] present a method based on three-dimensional magnetic resonance imaging (MRI) and an iterative finite element simulation, updating the material constants to match the observed deformation of a rubber phantom.

In [42] texture correlation and three-dimensional MRI was used to monitor the deformation *in vivo*. However, this method was reported sensitive to out-of-plane tissue displacements, variation in imaging conditions and change in tissue properties between images due to the load.

The PhD thesis of Hu [57] describes experiments performed on liver tissue for finite element modelling. The methods used include digital photography of dye markings on the tissue surface, as well as two orthogonal 2D X-ray images for tracking steel markers inserted into the liver *ex vivo*.

Altamar et al. [1] monitored soft tissue deformation in saline perfused kidneys through displacement of physical markers. In their study, glass beads were sutured to the surface of porcine kidneys subject to incision. The marker displacements were then tracked through pre- and post-deformation CT to assess predictive capabilities of their model.

For the specific application in this thesis, we use a non-physical representation of the tissue deformation by means of basis functions. The parametric representation is coupled with image-based experiments; tissue deformation induced by a pressure stamp, and monitored in three dimensions using CT images and steel markers inserted into the tissue to form accurate landmarks (Figure 3.1). These fiducial markers are used under the assumption, that the marker displacements observed between the two images represent the soft tissue deformation at the given location. The next section describes the parameterisation.

3.3 Representation by Basis Functions

Consider two point sets of size n in $d = 3$ dimensions; $\mathcal{P}$ and $\mathcal{Q} \in \mathbb{R}^{n \times d}$, holding corresponding marker positions retrieved from the two CT images acquired without and with deformation induced, respectively.

The parameterisation of the displacements between the two point sets, can be regarded as a task from point-based registration; determining a geometrical transformation aligning corresponding points by estimating their displacements. The alignment of a point pair $\mathbf{p}_i \in \mathcal{P}$ and $\mathbf{q}_i \in \mathcal{Q}$ is defined as a function ϕ of parameters $\mathbf{X} \in \mathbb{R}^{d \cdot n_k}$

$$\phi(\mathbf{p}_i, \mathbf{X}) = \mathbf{p}_i + \mathbf{u}(\mathbf{p}_i, \mathbf{X}), \tag{3.1}$$

modelling the displacements by the parametric transformation $\mathbf{u} : \left(\mathbb{R}^d, \mathbb{R}^{d \cdot n_k}\right) \rightarrow \mathbb{R}^d$.

In medical imaging applications, such as guidance systems for surgery, point-

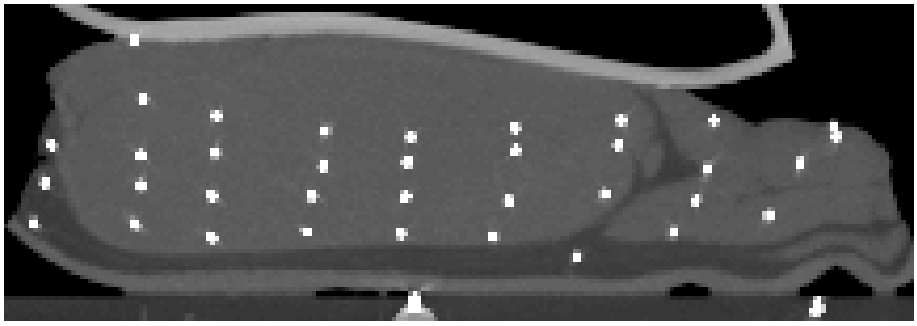

(a)

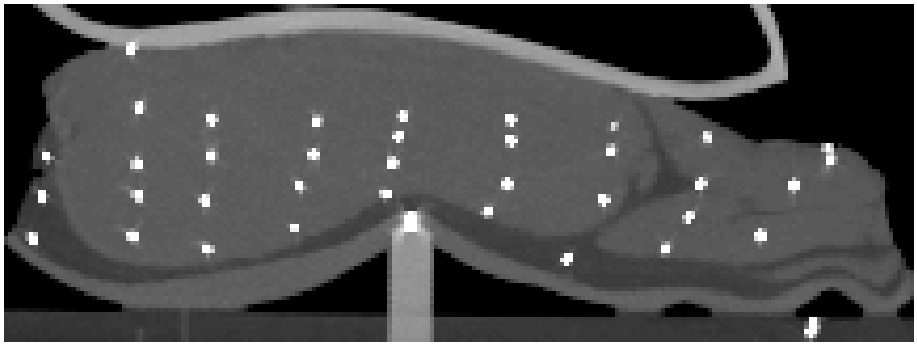

(b)

Figure 3.1: Image-based tissue modelling; three-dimensional CT images of tissue with steel markers inserted to quantify deformation from pressure applied onto the skin surface. (a) and (b) show the same subject before and after induced deformation. Images from chapter 7.

based registration can be used to align image pairs with a rigid transformation of fiducial markers [33]. But, in order to capture the nature of the soft tissue deformation, we turn to non-rigid transformations, which are also related to medical image registration [3, 37, 103].

The transformation is composed of a sum of basis functions ψ defined on a set of knot points $\mathcal{C} \in \mathbb{R}^{n_k \times d}$ all within the spatial range of $\mathcal{P}$ and $\mathcal{Q}$. With this, the displacement estimate of a single point in one direction, $u : (\mathbb{R}, \mathbb{R}^{n_k}) \to \mathbb{R}$, is represented as a sum of n_k basis functions with weighting parameters $\mathbf{x} \in \mathbb{R}^{n_k}$

$$u(\mathbf{p}_i, \mathbf{x}) = \sum_{j=1}^{n_k} x_j \psi(r_j), \tag{3.2}$$

where $r_j = \|\mathbf{p}_i - \mathbf{c}_j\|$ is the Euclidean distance between the point $\mathbf{p}_i$ and knot $\mathbf{c}_j \in \mathcal{C}$.

We consider a radial basis function (RBF) $\psi_{d,k} \in C^{2k}(\mathbb{R})$ as introduced by Wendland [119]. In dimension $d = 3$ with different degrees of smoothness $k = 0 \dots 2$, the functions are defined as univariate polynomials [36]

$$\psi_{3,0} = (1 - r)_+^2 \tag{3.3}$$

$$\psi_{3,1} = (1 - r)_+^4 (4r + 1) \tag{3.4}$$

$$\psi_{3,2} = (1 - r)_+^6 (35r^2 + 18r + 3), \tag{3.5}$$

with with compact support enforced as

$$(1 - r)_+^l \begin{cases} (1 - r)^l & \text{for } 0 \leq r \leq 1 \\ 0 & \text{for } r > 1 \end{cases}. \tag{3.6}$$

A scaling factor of the locality $a > 0$ can be applied as $\psi(r) \equiv \psi(r/a)$. The compact support makes the Wendland functions suitable to capture local tissue deformations. This is opposed to basis function with global influence, such as thin plate splines and multiquadratics [13, 73].

For n all pairs in $\mathcal{P}$ and $\mathcal{Q}$, regarding a single dimension of the deformation, the vector of parameters $\mathbf{x}$ is determined by minimising a sum of n squared pair-wise Euclidean distances between observations and estimates

$$\underset{\mathbf{x}}{\operatorname{argmin}} \sum_{i=1}^{n} \|\mathbf{q}_i - (\mathbf{p}_i + u(\mathbf{p}_i, \mathbf{x}))\|^2. \tag{3.7}$$

Corresponding to the least squares solution of

$$\mathbf{q} = \mathbf{p} + \mathbf{A}\mathbf{x}, \tag{3.8}$$

where $\mathbf{p}, \mathbf{q} \in \mathbb{R}^n$ and $\mathbf{A}$ is an $n \times n_k$ matrix of basis function values $\{A\}_{ij} = \psi_{d,k}(||\mathbf{p}_i - \mathbf{c}_j||)$.

Considering displacements in all $d = 3$ dimensions can then be expressed as

$$\mathbf{q} = \mathbf{p} + \begin{bmatrix} \mathbf{A} & \mathbf{0} & \mathbf{0} \\ \mathbf{0} & \mathbf{A} & \mathbf{0} \\ \mathbf{0} & \mathbf{0} & \mathbf{A} \end{bmatrix} \mathbf{X} = \mathbf{p} + \mathbf{A}_0\mathbf{X}, \tag{3.9}$$

with point coordinates and parameters concatenated dimension-wise $\mathbf{p}, \mathbf{q} \in \mathbb{R}^{d \cdot n}$ and $\mathbf{X} \in \mathbb{R}^{d \cdot n_k}$. With proper scaling of the support and positioning of the knot points, the kernel matrix is likely to be sparse, which can be utilised for efficient parameter estimation and computation of interpolants.

The parametric representation of the observed marker displacements enables interpolating between the markers to form a displacement field — for visualisation and analysis of the tissue deformation. Using the same knots as before, a new matrix of the same structure as $\mathbf{A}_0$ is computed with respect to the new points of interest (e.g. a regular grid structure or simply all voxel positions) and plugged into (3.9) along with the parameters estimated from the displaced markers (Figure 3.2).

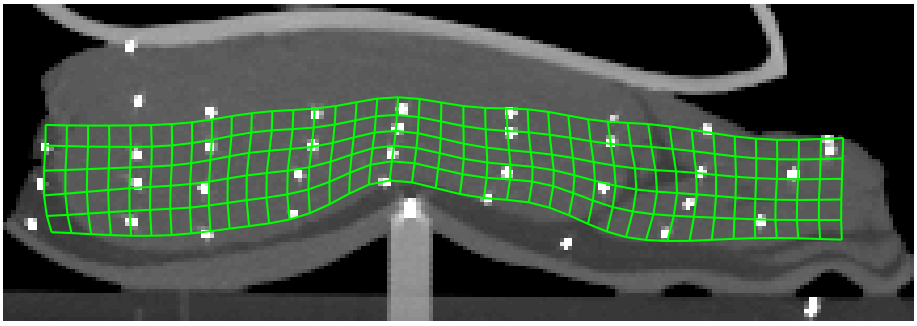

Figure 3.2: Interpolation of tissue deformation as a displacement field; a regular grid of points deformed with parameters estimated from the observed marker displacement seen in Figure 3.1. From chapter 7.

For interpolating tissue deformation between the markers, kriging is an alternative to the parametric representation above [26, 68]. This method originates in geostatistics, and is used for description and interpolation of irregularly sampled spatial data. In comparison to interpolation by kriging, parameterisation by RBFs, can provide a large reduction in dimensionality. Using RBFs, only three weighting coefficients are needed for each knot, as opposed to three directions for each pixel in the deformation field.

When representing deformations by Wendland functions, a widespread approach is to use the marker points as knots [36, 37, 117]. This guarantees positive definiteness and thus solvability with respect to the parameters [119]. However, in our case of image-based tissue modelling, such representations would not allow for comparisons of different subjects, as no point correspondences exist between them. Therefore, it is beneficial to use a common set of knots for all subjects, e.g. positioned relative to the indentation stamp.

Using a higher number of knots, enables a higher level of accuracy for the parametric representation. Moreover, the positioning can also improve this. E.g. by a denser coverage of the area around the stamp — where more deformation is observed — at the expense of other regions. Hansen et al. [51] presented a dynamic refinement of the knot point mesh in the application of parametric image registration. However, considering the knot positions as additional variables in our deformation model, would magnify the dimensionality and affect the interpretability of the results. Instead we rely on a common regular grid structure across all subjects.

Conducting the same experiment on several subjects, the observed marker displacements are comparable by means of their parametric representation and the parameters — the basis funciton weights — can be used to build a data-driven tissue model using statistical methods.

3.4 Statistical Deformation Modelling

For modelling and analysing the tissue deformation observed in the experiments, we again turn our attention to methods related to image registration and medical imaging, where the application of statistical methods on deformation fields is well-known.

In 1998 Ashburner et al. [4] introduced *deformation-based morphometry*; applying multivariate statistics on sets of deformation parameters obtained from image registration, to characterise and quantify morphometric features.

With a principal component analysis (PCA) on the registration parameters of free-form deformations based on B-splines, Rueckert et al. [101] constructed a statistical model of deformations for brain-MRI, enabling studies of anatomical variability. A similar approach was applied in the work of Ólafsdóttir et al. [87], to describe difference in variation of craniofacial anatomy between groups of mice.

The concept of these methods is similar to the work on statistical shape analysis of Cootes et. al [23]; building a model of a class of shapes from a set of examples of this shape using PCA. Only, the shapes are represented by landmarks, whereas the deformations are represented by warp parameters.

Alternative approaches to PCA for extracting modes of variation with other properties exist, e.g. varimax rotation, independent component analysis and sparse PCA [31, 88]. For details on these methods, readers are referred to the literature e.g. [59, 63, 122], and comparisons described in the PhD theses of Ólafsdóttir [86] and Erbou [29].

By feeding the RBF parameters to a PCA, we seek to build a tissue deformation model, capturing the variability of the data set. Considering a set of N RBF parameter vectors $\mathbf{X}_s$, $s = 1, \cdots, N$. The mean and covariance of the deformations are estimated as

$$\bar{\mathbf{X}} = \frac{1}{N} \sum_{s=1}^{N} \mathbf{X}_s, \tag{3.10}$$

and

$$\mathbf{\Sigma} = \frac{1}{N-1} \sum_{s=1}^{N} (\mathbf{X}_s - \bar{\mathbf{X}})(\mathbf{X}_s - \bar{\mathbf{X}})^T. \tag{3.11}$$

With an eigenanalysis of $\mathbf{\Sigma}$, the resulting eigenvectors are gathered in an orthonormal matrix $\mathbf{P} = [\mathbf{P}_1 \mathbf{P}_2 \cdots \mathbf{P}_{d \cdot n_k}]$, ordered according to the size of the corresponding eigenvalues $\lambda_1 \geq \lambda_2 \geq \cdots \geq \lambda_{d \cdot n_k}$.

These *principal modes* $\mathbf{P}$ form the basis of a generative model; a new instance of the RBF parameters (within the space spanned by the observations) can be formed as the sum of the mean and a linear combination of eigenvectors with coefficients $\mathbf{b} \in \mathbb{R}^{d \cdot n_k}$

$$\mathbf{X} = \bar{\mathbf{X}} + \mathbf{P}\mathbf{b}. \tag{3.12}$$

The corresponding deformation field can then be computed with the appropriate $\mathbf{A}_0$-matrix as in (3.9).

This way, an observed deformation $\mathbf{X}_{\text{obs}}$ can be represented by means of $\mathbf{b}$, by projection into the new basis

$$\mathbf{b} = \mathbf{P}^T(\mathbf{X}_{\text{obs}} - \bar{\mathbf{X}}). \tag{3.13}$$

As the elements of $\mathbf{b}$ are linked to an orthonormal basis ($\mathbf{P}$), they can make it easier to isolate and interpret the observed variability in relation to certain features of interest. E.g. by *reconstructing* $\mathbf{X}$ only using a subset $\mathbf{P}'$ of the modes and parameters $\mathbf{b}'$ in the generative model

$$\mathbf{X} = \bar{\mathbf{X}} + \mathbf{P}'\mathbf{b}', \tag{3.14}$$

see Figure 3.3. For a model with a given set of eigenvectors included, the percentage of the total variance explained is proportional to the size of the corresponding eigenvalues.

When using this type of statistical deformation modelling, it is important to keep in mind, that the models are solely data-driven. Thus, they are only capable of spanning the variability present in the set of observations. This is especially important in relation to prediction; the observations must be representative of the population modelled.

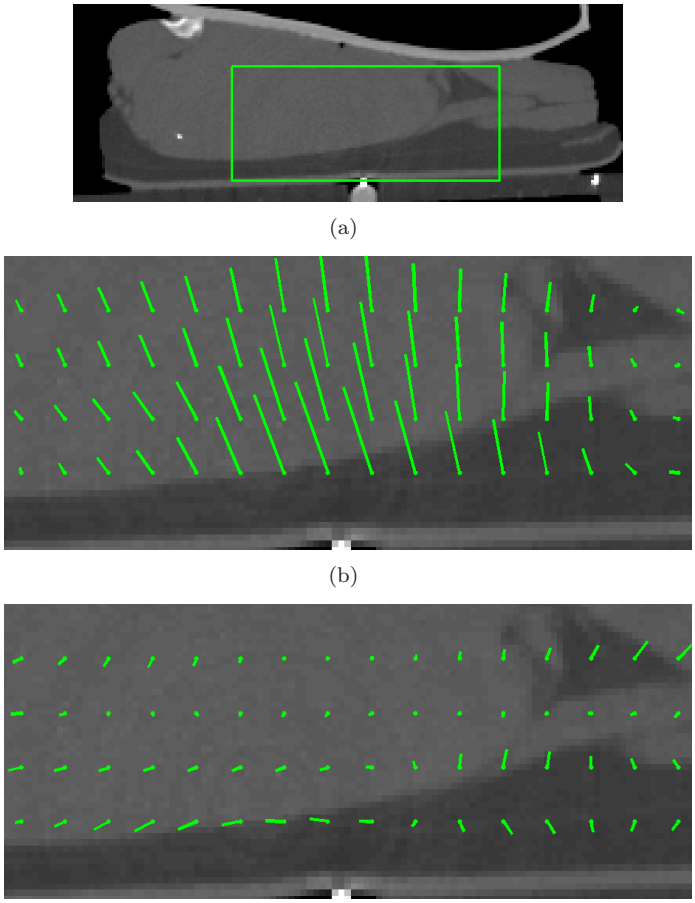

(a)

(b)

(c)

Figure 3.3: Displacements calculated for a grid of points using RBF parameters generated with (3.14), to illustrate the effect of single modes in the model. (a) The region of interest, the few high intensity pixels in the bottom are the pressure stamp tip. (b) Mean displacements. (c) Displacements reconstructed using only the first principal mode (without the mean and magnified); this mode corresponds to lateral movement in the left part of the image. From chapter 8.

Chapter 4

Image Reconstruction

Sections 4.1-4.4 of this chapter introduces concepts of CT image reconstruction, as used in the work presented in chapter 9. The fundamentals of the imaging modality are reviewed and in this context methods from statistical inversion are presented. The content is centred on the task of tomographic reconstruction from sparse X-ray projection data, with the targeted application being efficient image acquisition for on-line measurements in the abattoirs. Section 4.5 concerns a method for addressing anisotropy in slice-based three-dimensional images, as suggested in chapter 10.

4.1 Computed Tomography

X-ray CT is an imaging modality to acquire high contrast three-dimensional images of internal structures. The theoretical foundation was published by Cormack and Hounsfield in the 1960s and 1970s, and their pioneering work resulted in the 1979 Nobel Prize awarded jointly to the two [24, 25, 54, 92]. Since its introduction, CT has enjoyed vast popularity in a number of applications. For medical purposes, it is a well-known powerful examination tool, e.g. in diagnostics and monitoring of treatment. The modality is also used within the industry, applications include inspection for non-destructive studies and quality

control, e.g. in the timber industry, wind turbine production and manufacturing of aircraft components [2, 6, 104, 105].

CT reconstructs the absorption coefficients of the body at each spatial location from measured attenuations of X-rays having passed through the object from different directions. An X-ray, emitted from a *source*, traverses the object of interest and its strength on the opposite side is recorded as the number of photons hitting a *detector* (Figure 4.1). From a series of such measurements, CT produces an image with an estimate of the spatial distribution of the mass absorption coefficient function μ across a defined domain Ω. The concepts of the modality are well described in the literature, e.g. [65, 81, 82].

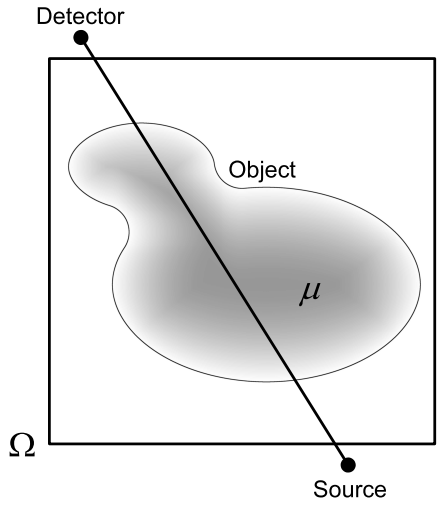

Figure 4.1: X-ray travelling from source to detector through the object of interest. The greyscale illustrates the mass absorption coefficient μ. The rectangle shows the image domain Ω. Illustration from chapter 9.

In the following, the CT problem is limited to two dimensions; a plane intersecting the object of interest. Given an X-ray of intensity I along a line passing through the object, the intensity attenuation dI which results when the ray travels along a segment $d\ell$ in a material with mass absorption $\mu \geq 0$, ignoring the effect of scattering and deflection of the ray from the material, can be described by the formula

$$dI = -I\mu d\ell. \tag{4.1}$$

An X-ray with initial intensity I_0 which has passed along the line segment L

through the object, reaches the detector with the intensity I given by

$$I = I_0 \exp\left(-\int_L \mu(p) d\ell(p)\right), \tag{4.2}$$

where $\mu = \mu(p)$ and $p \in \Omega$ (Figure 4.1). I_0 is estimated during scanner calibration by measuring the intensity of the ray at the detector when no object is present. This air scan also allows for compensation of detector sensitivity variation. The logarithmic transformation of the ratio of the intensities can be expressed as the integral of the mass absorption function

$$-\log\left(\frac{I}{I_0}\right) = -\int_{I_0}^{I} \frac{dI}{I} = \int_L \mu(p) d\ell(p). \tag{4.3}$$

From this ray attenuation model, the tomographic image reconstruction problem can be viewed as an integral geometry problem of estimating a function from values of line integrals through the domain of interest.

A full continuous set of integral values is referred to as the complete Radon transform data [98]. From this, it is possible to compute the unique mass absorption analytically. The method of choice for image reconstruction from such measurements is filtered back projection (FBP). FBP uses the classical theory of Radon and Fourier transforms of the integral data along with filtering to eliminate blurring, see e.g. [9, 62, 64].

The reconstructed attenuation coefficient map is calibrated against the Hounsfield scale; scaling the image intensities to Hounsfield Units (HU), such that attenuation of air receives HU -1000, and the attenuation of distilled water receives HU 0 [65].

In practice, the set of measurements will come from a finite number of source/detector pairs. In conventional CT scanners, the source and detector array are mounted on opposite sides of a gantry, rotating to acquire the sequence of projections from different directions. To reconstruct a single 512×512 pixel two-dimensional slice using FBP, modern medical CT scanners measure around 2 million rays [65].

Various geometrical set-ups exist for acquiring the projection data. In the early work, parallel-beam CT was considered using arrays of both sources and detectors. Later, this was replaced by fan-beam CT; a fan-shaped beam emitted from a single point source and measured in an array of detectors. The latter is chosen here, as only one source is needed to acquire the projection. Figure 4.2(a) illustrates the concept.

Recent technological advance in the development of X-ray tubes have spawned stationary source acquisition techniques [120], where multiple sources and detectors are located at fixed positions around the object. An advantage of this method is that it does not require gantry motion, instead switching rapidly among the sources, each one creating a fan-projection of the object from a different angle. The elimination of mechanical motion enables a faster and more robust set-up, especially suitable for handling high throughput of industrial applications. With this stationary set-up, it is also possible to speed up the process by acquiring simultaneous projections from multiple views with non-overlapping fans [121].

An increase in number of detectors does not change the radiation dose, so the main draw-back is a one-time installation expense. A reduction in the number of projections acquired in a stationary scanner, on the other hand, can both reduce the radiation exposure and the cost of the scan, as each fan of X-rays is an expense at installation, and also increases the cost of operation as wear on the X-ray tubes. Therefore, we focus on image reconstruction from projection data with *sparsity* with respect to the number of source positions. Figures 4.2(b) and (c) show schematic drawings of source positions for full data and the sparse data considered. The drawings of the fan-beam and full data are scaled, as modern CT scanners typically measure 800-1500 projections of 600-1200 data points each [65]. Regarding n_s X-ray source positions, each one measuring n_d ray attenuations, the $n_d \times n_s$ matrix of projections data is referred to as a *sinogram* (Figure 4.3(b)).

With this fan-beam projection model, a three-dimensional image can be formed as a stack of *slices*, acquired by moving the object stepwise along the z-direction relative to the source/detectors. Alternative geometries, such as multi-slice, helix, and cone beam CT, are described in [65].

Reconstruction with the analytical approach of FBP is known to suffer from serious shortcomings when the data is significantly incomplete [99]. With the goal of our application in mind, it is therefore necessary to formulate the problem in terms of a discrete observation model and seek an approximate solution augmenting the data by complementary information.

Forming the discrete setting, the domain Ω is discretised using an $m \times n$ regular grid of image pixels $P_{i,j}$ (Figure 4.4). The mass absorption coefficient μ is assumed constant in each pixel

$$\mu(p) = \mu_{i,j},\ p \in P_{i,j},\ 1 \leq i \leq m,\ 1 \leq j \leq n. \tag{4.4}$$

Consider the vector $x \in \mathbb{R}^N$, with $N = n \cdot m$, containing the matrix entries of

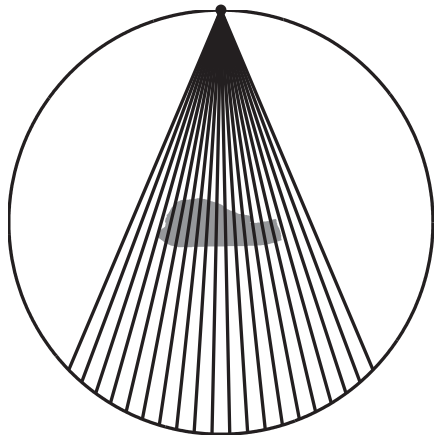

(a) Fan-beam.

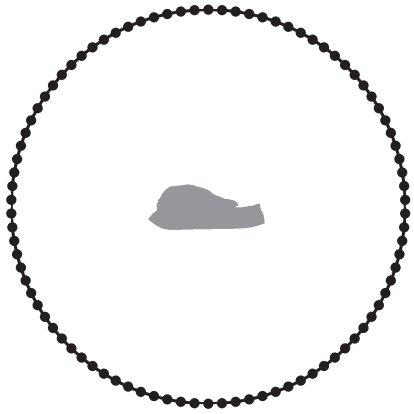

(b) Full data.

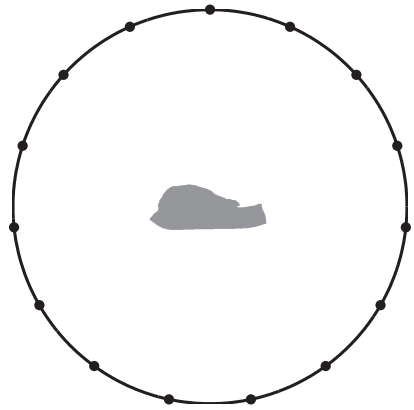

(c) Sparse data.

Figure 4.2: Geometric illustration of projection data. (a) A single fan-beam projection; The lines illustrate rays emitted from a point source, hitting an arc-shaped array of 20 equally spaced detectors after passing through the object. (b) and (c) Source position set-ups for acquisition of full data and sparse data, respectively. Illustrations from chapter 9.

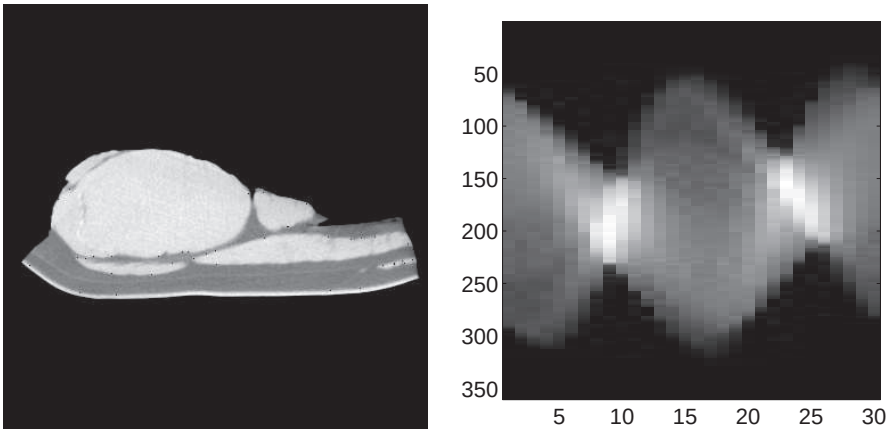

(a) Pig back. (b) Sinogram.

Figure 4.3: CT image data. (a) Pig back. (b) Corresponding simulated fan-beam sinogram of sparse projection data. (fan opening angle 45°, measuring $n_d = 360$ rays in each of the $n_s = 30$ source positions). Images from chapter 9.

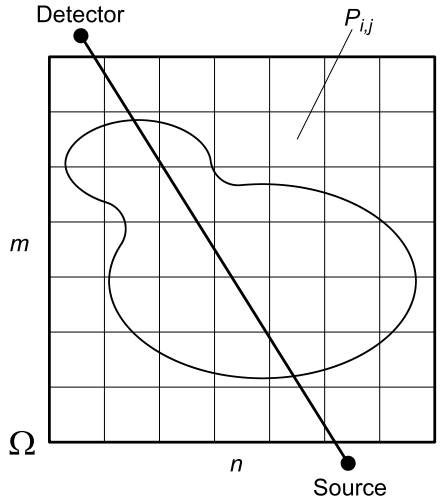

Figure 4.4: The spatial domain Ω is partitioned into $m \times n$ pixels, and the attenuation coefficient μ is discretised as a piecewise constant function in each pixel. Illustration from chapter 9.

μ_{ij} in column-wise ordering, and the measured projections in a vector $b \in \mathbb{R}^K$, with $K = n_s \cdot n_d$. The kth element b_k holds the measurements of the attenuated kth X-ray, corresponding to the integral along the line L_k through Ω, connecting this source/detector pair. With $|L_k \cap P_{i,j}|$ as the length of the intersection of L_k and the pixel $P_{i,j}$, the domain of integration can be discretised as a finite sum of contributions from individual pixels

$$b_k = \int_{L_k} \mu(p)dp = \sum_{i=1}^{n} \sum_{j=1}^{m} |L_k \cap P_{i,j}| \, \mu_{i,j} = \sum_{s=1}^{N} A_{k,s} x_s. \tag{4.5}$$

Organising the lengths of the intersections between the K source to detector lines and the N pixels into the matrix $A \in \mathbb{R}^{K \times N}$, the discrete problem takes the form

$$b = Ax. \tag{4.6}$$

From this *discrete Radon transform* of x, the CT image reconstruction problem can then be regarded as the inverse problem of estimating N unknowns given a system of K linear equations. The system matrix A is typically very large and extremely sparse, because each ray intersects a very small fraction of the pixels.

Iterative methods are the natural choice for solving large sparse systems of equations. In the context of image reconstruction, the algebraic reconstruction technique (ART), introduced by Gordon et al. in 1970 [44] and applied in the early work of Hounsfield [8, 54], has enjoyed vast popularity. The details of ART are well described in the literature, e.g. in [100].

When regarding few projection data, the large ratio of unknowns to measurements (the large null space of A), the ill-conditioning of the problem and the errors in the model and measurement, all pose problems for the computation of a stable and meaningful solution. One way to overcome this ill-posedness, is to introduce complementary information about the problem and the expected solution, a technique commonly referred to as regularisation in the inverse problems community. A popular approach is to adopt a statistical framework. A main property of statistical inversion is the possibility to augment the quantitative data with qualitative information about the sought solution.

4.2 Statistical Inversion

In the statistical approach to solving inverse problems all unknown parameters (x and b in (4.6)) are regarded as random variables (X and B), hence described in terms of probability density functions (π) rather than actual values.

The randomness is not intended as an intrinsic property of the unknowns, but rather a reflection of our uncertainty about their values. The image is the unknown quantity of interest, and the measured X-ray projections are affected by uncertainties due to both measurement errors and model limitations.

In this framework, it is therefore natural to express any *a priori* belief about them through what is known in Bayesian terms as a prior probability density function. This is a means of compensating for the paucity, or poor quality, of data, and the approach has been shown to be quite effective in a variety of applications. The theoretical foundations and several examples can be found in [17, 62].

In general, the Bayesian solution of an inverse problem amounts to infer on the unknown of primary interest, X, from measurement of another variable B, assuming a model linking the two and in the light of what are the believed properties of X. The *likelihood* is the probability density function of B assuming that $X = x$ is known, denoted as $\pi_{\text{likelihood}}(b \mid x)$. The shape of the likelihood is strongly affected by the characteristics of the noise, as will be explained below. The *prior* probability density function, $\pi_{\text{prior}}(x)$, expresses the perceived characteristics of X prior to taking the data into consideration. The *posterior*, $\pi_{\text{posterior}}(x)$, is the probability density function of X conditioned on the current realisation of the data, $\pi_{\text{posterior}}(x) = \pi(x \mid b)$, and can be interpreted as the correction of the prior in the light of the likelihood.

It follows from basic probability rules and Bayes' formula that

$$\pi(x \mid b)\pi(b) = \pi_{\text{likelihood}}(b \mid x)\ \pi_{\text{prior}}(x), \tag{4.7}$$

and

$$\pi(x \mid b) \propto \pi_{\text{likelihood}}(b \mid x)\ \pi_{\text{prior}}(x), \tag{4.8}$$

with the marginal density $\pi(b)$ of B neglected as a mere scaling of the posterior independent of x.

Determining the posterior density is the Bayesian solution to the inverse problem. From the posterior, one can compute the realisation of X which has the highest probability, the maximum *a posteriori* (MAP) estimate. Moreover, the added benefit of having the solution expressed as a density rather than a single realisation, is that sampling from the posterior provides a mean to assess the uncertainty that propagates onto the estimate [18, 19].

4.3 Bayesian Computed Tomography

The discrete tomographic reconstruction model can be reformulated in the Bayesian framework, such that the likelihood is formed corresponding to the CT fan-beam model, and the prior encodes the qualitative a priori belief about the structure of the scanned object.

The CT projection model (4.6) should also account for errors in the measured data as well as model limitations — the aggregate of which will be referred to as noise. Assuming that the noise is additive and independent of the image that we want to estimate, we have the noisy discrete model

$$b = Ax + e. \tag{4.9}$$

With $B, E \in \mathbb{R}^K$ and $X \in \mathbb{R}^N$ as random variables, we have the corresponding stochastic extension

$$B = AX + E. \tag{4.10}$$

In CT the measurements are photon counts, hence the distribution of the data can naturally be regarded as Poisson distributed. However, unless low dose measurements are used, the photon count is high, and it is therefore reasonable, and computationally advantageous, to resort to a Gaussian approximation, details are described in the appendix of [108]. Assuming that the noise in each data entry is independent, zero-mean Gaussian noise model with variance σ^2, $E \sim \mathcal{N}(0, \sigma^2 I)$, the likelihood of the observed data can be written as

$$\pi_{\text{likelihood}}(b \mid x) \propto \pi_{\text{noise}}(b - Ax) \propto \exp\left(-\frac{1}{2\sigma^2}\|b - Ax\|^2\right). \tag{4.11}$$

The design of informative priors which are also computationally efficient is an important and challenging topic which has received a lot of attention recently. Their construction tends to be based on notions which are believed to be true about image content, which may include intensity ranges or particular structural features. A review of prior formulations in the context of CT along these guidelines can be found in [108], where the connection between specific types of priors and Tikhonov regularisation is discussed. Of particular interest is the total variation (TV) penalty and its Markov random field characterisation: the solution is expected to have piecewise constant structures, as is the case in [107], where the iterative image reconstruction algorithm based on the minimisation of the image TV is presented.

In the Bayesian approach to the CT few projection problem presented by Hsiao et al. [56], a prior in the form of a mixture of gamma densities is applied to image

reconstruction with few data, while Chen et al. [22] propose a reconstruction method for low-dose CT which combines Bayesian statistics with MRF theory to design an adaptive-weighting nonlocal prior. In [58] it is shown that a prior based on the L_0 norm can be very effective for CT reconstruction from very sparse data.

In our target application, the scanned object is known to consist of well-separated regions with different X-ray attenuation coefficients. Thus, it is reasonable to expect that the reconstructed image has clearly distinct areas of homogeneous intensities, with sharp transitions in between. Therefore a good prior, accounting for the structure of the object, should favour little change in intensity within same tissue regions, and allow sharp changes of intensity at the boundaries between different tissues. In mathematical terms this can be translated into expecting small spatial derivatives inside a uniform region, and very high at the transition between one region and the other.

Following [18], let L_1 and L_2 be the finite difference matrices for the horizontal and vertical first order partial derivatives with zero boundary conditions. These expected small partial derivatives of X can be expressed as

$$L_* X \sim \mathcal{N}(0, D_\theta) \tag{4.12}$$

$$\pi(L_* x) \propto \exp\left(-\frac{1}{2} x^T \left(L_*^T D_\theta^{-1} L_*\right) x\right), \tag{4.13}$$

with L_* denoting either L_1 or L_2.

This smoothness condition is equivalent to modelling the partial derivatives as zero-mean multivariate Gaussian variables with covariance matrices $D_\theta = \operatorname{diag}(\theta_1, \ldots, \theta_N)$, where $\theta_j > 0,\ j = 1, \ldots, N$. The vector θ conveys the expected variability of the intensity derivatives at the different pixels. Since the values θ_j act as weights in (4.13), they affect the location of the edges in the reconstructed image. Setting the variance equal at all pixels $\theta_j = \theta_0$ is tantamount to expecting the image to be equally smooth everywhere, while a larger than average value θ_j, would convey the expectation that an edge may occur at pixel x_j. If the location and magnitude of edges were known in advance, they could be used to determine the individual values of the θ_js. In general, however, the information available prior to the reconstruction is only qualitative; sharp edges are expected between different tissue types in an otherwise smooth image — but with no information about position, magnitude or number.

Since θ is a vector of unknown parameters, it should also be considered as a realisation of a random variable, Θ. And thus, it must be added to the list of variables to estimate. The joint prior density of X and Θ is

$$\pi(x, \theta)_{\text{prior}} = \pi_{\text{prior}}(x \mid \theta)\pi_{\text{hyper}}(\theta). \tag{4.14}$$

Because the uncertainty carried into the problem by Θ affects the unknown at another layer, it is referred to as a hyperparameter vector and refer to the corresponding probability density function $\pi_{\text{hyper}}(\theta)$ as a *hyperprior*.

For a fixed $\Theta = \theta$, assuming independence between horizontal and vertical partial derivatives, the prior becomes

$$\pi_{\text{prior}}(x \mid \theta) = \pi(L_1 x,\ L_2 x \mid \theta) = \pi(L_1 x \mid \theta)\pi(L_2 x \mid \theta). \tag{4.15}$$

Relaxing the condition on the hyperparameter θ and adding it to the list of the unknowns, implies that the normalising factor of (4.13) which depends on θ must be explicitly accounted for, hence

$$\pi(L_* x \mid \theta) = \frac{|L_*|}{(2\pi)^{N/2}|D_\theta|^{1/2}} \exp\left(-\frac{1}{2} x^T \left(L_*^T D_\theta^{-1} L_*\right) x\right), \tag{4.16}$$

from which we arrive at the following conditionally Gaussian prior formulation

$$\begin{aligned} \pi_{\text{prior}}(x \mid \theta) &= \frac{|L_1||L_2|}{(2\pi)^N |D_\theta|} \exp\left(-\frac{1}{2} x^T C_\theta x\right) \\ &\propto \left(\prod_{j=1}^{N} \theta_j^{-1}\right) \exp\left(-\frac{1}{2} x^T C_\theta x\right), \end{aligned} \tag{4.17}$$

where $C_\theta = L_1^T D_\theta^{-1} L_1 + L_2^T D_\theta^{-1} L_2$.

The choice of $\pi_{\text{hyper}}(\theta)$ should reflect our expectation of distinct edges with sudden variation of the intensity across an edge, while no information about their presumed location. Hence, the θ_j's should be mutually independent and identically distributed. Moreover, since the image is expected to consist of large homogeneous regions, we may expect the values of the derivatives to be large only at few pixels. Therefore the hyperprior should be chosen to favour small values, but allow a few outliers. The Gamma distribution [7]

$$\Theta_j \sim \text{Gamma}(\alpha, \theta_0), \tag{4.18}$$

with the density

$$\pi_{\text{hyper}}(\theta) \propto \prod_{j=1}^{N} \theta_j^{\alpha-1} \exp\left(-\frac{\theta_j}{\theta_0}\right), \tag{4.19}$$

which is shown in Figure 4.5, qualitatively corresponds to these properties. The mode of the density near zero corresponds to the large proportion of smooth regions in the image, while the right tail allows intensity jumps if needed. The figure illustrates how the two parameters affect the shape of the hyperprior density function.

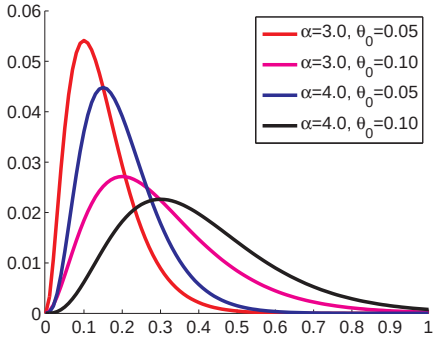

Figure 4.5: Examples of density functions for the gamma distribution.

With this hyperprior, the joint prior for X and Θ is

$$\pi_{\text{prior}}(x,\theta) \propto \left(\prod_{j=1}^{N} \theta_j^{-1}\right) \exp\left(-\frac{1}{2}x^T C_\theta x\right) \left(\prod_{j=1}^{N} \theta_j^{\alpha-1} \exp\left(-\frac{\theta_j}{\theta_0}\right)\right). \quad (4.20)$$

The introduction of this additional layer does not change the form of the likelihood, but the posterior needs to be adjusted accordingly

$$\pi_{\text{post}}(x,\theta \mid b) \propto \exp\left(-\frac{1}{2\sigma^2}\|b-Ax\|^2 - \frac{1}{2}x^T C_\theta x + (\alpha-2)\sum_{j=1}^{N}\log\theta_j - \sum_{j=1}^{N}\frac{\theta_j}{\theta_0}\right), \quad (4.21)$$

where $C_\theta = L_1^T D_\theta^{-1} L_1 + L_2^T D_\theta^{-1} L_2$.

4.4 Image Estimation and Uncertainty Quantification

As mentioned in section 4.2, one can compute the image as the MAP estimate; the maximiser of the posterior distribution provided by the Bayesian formulation. The MAP estimate of (x,θ) is the minimiser of the negative logarithm

$$\begin{aligned} F(x,\theta) &= -\log(\pi_{\text{post}}(x,\theta \mid b)) \\ &= \frac{1}{2\sigma^2}\|b-Ax\|^2 + \frac{1}{2}x^T C_\theta x - (\alpha-2)\sum_{j=1}^{N}\log\theta_j + \sum_{j=1}^{N}\frac{\theta_j}{\theta_0}. \end{aligned} \quad (4.22)$$

Gradient-based numerical algorithms for optimisation (e.g. [39]) can be applied for the joint-estimation of (x, θ). However, an efficient alternating algorithm for finding the minimiser of objective functions with a similar structure has been proposed in [7, 18].

The algorithm sequentially updates one of the two unknowns x and θ, while keeping the other fixed:

1. Initialise $k = 1$ and $\theta^0 = \text{diag}(\theta_0)$.
2. Update $x^k = \text{argmax}\{\pi_{\text{post}}(x, \theta^{k-1} \mid b)\}$.
3. Update $\theta^k = \text{argmax}\{\pi_{\text{post}}(x^k, \theta \mid b)\}$.
4. Update $k = k + 1$ and return to step 2.
   Repeat until convergence.

When $\theta = \theta^k$ is fixed in step 2, $F(x, \theta)$ is a quadratic function of x, with a minimiser in the form of the least squares solution of the linear system

$$Mx = r, \quad M = \begin{bmatrix} \sigma^{-1}A \\ D_\theta^{-1/2}L_1 \\ D_\theta^{-1/2}L_2 \end{bmatrix}, \quad r = \begin{bmatrix} \sigma^{-1}b \\ 0 \\ 0 \end{bmatrix}, \tag{4.23}$$

which can be computed by the Conjugate Gradient method for Least Squares (CGLS) iterative method [11, 52]. When $k = 1$, this update corresponds to applying the first order smoothness penalty with equal weight on all pixels.

In step 3, with $x = x^k$ fixed, the first term in (4.22) is independent of θ. Since mutual independent θ_j's are assumed for the hyperprior, the update of θ can be done element wise by solving $\frac{\partial F}{\partial \theta_j} = 0$ for $j = 1, \ldots, N$

$$-\frac{1}{2}\frac{[L_1 x]_j^2 + [L_2 x]_j^2}{\theta_j^2} + \frac{1}{\theta_0} + (\alpha - 2)\frac{1}{\theta_j} = 0, \tag{4.24}$$

where $[L_1 x]_j^2$ and $[L_2 x]_j^2$ denote the square of the derivative at pixel j in the respective direction. An analytical solution exists to this second order polynomial equation. Thus, the update of the entries of θ in step 3 follows the closed-form expression

$$\theta_j = \theta_0 \left(\eta + \sqrt{\frac{[L_1 x]_j^2 + [L_2 x]_j^2}{2\theta_0} + \eta^2} \right), \tag{4.25}$$

with $\eta = \frac{1}{2}(\alpha - 2)$.

Figure 4.6 illustrates the iterative procedure by means of intermediate estimates of the image and hyperparameter for $k = 1, \ldots, 4$.

The MAP estimator gives no indication of the uncertainties of the estimate. To quantify this, one typically needs to resort to Markov chain Monte Carlo (MCMC) sampling methods [71, 74]. In imaging applications this is challenging because of the high dimensionality of the problem. This is aggravated with our hierarchical formulation, as sampling must comprise both X and Θ.

However, one is often only interested in evaluating the uncertainty within a given spatial region of interest (ROI) defined on the image, e.g. containing certain features of interest [18]. Figure 4.7, shows an example of a ROI consisting of pixels around the interface between meat and fat. For the industrial application, the location of this transition is of particular importance to guide a cutting robot trimming the rind to a given thickness.

Following this, both image and hyperparameter are partitioned into two sets $X = [X'; X'']$ and $\Theta = [\Theta'; \Theta'']$, such that they contain pixels within the ROI and in the complement, respectively. The posterior density of the variables in the ROI conditioned on the complement as well as the observations b, can then be written as

$$\pi(x', \theta' \mid b, x''_{\mathrm{MAP}}, \theta''_{\mathrm{MAP}}) \propto \pi(x, \theta \mid b)\big|_{x''=x''_{\mathrm{MAP}}, \theta''=\theta''_{\mathrm{MAP}}}, \tag{4.26}$$

with the MAP-subscript referring to the respective elements of the MAP estimates.

The MCMC sampling over the ROI can be done with a block form of the Gibbs sampler [41, 74]. As with the iterative MAP estimation, we adopt the two-step approach for the sampler, fixing alternately one of the parameters x' and θ', while updating the other by drawing from the conditional density. More precisely, the algorithm is described as follows:

1. Initialise $k = 0$, $x^0 = x_{\mathrm{MAP}}$ and $\theta^0 = \theta_{\mathrm{MAP}}$.
2. Draw x' from the conditional distribution $\pi(x' \mid b, \theta^k, x''_{\mathrm{MAP}})$.
   Update $x^{k+1} = [x'; x''_{\mathrm{MAP}}]$.
3. Draw θ' from the conditional distribution $\pi(\theta' \mid b, x^k, \theta''_{\mathrm{MAP}})$.
   Update $\theta^{k+1} = [\theta'; \theta''_{\mathrm{MAP}}]$.
4. Update $k = k + 1$.
   Repeat from step 2 until the desired sample size is reached.

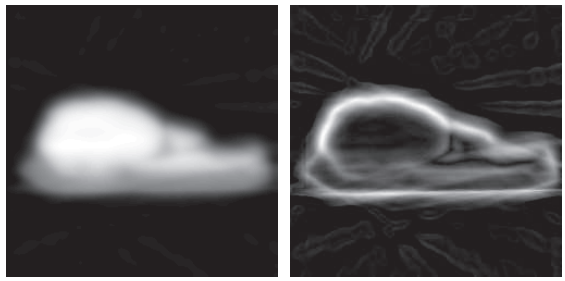

(a) $k = 1$.

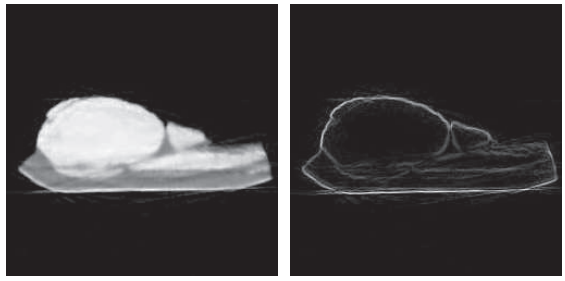

(b) $k = 2$.

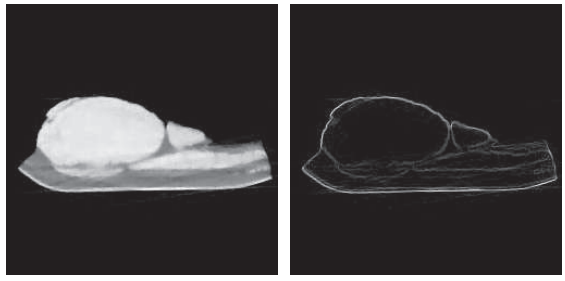

(c) $k = 3$.

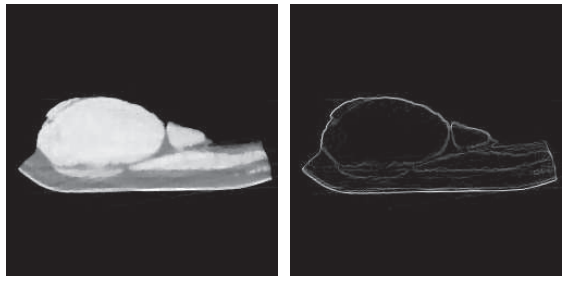

(d) $k = 4$.

Figure 4.6: Intermediate estimates for image x and hyperprior θ of the first four consecutive iterations of the two-step algorithm. The reconstruction is based on the simulated sinogram in Figure 4.3. Images from chapter 9.

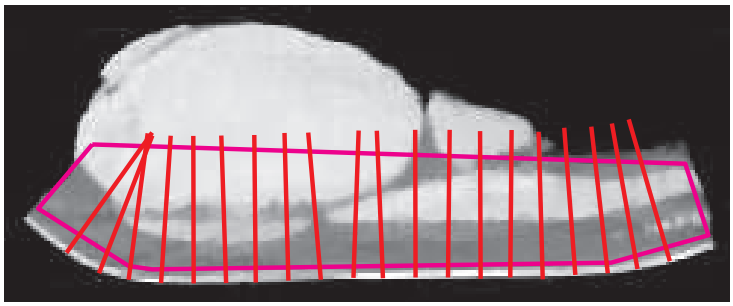

Figure 4.7: MAP-estimate image with lines and polygon illustrating the 20 measurement profiles and the ROI, respectively. Image from chapter 9.

In step 2, let M and r be the arrays defined in (4.23), with $\theta = \theta^k$, and let $M = [M', M'']$ be the column partitioning of M corresponding to the ROI and its complement. The factor in the posterior distribution conditioned on $\theta = \theta^k$ depending on x is

$$\pi(x' \mid b, \theta^k, x''_{\text{MAP}}) \propto \exp\left(-\frac{1}{2}\|M'x' + M''x''_{\text{MAP}} - b\|^2\right), \tag{4.27}$$

suggesting that a random draw for x' can be accomplished by solving in the least squares sense the problem

$$M'x' = b - M''x''_{\text{MAP}} + \xi, \quad \xi \sim \mathcal{N}_k(0, I). \tag{4.28}$$

The problem can be solved using the CGLS algorithm.

In step 3, we exploit the mutual independency of the components θ_i in the posterior distribution. The posterior distribution of θ_j is

$$\pi(\theta_j) \propto \exp\left(-\frac{1}{2}\frac{[L_1x]_j^2 + [L_2x]_j^2}{\theta_j^2} + (\alpha - 2)\log\theta_j - \frac{\theta_j}{\theta_0}\right), \; j \in I_{\text{ROI}}, \tag{4.29}$$

and the component-wise draws are with the inverse probability density algorithm (see [17]).

The uncertainty over the ROI needs to be interpreted and visualised from the variability of the sample generated. Finding a suggestive way of visualising the variability may be a challenging task. One possibility to overcome the difficulty of grasping the high dimensionality of the image and hyperprior is to perform the same measurements on all samples and compare them. Figure 4.7 illustrates this reduction of dimensionality for easier interpretation; studying the variability of the fat layer thickness measured in 20 profiles perpendicular to the skin surface.

4.5 Image Upsampling

Three-dimensional images acquired in a slice-wise manner often suffer from anisptropy, e.g. 1 cm slice thickness and slice spacing paired with sub-millimetre in-plane resolution. A low out-plane resolution can cause problems for the interpretation, by blowing up the partial volume effect; image artefacts occurring as part of the digitalisation, when forming images by slices of volumetric blocks rather than infinitely thin two-dimensional planes.

Images containing thin structures running parallel with the slice planes are particularly vulnerable. In relation to CT in the abattoir, Hansen et al. [49] reported issues analysing images of pork middles, where the ribs appeared geometrically distorted and some thinner muscles would vanish or fade out. Images with structures covering several slices can also suffer from anisotropy, as shown by Erbou and Ersbøll [30] in their work on analysing three-dimensional bone structures. However increasing the out-plane resolution by acquiring more slices, spaced closer together, would increase both scan time and cost — and thus, is undesirable for the online application.

Image interpolation plays an important role by closing the gap between the true continuous nature of an image and the practical discrete representation. Uniform tensor splines such as tricubic interpolation, is the method of choice for most applications due to the regular sampling of image voxels. A potential problem with this approach is the inherent assumption of a smooth transition between neighbouring voxels across slices.

As a solution, *registration-based interpolation* was introduced by Penney et al. [94]. Correspondences between neighbouring slices are determined by one-way registrations in 2D. The interpolation is then performed along these lines of correspondence to achieve a smooth transition, rather than using the usual lateral neighbourhood. Frakes et al. [38] extended the method by using both a forward and backward registration; a weighted sum of two non-symmetric displacement fields. Recently, Ólafsdóttir et al. [89] proposed a method to improve the method even further, suggesting an interpolation based on weighting both intensity and deformation by the inter-slice distance of the interpolation point.

Registration-based interpolation is highly dependent on the quality of the correspondences obtained. This can be somewhat questionable, as there may not exist a one-to-one mapping between adjacent slices. That is, structures may disappear between two slices, and in these situations one must rely on the registration scheme.

As an alternative to the interpolation described above, we propose fitting a parametric function to the slices, accounting for the partial volume effect by incorporating the slice thickness. Furthermore, we use regularisation based on the symmetric registration to stabilise the ill-posed problem. As the idea behind the method is to identify the underlying image rather than interpolating the thick slice voxels, we say the method *upsamples* the anisotropic image under reasonable constraints.

The goal of our method is to obtain a better approximation of the true three-dimensional image R given a representation by K slices $\{S^1, S^2, \ldots, S^K\}$ of $M \times N$ voxels each. That is, the expected value of the (i,j)th voxel of the kth slice image S^k_{ij} is given by the intrgral

$$E[S^k_{ij} \mid R] = \int_{V_{ij}} R(\boldsymbol{x}) dv, \tag{4.30}$$

where V_{ij} is the volume element covered by the (i,j)th voxel. The partial volume effect occurs, when this volume contains a mixture of multiple tissue values.

The strategy is find the best parametric image function, $\tilde{R}$, to match the observed slices. We use cubic B-splines $\boldsymbol{b}$, parameterised by weights $\boldsymbol{p}$, to represent the image intensities. In three dimensions, we write

$$\tilde{R}(\boldsymbol{x}, \boldsymbol{p}) = \langle \boldsymbol{b}(x_3) \otimes \boldsymbol{b}(x_2) \otimes \boldsymbol{b}(x_1), \boldsymbol{p} \rangle, \tag{4.31}$$

where $\langle \cdots, \cdots \rangle$ denotes the inner product, and $\otimes$ is the tensor product of the one-dimensional basis functions.

The comparison is formulated as

$$\mathcal{M}[\tilde{R}, \{S^k\}_{k=1\ldots K}] = \sum_{k=1}^{K} \sum_{i=1}^{M} \sum_{j=1}^{N} m(E[S^k_{ij} \mid \hat{R}], S^k_{ij}), \tag{4.32}$$

where $m(\cdot)$ is a measure of similarity between voxels in the observed and estimated slices, e.g. the squared difference in intensities — a choice based on the assumption of the underlying noise model of the data.

From this, the continuous representation of R, can be estimated by minimising (4.32) with respect to the image parameters. However, relying on image intensities alone forms an ill-posed problem. This can be addressed by adding regularisation to the minimisation

$$\min_{\tilde{R}} \mathcal{M}[\tilde{R}, \{S^k\}_{k=1\ldots K}] + \beta \mathcal{S}_{\boldsymbol{v}}[\tilde{R}]. \tag{4.33}$$

We propose a regularisation term that penalises high image gradients in certain directions. This can be formulated as an inner product between the image gradient and a vector field $\boldsymbol{v}$

$$\mathcal{S}_{\boldsymbol{v}}[\tilde{R}] = \int_{\Omega} \langle \nabla \tilde{R}(\boldsymbol{x}), \boldsymbol{v}(\boldsymbol{x}) \rangle^2 d\boldsymbol{x}. \tag{4.34}$$

That is, $\boldsymbol{v}$ determines the direction and magnitude of the penalty, functioning as a *penalisation vector field*.

Inspired by [38, 89, 94] the penalisation vector field is formed by non-rigid registration of neighbouring slices S^1 and S^2, e.g. with the popular free-form deformation model by Rueckert et al. [102]. A symmetric registration is applied, assuming correspondence between points $\boldsymbol{\phi}_1(\boldsymbol{x}) = \boldsymbol{x} - \boldsymbol{u}(\boldsymbol{x})$ in slice S^1 and $\boldsymbol{\phi}_2(\boldsymbol{x}) = \boldsymbol{x} + \boldsymbol{u}(\boldsymbol{x})$ in slice S^2 (Figure 4.8).

Each element of the penalisation vector field is then composed by a half slice thickness τ, the estimated displacement $\boldsymbol{u}$ and a weight γ

$$\boldsymbol{v}(\boldsymbol{x}) = \gamma(\boldsymbol{x}) \frac{[\tau,\ \boldsymbol{u}(\boldsymbol{x})]^{\mathrm{T}}}{\| [\tau,\ \boldsymbol{u}(\boldsymbol{x})]^{\mathrm{T}} \|}. \tag{4.35}$$

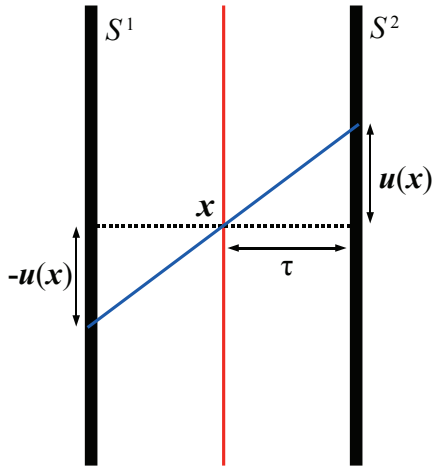

Figure 4.8: Illustration of the slice registration setup and the penalisation vector field. From chapter 10.

Regions of homogeneous intensities contain no information to guide the registration. Instead, edges *within* slices are of interest: Both slices must contain edge information around the matching point in order for the correspondence to

be regarded as strong. This can be accounted for by the scale factor γ in (4.35).

$$\gamma(\boldsymbol{x}) = \frac{\left|G'_\sigma * \left(S^1 \circ \boldsymbol{\phi}_1(\boldsymbol{x})\right) + G'_\sigma * \left(S^2 \circ \boldsymbol{\phi}_2(\boldsymbol{x})\right)\right|}{\epsilon + \left(S^2(\boldsymbol{\phi}_2(\boldsymbol{x})) - S^1(\boldsymbol{\phi}_1(\boldsymbol{x}))\right)^2}, \tag{4.36}$$

with G'_σ denoting a first order derivative of a Gaussian kernel with standard deviation σ [20]. The denominator is the sum of the similarity of the slice registration and the constant ϵ, related to the intensity level of the image. As mentioned, the penalisation vector field is constructed by multiplying the correspondence directions from the registration by these scale factors.

Chapter 5

Overview of Contributions

This chapter summarises the main results obtained in the papers included in part II.

5.1 Quantification and Validation of Soft Tissue Deformation

Chapter 7 investigates the use of CT and techniques from image analysis as methods for modelling and analysing tissue deformation. The studies are part of the development of an automatic tool for trimming the rind off pig backs to a given fat layer thickness. Initial stages of the design phase have revealed the need for knowledge of the tissue deformation, caused by the machine handling the meat.

We present an image-based method for empirically modelling tissue deformation. Steel markers are placed inside the tissue to enable automatic generation of very reliable landmarks in three dimensions through CT. Pressure is applied onto the skin surface to mimic part of the cutting tool. By monitoring the displacement of the landmarks between two consecutive CT images (without and with pressure applied), we gain understanding of the tissue deformation induced by the

external forces. Under the assumption, that the marker displacements hold the ground truth for the tissue deformation at the given location, we are able to build and validate our data-driven model. Figure 5.1 shows the experimental set-up.

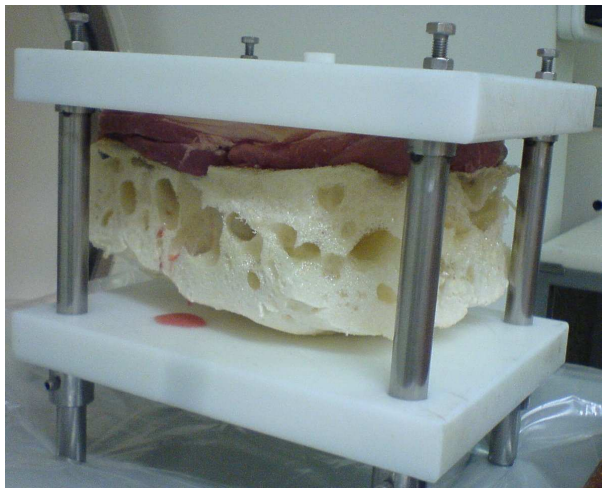

Figure 5.1: The experimental setup; the pig back is placed between two nylon plates and a foam cushion. The top of the indentation bolt (white) is just visible above the plate. In comparison to the scans, the setup is turned upside down for easier adjustment of the bolt between two CT scans.

Considering 10 pig backs, between 113 and 140 markers are inserted in each. We form a compact representation of the displacement fields with a parameterisation by the smooth and compactly supported Wendland functions [119], defined on a set of knot points common to all subjects. This technique is related to non-rigid image registration [37]. Representing the displacements of all 1282 markers injected in the 10 pig backs, the parameterisation yields an absolute error with mean 0.20 mm, median 0.13 mm, and standard deviation 0.21 mm. The accuracy of the compact parametric representation is illustrated in figure 5.2.

With this representation, the observed displacement fields are comparable by their parameters. We build a statistical model of the observations by feeding the parameters to a PCA model, an approach similar to statistical shape models [23]. To validate the model, we use subject-wise leave-one-out cross validation, estimating the prediction error; evaluating 10 models built from the remaining 9 deformation fields. Figure 5.3 shows histograms and corresponding descriptive statistics for absolute errors of the marker displacements achieved with different

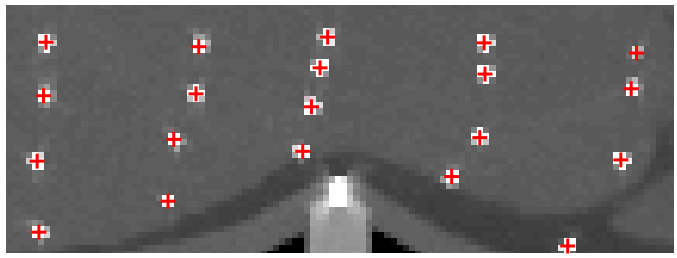

Figure 5.2: The red crosses show marker positions achieved by the accurate parametric representation.

subsets of modes in the PCA.

The results demonstrate the applicability of our image-based experiments for quantifying and studying tissue deformation. The mathematical representation and statistical model pave the way for further empirical analysis.

5.2 An Efficient Data-driven Tissue Deformation Model

Chapter 8 extends the experiments and analysis described in the previous section; modelling tissue deformation in relation to the development of a tool for automatic trimming the fat off pig backs. Pressure from the knives in the machine has been reported to cause lateral movement in the loin muscle, thus, complicating accurate cuts as defined by subject-specific on-line measurements.

In this work we assess the generality of the statistical deformation model and study the deformation contained in individual principal modes. In the latter, we focus on the loin muscle movement. This is then related to relevant measurements of carcass composition, suitable for utilisation in the abattoirs.

To investigate the generality of the model, we perform leave-one-out cross-validation by subject. For the given subject, excluded from the training set, the mean deformation parameters are applied to the marker positions and compared to the true observed displacements. Regarding all models built, this yields a mean absolute prediction error of 1.41 ± 0.87 mm, comparable to the voxel size in the CT images (0.9375 mm $\times$ 0.9375 mm, with a slice thickness of 1 mm).

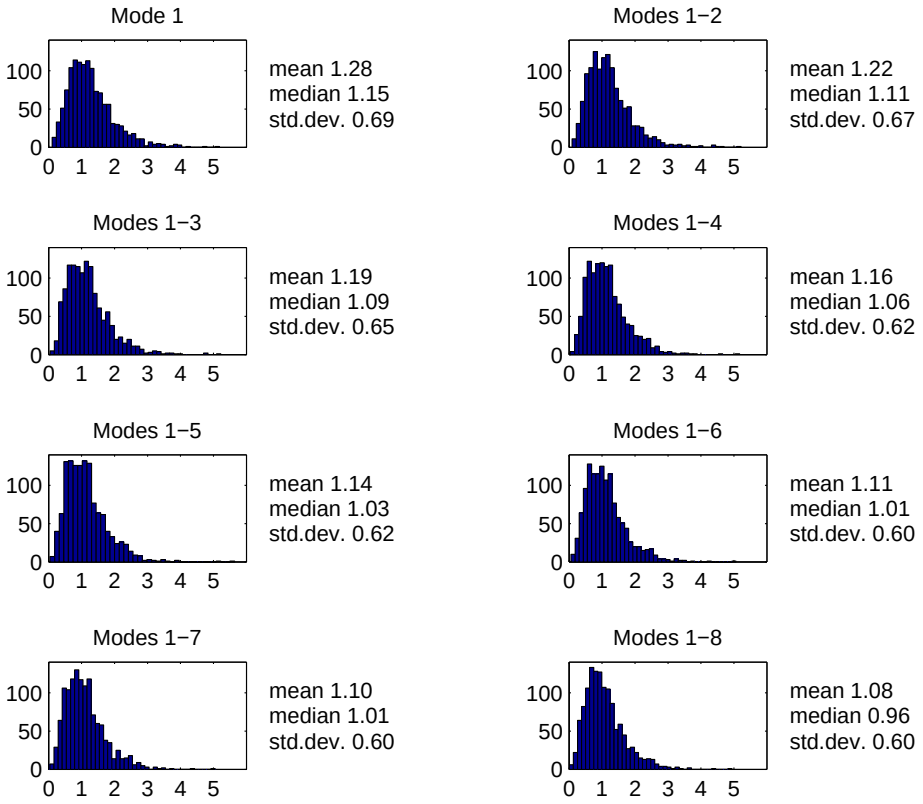

Figure 5.3: Histograms and corresponding descriptive statistics of the absolute errors (in mm) for all markers in all subjects; achieved by leave-one-out cross validation using different subsets of principal modes in the statistical deformation model.

The lateral movement of the loin muscle is examined in relation to the individual principal modes of the model. We find an association between the first principal mode and the movement. This mode explains 37 % of the total variance in the observed deformation fields.

Existing carcass grading systems are capable of performing estimates related to the rind thickness and loin muscle thickness [21], so it is sensible to use these two measurements to characterise the carcass composition of the subjects. Our model indicates a relation to this deformation: The most lean pig back exhibits a higher degree of lateral muscle movement compared to the more fatty subjects (Figure 5.4).

The presented analysis can provide valuable knowledge in the cutting tool development. Our results suggest sorting of the pig backs to discriminate the processing; e.g. compensating for the movement by applying different amounts of pressure to the opposite side of the muscle.

5.3 BASE-CT: Bayesian Adaptive Structure Enriched Computed Tomography

Chapter 9 presents an algorithm for tomographic image reconstruction from sparse X-ray projection data: BASE-CT. The algorithm follows the Bayesian approach to statistical inversion [62], formulating the inverse problem using probability density functions.

The context of the work is automated slaughtering, where CT images are intended to provide detailed information about carcasses for individual adaption of the processing. In order for this to be feasible in the high throughput environment of the abattoirs, the imaging equipment must be fast, robust and cost-efficient. In comparison to conventional CT, an image reconstruction based on sparse projection data, can lead to an increase in both speed and robustness as well as a reduction in cost.

BASE-CT is evaluated on a Shepp-Logan phantom [106] in comparison with three existing reconstruction methods; FBP [76], ART [100] and TV [107]. A 512×512 image is reconstructed from a simulated sinogram of 40 fan-beam projections of 180 attenuated rays each. Figure 5.5 displays the resulting reconstructions. The image obtained with BASE-CT is significantly better than those reconstructed with FBP and ART. In comparison to TV, we see a slight improvement in the ability to capture the most detailed image structures in the bottom part of the phantom.

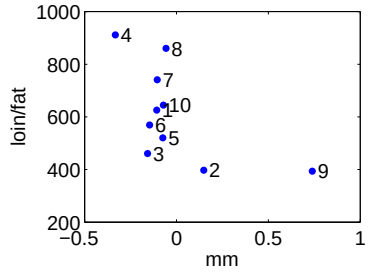

(a)

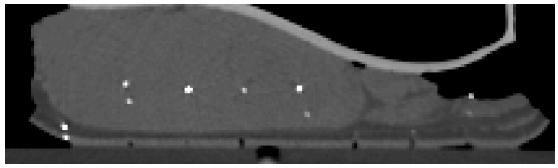

(b) Subject 4.

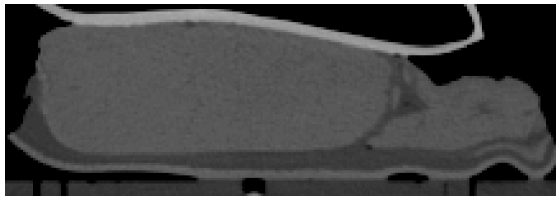

(c) Subject 1.

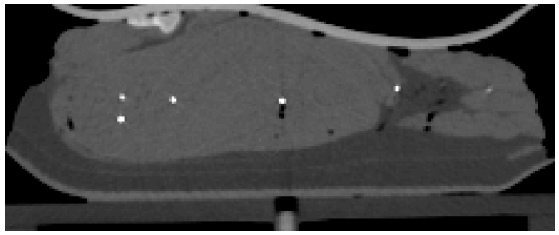

(d) Subject 9.

Figure 5.4: Analysing the tissue deformation contained in the first principal mode of the model. (a) Plot relating lateral movement of the loin muscle and fat tissue beneath it (x-axis) to the ratio between muscle size and fat layer thickness (y-axis). The numbers refer to subjects. (b)-(d) Three different carcass compositions resulting in different lateral loin muscle movements, quantified by our model.

(a) Original.

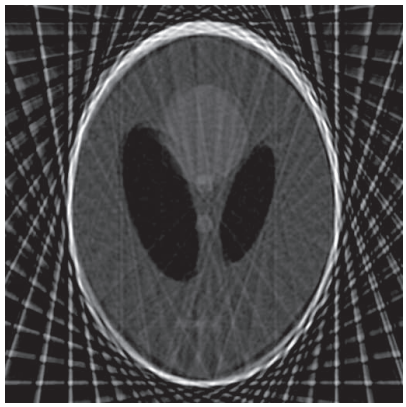

(b) FBP.

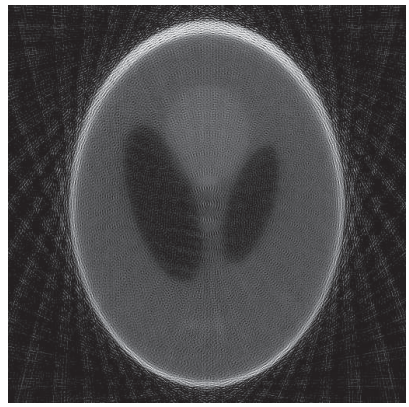

(c) ART.

(d) TV.

(e) BASE-CT.

Figure 5.5: Shepp-Logan phantom reconstructions.

The potential of BASE-CT is demonstrated in relation to two imaging applications from the abattoirs.

The first task is connected to automated trimming of the rind. To resemble the existing manual procedure [109], the thickness is measured in 20 profiles perpendicular to the skin surface. To quantify the uncertainty of the reconstructed MAP estimate, the measurements are repeated on 10000 random samples drawn from the posterior distribution of the image. Figure 5.6 shows histograms of the edge-position superimposed on the MAP estimate. The position of the transition between meat and fat is stable over the sample, and the corresponding histograms are very narrow, suggesting that the MAP-estimate image is a very good representative of the entire distribution.

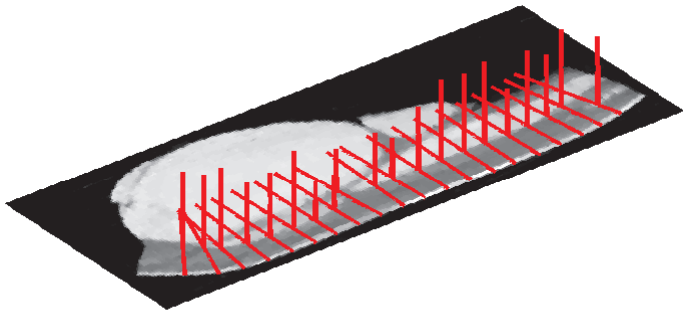

Figure 5.6: Histograms of edge positions located on the 10000 samples.

In the second application example, we use the CT image to measure the LMP of the carcass, an indicator used for grading and sorting for further processing. To study the suitability of our reconstructions, we perform tissue classification by intensity thresholding on both the original and the BASE-CT image. We achieve a good correspondence between the two sets of labels, with LMPs of 56.32% and 56.15%, respectively. To evaluate the reliability of our measurements we generate a sample of 3000 images of the entire pig back from the posterior; the sample mean LMP is 56.00% and the sample standard deviation 0.17%. Figure 5.7 shows the calculated LMPs corresponding to the 3000 draws. The values across the sample are very tightly clustered around the sample mean, as above suggesting that the image reconstruction is very reliable.

The measurements from the reconstructions exhibit a high degree of both accuracy and certainty. In this context, our results appear very promising for efficiently applying BASE-CT in industrial imaging in the abattoirs.

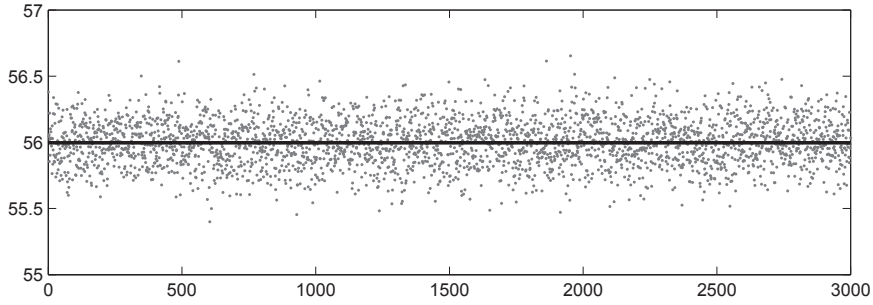

Figure 5.7: LMPs for a sequence of 3000 random draws from the posterior distribution. The horizontal line corresponds to the sample mean 56.00%.

5.4 Can Anisotropic Images Be Upsampled?

Chapter 10 presents a method for upsampling images suffering from anisotropy due to slice thickness. The resolution is increased, by fitting an image function, modelled by B-splines to the slices, while accounting for the slice thickness to handle partial volume artefacts. As the formulation is ill-posed, regularisation is added. Correspondences between adjacent slices are established using a symmetric registration method with a free-form deformation model [103]. High image gradients along lines of correspondence are penalised by means of a vector field, resulting in less regularisation where the two are approximately orthogonal and/or of low magnitude.

The performance of the upsampling (UP) is illustrated in two-dimensions in comparison with standard cubic interpolation (CI) [66] and one-way registration-based interpolation (RBI) [94].

From a 250×250 isotropic-sampled Shepp-Logan phantom [106], a downsampled anisotropic 250×50 image is created by averaging every five columns together. That is, the columns act as the thick slices in the two-dimensional example. Figure 5.8(c) displays the registration-based line correspondences superimposed on the anisotropic phantom. Based on the registration, a penalisation vector field was extracted (Figure 5.8(d)).

Figure 5.9 shows the enhanced phantom images corresponding to the two interpolation schemes and the upsampling. The mean squared error between pixel values in the isotropic-generated phantom and the enhanced images were 0.0143 for CI, 0.0073 for RBI, and 0.0045 for UP.

We see that UP provides the most visually pleasing result; the performance is

(a) Original phantom

(b) Anisotropic phantom

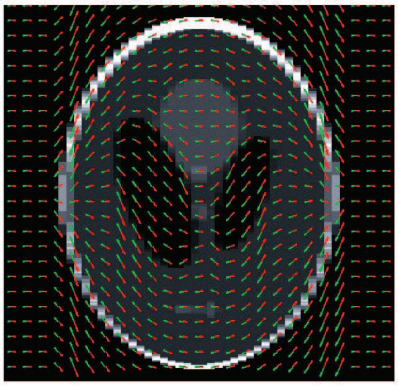

(c) Anisotropic phantom with correspondences from the registration

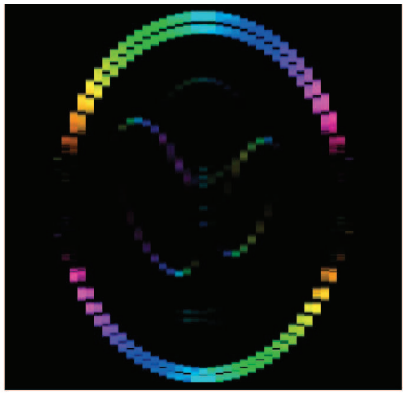

(d) Penalisation vector field

(e) Colour-map for penalisation vector field. The colour shows the direction and the brightness shows the magnitude.

Figure 5.8: Visualisation of phantom data, symmetric registration and the penalisation vector field.

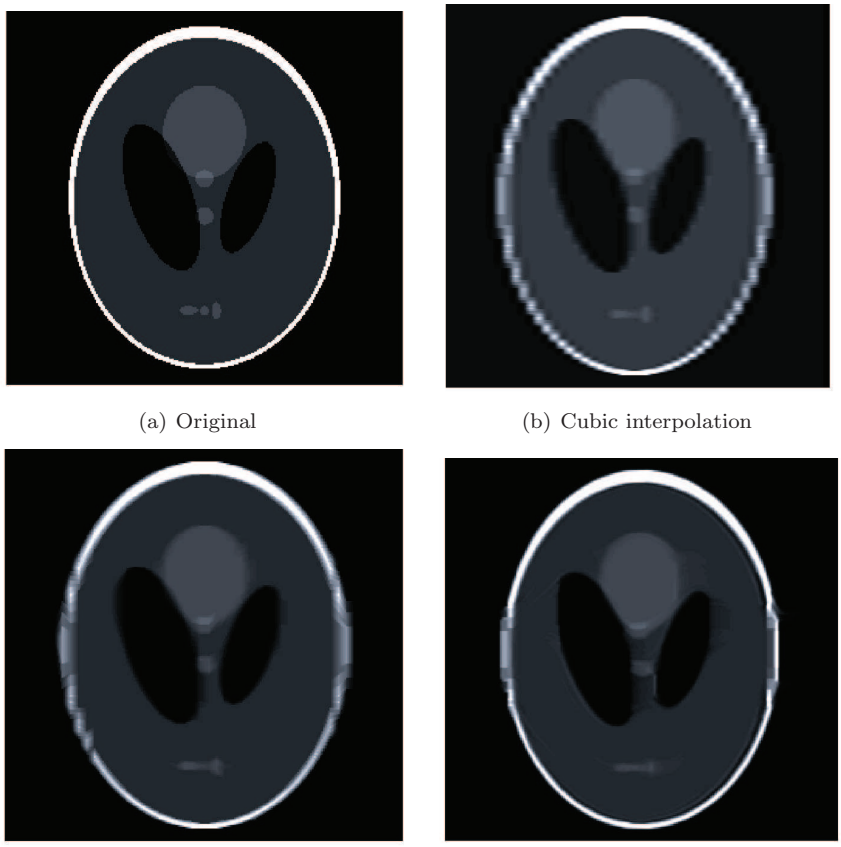

(a) Original (b) Cubic interpolation

(c) One-way registration (d) Upsampling

Figure 5.9: Original and enhanced phantom images.

confirmed by the error measures. Figure 5.9(c) shows how RBI provides good results in areas with good registration, and unsatisfactory interpolation in areas lacking correspondences — areas where structures run approximately parallel to the slices. Here, UP performs remarkably better. However, UP still produces some blurring in areas where the width of the structure in the original image is similar to the slice thickness in the anisotropic image— where the partial volume effect is too severe. These preliminary tests showed promising results, motivating further investigation and validation.

Chapter 6

Conclusion

This chapter discusses the contributions of part II, summarised in part I, in relation to the objectives of the thesis (cf. section 1.1) and aspects of future work. The chapter is concluded by a section with closing remarks on the work.

6.1 Discussion

The first objective of the thesis is to investigate the use of CT in analysis of tissue deformation in pig carcasses. The purpose is to assist developers of an automated robotic tool for trimming the rind off pig backs. The Virtual Slaughterhouse Project successfully demonstrated the use of CT for modelling biological variation across populations of pigs, providing knowledge of the raw materials for optimal processing and automation. The results presented in chapters 7 and 8 follow in these footsteps.

We propose an experimental setup for image-based tissue modelling. The inserted steel markers quantify the deformation very accurately, and the stamp provides good repeatability of the external force applied. In future work, the setup can be expanded to provide an even more comprehensive and realistic data set. One can add more pressure stamps to match the number in the machine, and combine this with acquisition of several additional CT images with

different indentation arrangements of the stamps.

The statistical deformation model is purely data-driven. In this way, the biological variation spanned by the model corresponds to the variation present in the 10 observations. An improvement is therefore to expand the data set, by including more pig backs with a larger variety in carcass composition.

The results turn out to provide valuable information for designing and calibrating the automated cutting machine, thereby presenting a suitable alternative or supplement to improve the existing tool development strategies.

The second objective of the thesis is the development of methods for efficient image reconstruction. This covers another aspect of CT in the abattoir; moving from studies of populations to accurate measurements of each single carcass for individual adaption of the processing.

In chapter 9 we propose a method for CT reconstruction: BASE-CT. The algorithm is intended for online use in the abattoir, thus demanding fast, robust and cost-effective imaging. BASE-CT provides extremely promising results, enabling a substantial reduction of the amount of X-ray data needed to reconstruct images of high quality. Such a reduction of data will inevitably lead to a faster image acquisition with a lower cost of operation.

Chapter 10 addresses slice-based three-dimensional images suffering from anisotropy. This image enhancement appears to be a highly suitable alternative to the expensive acquisition of more slices with less spacing.

The development of efficient image reconstruction techniques is an important step for DMRI and the Danish pig meat industry in the process of moving CT from the mobile unit into the abattoir as equipment for online measurements.

The existing US-based classification equipment, reports a maximum capacity of 1200 carcasses per hour [21]. Our algorithms are implemented on a standard laptop running MATLAB [76]. In order for the methods to be usable in practice, some effort should to be put into optimising the code, e.g. by parallelisation. This next step was already taken in February 2010; DMRI entered a collaboration involving the eScience Centre of the Department of Computer Science at the University of Copenhagen. This project will run until August 2013, aiming at *high performance high productivity*. Applications include real-time reconstruction and analysis of CT images for industrial applications, where the concepts of BASE-CT will play a considerable role.

6.2 Conclusion

This thesis consists of work combining techniques from medical imaging with applications in the meat industry. The methods and results are presented through publications for both medical and non-medical audiences. As the applications are industrial, the concerned subjects are *normal* — as opposed to the typical medical imaging scenario where the *abnormal* subjects are of prime interest.

The results of the work demonstrate the great potential of CT as a means for improving the yield of modern Danish abattoirs. We show how CT can be used to study the biological variation in populations. This is very important for efficiently processing inhomogeneous raw materials into homogeneous products of high quality. We take a peek into the future of applications in the abattoir, and propose a method for cost-effective CT reconstruction for online measurements of each individual carcass. This technology can be a highly useful tool for optimising the utilisation of the raw materials.

In the fierce international competition, the use of online CT can turn out to be game-changing. The development of innovative technology can help the Danish pig meat industry to maintain competitive prices and high product standards. In that way Denmark can remain a worldwide industry-leader.

Part II

Contributions

Chapter 7

Quantification and Validation of Soft Tissue Deformation

Thomas Hammershaimb Mosbech, Bjarne Kjær Ersbøll and Lars Bager Christensen

Abstract

We present a model for soft tissue deformation derived empirically from 10 pig carcases. The carcasses are subjected to deformation from a known single source of pressure located at the skin surface, and the deformation is quantified by means of steel markers injected into the tissue. The steel markers are easy to distinguish from the surrounding soft tissue in 3D computed tomography images. By tracking corresponding markers using methods from point-based registration, we are able to accurately quantify the magnitude and propagation of the induced deformation. The deformation is parameterised by radial basis functions with compact support. The parameterisation yields an absolute error with mean 0.20 mm, median 0.13 mm and standard deviation 0.21 mm (not cross validated). We use the parameterisation to form a statistical deformation model applying principal component analysis on the estimated deformation parameters. The model is successfully validated using leave-one-out cross validation by subject, achieving a sufficient level of precision using only the first two principal modes; mean 1.22 mm, median 1.11 mm and standard deviation 0.67 mm.

7.1 Introduction

The origin of this work lies in the meat industry, where there is an increasing demand for rapid automated processing of inhomogeneous pig carcasses into ho-

mogeneous products. A current area of research for the Danish Meat Research Institute is automation through computed tomography (CT) performed on-line in the abattoir. Figure 7.1 shows a conceptual drawing of a machine for processing pig backs to produce bacon with a given fat-layer thickness. The machine consists of cylinders pulling the meat towards a fixed horizontal knife, which trims the fat layer. The amount of fat to be cut off is controlled by a series of stamps pressing onto the skin surface of the pig back. Initial studies have revealed a need for knowledge about the tissue deformation induced by these stamps in order to insure that the fat layer is trimmed properly. This knowledge should be provided through analysis of CT images and deformation modelling. We study a simplified version of the stamps of the machine, by examining tissue deformation induced by pressure from a single bolt in a region of interest (ROI) covering the longissimus (loin muscle).

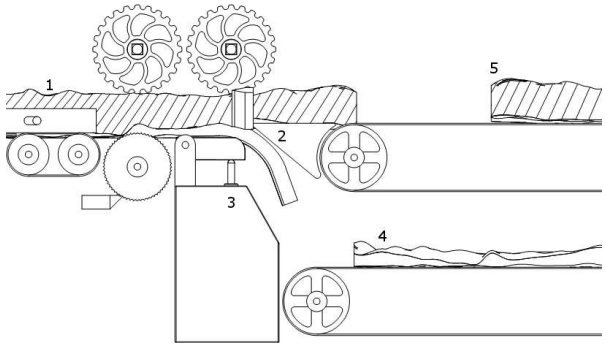

Figure 7.1: Conceptual drawing of the machine for trimming the fat layer on pig backs to a given thickness. Main items are labelled with numbers. 1; unprocessed pig back, 2; horizontal knife, 3; stamps, 4; excess fat, 5; processed pig back.

7.1.1 Related Work

Knowledge of tissue deformation is important in several areas of medical imaging. Examples include the development of haptic interfaces in simulators for surgical training, where realistic feedback is important, as well as robotics for interaction with soft tissue, enabling prediction of subject behaviour during handling. The latter is also a relevant field of research for industrial applications.

Famaey and Sloten [32] present an overview of physically founded tissue deformation models based on continuum mechanics for applications related to surgical simulations and robotics. Oomens et al. [91] and Then et al. [113]

apply such models in relation to studies of pressure sores. A common approach is to use finite element analysis to implement such models, with experimentally defined constants characterising the material stiffness. Another method is to use geometry-based models such as basis function. Wachowiak et al. [117] use radial basis functions (RBFs) in an application for real-time modelling of simulated needle insertion in prostate brachytherapy. As human tissue can be complex and often consists of layers of different tissues with ligaments and fascias, forming realistic models this way can be a difficult task.

In this paper, we present a method for building an empirically derived tissue deformation model using basis functions. We place markers inside the tissue to enable automatic generation of very reliable landmarks. By monitoring the movement of the landmarks through CT images, we gain understanding of the deformation induced by external forces. The markers hold the ground truth for the deformation at the given location and enable validation of the model to be performed.

7.1.2 Data

This work includes 10 pig backs with steel markers inserted. Using a syringe, steel markers with a diameter of 0.5 mm diameter are injected into the soft tissue through the skin. The markers are aimed to be positioned in a three-dimensional regular grid covering the ROI. Due to the difference in subject size, the number of markers inserted varies between 113 and 140. The pressure-bolt for inducing the tissue deformation is mounted on a nylon plate in a metal frame. The subject is placed with the skin side down on this plate, such that the centre (yz) of the ROI is at the bolt tip. A soft cushion is placed on top of the subject to prevent unintentional movement during image acquisition. Figure 7.2 shows a photo of the setup. We make two scans for each subject; one without any deformation induced, and one with the bolt pressed 20 mm down onto the skin surface. Figure 7.3 shows corresponding images of the same subject; before and after tissue deformation has been induced. The scans are made with in-plane resolution 0.9375 mm $\times$ 0.9375 mm and 1 mm slice thickness.

7.2 Methods

As seen in figure 7.3, the injected steel markers give rise to high image intensity in the CT images. As the ROI in each subject consists of soft tissue only, we extract the marker positions as points by applying an intensity threshold. To

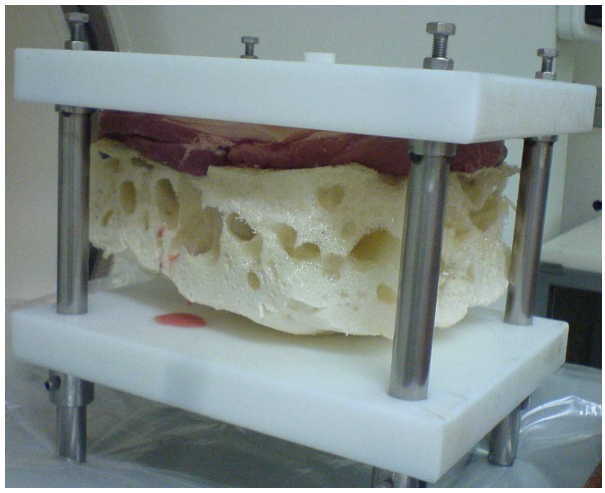

Figure 7.2: The experimental setup with nylon plates, metal frame and soft cushion underneath the meat. The top of the pressure-bolt (white) is just visible above the plate. On the photo the setup is turned upside down for proper adjustment of the bolt between two CT scans.

find correspondences between marker positions within subjects before and after the deformation has been induced, we use the Hungarian Method[69]; matching points by minimising the sum of pairwise Euclidean distances. This results in 10 sets of n_s point pairs in $d = 3$ dimensions holding information on the tissue deformation. We denote the initial marker positions and corresponding displacements $\mathbf{p}_s$, $\mathbf{q}_s \in \mathbb{R}^{n_s \times d}$. That is, markers extracted from the second images are placed in $\mathbf{p}_s + \mathbf{q}_s$.

7.2.1 Deformation Parameterisation

No point-correspondences can be derived between the 10 subjects due to the difference in both number and position of the markers. Therefore the observed displacements are converted into a common parameterisation to enable comparison and modelling of the tissue deformation. This parameterisation is closely related to the task of point-based registration; determining a geometrical transformation $\mathbf{u}$ aligning point pairs. Regarding $\mathbf{u}$ as a function of some parameters $\mathbf{x} \in \mathbb{R}^{d \cdot n_k}$ — that is, $\mathbf{u} : \left(\mathbb{R}^d, \mathbb{R}^{d \cdot n_k}\right) \to \mathbb{R}^d$. We wish to estimate the displacements $\hat{\mathbf{q}}_s = \mathbf{u}(\mathbf{p}_s, \mathbf{x}_s)$. By using the same parameterisation for all subjects we can later compare tissue deformations by comparing the transformation parameters.

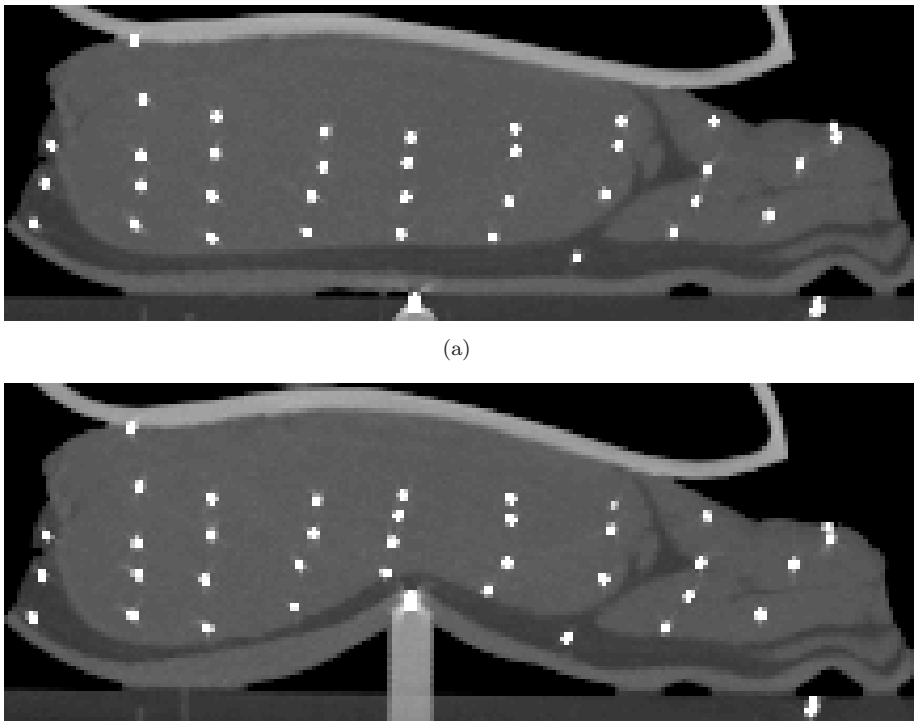

(a)

(b)

Figure 7.3: (a) and (b) show the same subject before and after the bolt has been pressed 20 mm onto the skin surface to induce tissue deformation. The images are maximum intensity projections of 10 adjacent slices in the CT images for a better two-dimensional visualisation of the steel markers, since the deformation is three-dimensional. The high intensity of the markers makes them clearly distinguishable from the surrounding soft tissue. A marker on the bolt tip and one on the frame are also visible.

Initially each point set is centred around the bolt to bring the deformations into a common coordinate system. Furthermore any difference in rotation of the setup is accounted for with a point-based rigid registration of markers placed on the bolt-frame (thus not affected by the induced tissue deformation).

For each set of $\mathbf{p}_s$ and $\mathbf{q}_s$ the parameters corresponding to the tissue deformation $\mathbf{x}_s$ are determined by minimising a cost function consisting of the sum of n_s squared pairwise Euclidean distances between true displacements and estimated displacements. Omitting the subscript s for simplicity, we write;

$$\underset{\mathbf{x}}{\operatorname{argmin}} \sum_{i=1}^{n} \|\mathbf{q}_i - \mathbf{u}(\mathbf{p}_i, \mathbf{x})\|^2. \tag{7.1}$$

As geometrical transformation function $\mathbf{u}$ we use a specific type of RBFs with compact support as introduced by Wendland[119]. In this work we adopt an approach similar to the one described by Fornefett et al. [37]. The basis functions are defined from at set of n_k knot points $\mathbf{c} \in \mathbb{R}^{n_k \times d}$ covering the ROI. The RBFs used allow for modelling of tissue deformation occurring locally as the influence of each basis function decreases with growing distance from the respective knot point.

Taking the dimensions of the transformation separately, we have; $u : \left(\mathbb{R}^d, \mathbb{R}^{n_k}\right) \rightarrow \mathbb{R}$. The function u is a weighted sum of n_k RBFs, ψ, with the parameters $\mathbf{x}$ as weighting coefficients. For a single point $\mathbf{p}_i$ we model the displacement in one direction by

$$u(\mathbf{p}_i, \mathbf{x}) = \sum_{j=1}^{n_k} x_j \psi(r_j), \tag{7.2}$$

where each r_j is defined with respect to knot $\mathbf{c}_j$, as the Euclidean distance $r_j = \|\mathbf{p}_i - \mathbf{c}_j\|$. In dimension $d > 0$ and smoothness $k \geq 0$ a unique basis function exists; $\psi_{d,k} \in C^{2k}(\mathbb{R})$. For $d = 3$ the first three are

$$\psi_{3,0} = (1 - r)_+^2 \tag{7.3}$$

$$\psi_{3,1} = (1 - r)_+^4 (4r + 1) \tag{7.4}$$

$$\psi_{3,2} = (1 - r)_+^6 (35r^2 + 18r + 3)), \tag{7.5}$$

with $(1 - r)_+^l = (1 - r)^l$ for $0 \leq r \leq 1$ and 0 for $r > 1$. The spatial support can be governed by a scaling parameter $a > 0$; $\psi(r) \equiv \psi(r/a)$. That is, a basis function has zero effect on points further away than r/a from the knot. In matrix notation a linear system for approximating a vector of displacements using equation (7.2) can be written as

$$\hat{\mathbf{q}} = \mathbf{A}\mathbf{x}, \tag{7.6}$$

where $\mathbf{A}$ is a matrix of basis function values with elements $\{A\}_{ij} = \psi_{d,k}(||\mathbf{p}_i - \mathbf{c}_j||)$. We can handle displacements for all three directions in one step;

$$\begin{bmatrix} \hat{\mathbf{q}}_x \\ \hat{\mathbf{q}}_y \\ \hat{\mathbf{q}}_z \end{bmatrix} = \begin{bmatrix} \mathbf{A} & \mathbf{0} & \mathbf{0} \\ \mathbf{0} & \mathbf{A} & \mathbf{0} \\ \mathbf{0} & \mathbf{0} & \mathbf{A} \end{bmatrix} \begin{bmatrix} \mathbf{x}_x \\ \mathbf{x}_y \\ \mathbf{x}_z \end{bmatrix}. \tag{7.7}$$

With fewer knots than points $n_k < n_s$, we can then find the optimal $\mathbf{x}$ which estimates the observed marker displacements by minimising a cost function f of least squared differences, cf. equation (7.1);

$$f = \frac{1}{2}(\mathbf{q} - \mathbf{A}\mathbf{x})^T(\mathbf{q} - \mathbf{A}\mathbf{x}). \tag{7.8}$$

The accuracy of this parametric representation is illustrated in figure 7.4; marker positions in the deformed tissue are calculated using the estimated optimal parameters and plotted on a corresponding maximum intensity projection (MIP). Regarding these estimates of all 1282 markers injected in the 10 subjects, the parameterisation yields an absolute error with mean 0.20 mm, median 0.13 mm, and standard deviation 0.21 mm.

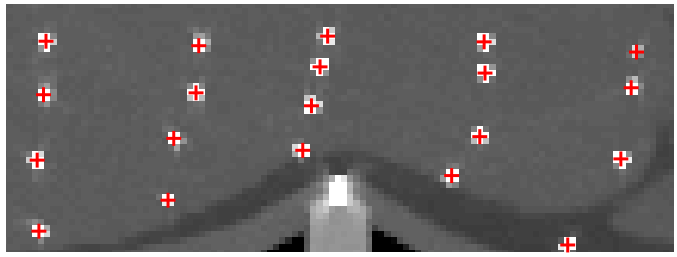

Figure 7.4: Close-up view of the maximum intensity projection of figure 7.3(b). The crosses indicate marker positions achieved by the deformation parameterisation and the estimated optimal parameters.

With these parameter estimates we can interpolate the tissue deformation between the markers. For voxel positions within the ROI spanned by the markers, we construct a new matrix of basis-function values using the same knots as for the parameter estimation. The displacements can then be computed using equation (7.7), allowing us to *re-enact* the tissue deformation observed. In figure 7.5 this is shown as estimated displaced positions from a regular grid superimposed on an MIP of the corresponding deformed tissue.

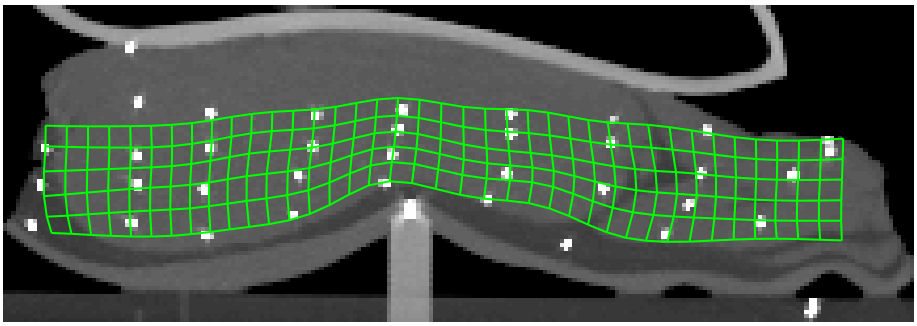

Figure 7.5: Estimated displaced voxel positions from a regular grid (5 mm spacing) superimposed on the maximum intensity projection of figure 7.3(b).

7.2.2 Statistical Deformation Model

For the estimated deformation parameters to be comparable between subjects, the parameterisation must be the same. Therefore in all subjects, we place knot points in a common grid structure centred around the bolt. This means that the value of the ith element in all estimated parameter vectors corresponds to the same deformation direction and same knot position relative to the origin of the tissue deformation. We use this property to build a statistical model of the tissue deformation using principal component analysis (PCA), the approach is inspired by statistical shape models [23].

The parameter vector $\mathbf{x}$ is regarded as a Gaussian-distributed random variable with $d \cdot n_k$ elements. Our $N = 10$ estimates are then treated as observations with mean

$$\bar{\mathbf{x}} = \frac{1}{N} \sum_{s=1}^{N} \mathbf{x}_s. \tag{7.9}$$

Centered around this mean, the covariance matrix $\mathbf{\Sigma}$ is estimated as

$$\mathbf{\Sigma} = \frac{1}{N-1} \sum_{s=1}^{N} (\mathbf{x}_s - \bar{\mathbf{x}})(\mathbf{x}_s - \bar{\mathbf{x}})^T, \tag{7.10}$$

with eigenvalues sorted so they are non-increasing $\lambda_1, \lambda_2, \ldots, \lambda_{d \cdot n_k}$ and corresponding eigenvectors gathered in an orthonormal matrix $\mathbf{P} = [\mathbf{P}_1 \mathbf{P}_2 \cdots \mathbf{P}_{d \cdot n_k}]$. These *principal modes* make up our deformation model

$$\mathbf{x} = \bar{\mathbf{x}} + \mathbf{P}'\mathbf{b}, \tag{7.11}$$

approximating a deformation parameter vector as the sum of the mean and a linear combination of the l first eigenvectors $\mathbf{P}'$ with coefficients $\mathbf{b} \in \mathbb{R}^l$. This

formulation gives the possibility of a compact representation of the most general tendencies in the tissue deformation. The share of total variance explained by a single principal mode $\mathbf{P}_i$ is equal to the size of the corresponding eigenvalue normalised by the total sum of all eigenvalues, $\lambda_i / \sum_{j=1}^{d \cdot n_k} \lambda_j$.

7.3 Validation

To validate the model, we use leave-one-out cross validation with the PCA to estimate the prediction error. That is, we assess the amount of the tissue deformation in each subject that can be expressed using the remaining 9. For each subject s the mean $\bar{\mathbf{x}}_s$ and matrix of principal modes $\mathbf{P}_{cv,s}$ are calculated using all parameter vectors except the sth. Using some subset of the modes $\mathbf{P}'_{cv,s}$ we wish to find the coefficients $\mathbf{b}_s$, that minimise the cost function

$$f = \frac{1}{2} \left(\mathbf{q} - \mathbf{A} \left(\bar{\mathbf{x}}_s + \mathbf{P}'_{cv,s} \mathbf{b}_s \right) \right)^T \left(\mathbf{q} - \mathbf{A} \left(\bar{\mathbf{x}}_s + \mathbf{P}'_{cv,s} \mathbf{b}_s \right) \right). \tag{7.12}$$

The optimal $\mathbf{b}_s$ is then used to form the corresponding deformation parameter vector $\mathbf{x}_s$ by equation (7.11) with $\bar{\mathbf{x}}_s$ and $\mathbf{P}'_{cv,s}$. This is done several times for all subjects varying the modes used in $\mathbf{P}'_{cv,s}$. To evaluate the performance of the model, we consider the absolute error of the marker displacement estimates.

Figure 7.6 shows histograms and corresponding descriptive statistics for errors achieved with the different mode-setups. As the errors are based on 10 models estimated using 9 observations each, it is only sensible to use up to 8 principal modes. The *8-mode model* does not provide error-measures as low as the full parameterisation. However, the two sets of measures should be compared with caution as the parameterisation errors are not achieved with cross validation. The errors of the model indicate that each observation contains some variation that is not present in the remaining 9 used for the cross validation. An explanation for this could of course be the anatomical variation between subjects, but a possible difference in the applied pressure — e.g. positioning of the bolt — is also a plausible cause. Using a larger number of subjects would make the model more capable of handling the variations, but this would also introduce more variation not originating from the tissue deformation itself.

As expected the mean and median error decrease when more modes are included. It is not obvious how many modes to retain. However, the small number of observations implies using only a small number of modes, and thus only modelling the most general deformation. Figure 7.7 relates the mean and median error to the number of principal modes. The largest *kink* on the curve of the mean is located between 1 and 2, suggesting the choice of a model with only the first

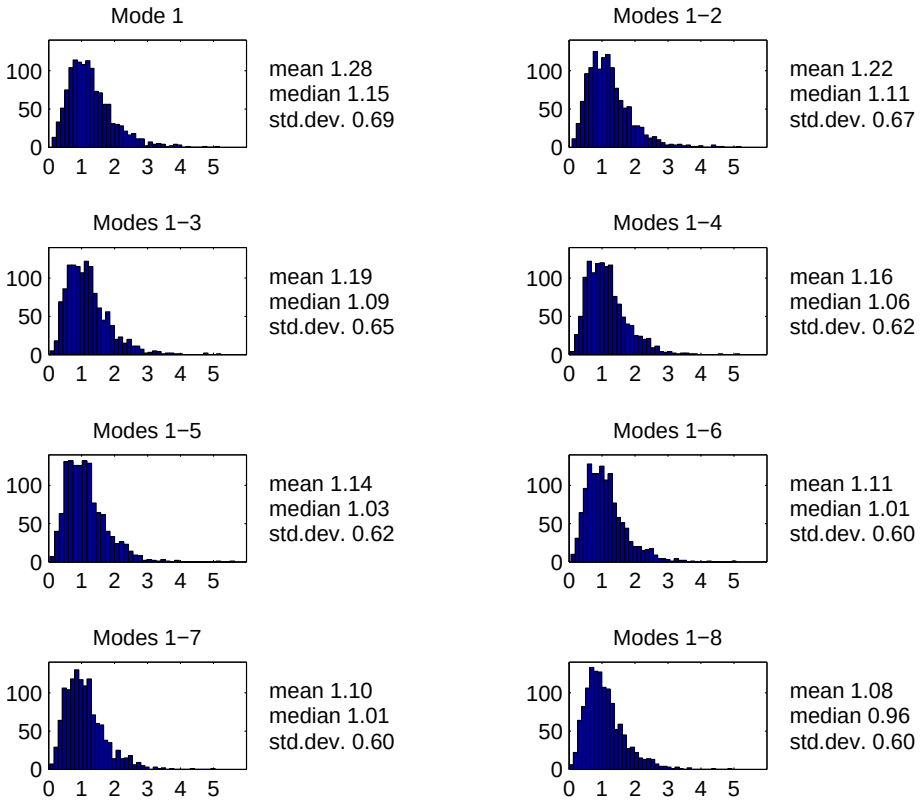

Figure 7.6: Histograms and corresponding descriptive statistics of the absolute errors (in mm) for all markers in all subjects; achieved by leave-one-out cross validation using different subsets of principal modes in the statistical deformation model.

two principal modes. This would result in a model with a mean absolute error of 1.22 mm, median 1.11 mm and standard deviation 0.67 mm. Comparison of the magnitudes of the error and the voxel dimensions of the images used, shows that our empirically derived statistical tissue deformation model is able to achieve a sufficient level of precision.

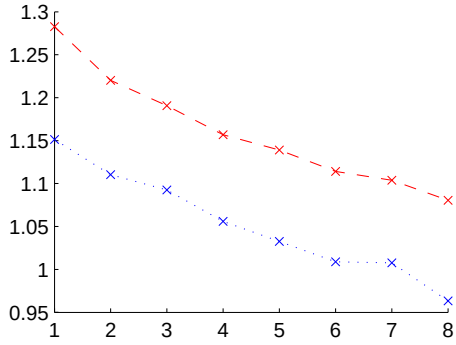

Figure 7.7: Plot relating mean and median of the absolute error (dashed and dotted respectively) to the number of principal modes used in the model.

7.4 Discussion

We present a method for empirically deriving a soft tissue deformation model from CT images of 10 pig backs with steel markers injected. The tissue deformation is parameterised using radial basis functions with compact support defined on a grid of knots. The parameterisation yields an absolute error of marker displacement estimates with mean 0.20 mm, median 0.13 mm and standard deviation 0.21 mm. We derive a statistical deformation model using principal component analysis on the estimated parameters. The model is successfully validated using leave-one-out cross validation by subject repeated for different subsets of the principal modes. Retaining only the first two modes we achieve a sufficient level of precision; mean 1.22 mm, median 1.11 mm and standard deviation 0.67 mm. The use of steel markers injected into the soft tissue enables automatic generation of the accurate landmarks used to build the tissue deformation model through the parameterisation. The markers hold the ground truth for the deformation at the given location. This enables very reliable validation.

Chapter 8

An Efficient Data-driven Tissue Deformation Model

Thomas Hammershaimb Mosbech, Bjarne Kjær Ersbøll and Lars Bager Christensen

Abstract

In this paper we present an efficient data-driven tissue deformation model. The work originates in process automation within the pig meat processing industry. In the development of tools for automating accurate cuts, knowledge on tissue deformation is of great value. The model is built from empirical data; 10 pig carcasses are subjected to deformation from a controlled source imitating the cutting tool. The tissue deformation is quantified by means of steel markers inserted into the carcass as a three-dimensional lattice. For each subject marker displacements are monitored through two consecutive computed tomography images — before and after deformation; tracing corresponding markers provides accurate information on the tissue deformation. To enable modelling of the observed deformations, the displacements are parameterised applying methods from point-based registration. The parameterisation is based on compactly supported radial basis functions, expressing the displacements by parameter sets comparable between subjects. For modelling the tissue deformation, principal component analysis is applied, treating each of the parameter sets as an observation. Using leave-one-out cross-validation, marker displacements are estimated in all subjects from the mean parameters. This yields an absolute error with mean 1.41 mm. The observed lateral movement of the loin muscle is analysed in relation to the principal modes, and the results are compared to manual measurements of carcass composition. We find an association between the first principal mode and the lateral movement. Furthermore, there is a link between this and the ratio of meat-fat quantity — a poten-

tially very useful finding since existing tools for carcass grading and sorting measure equivalent quantities.

8.1 Introduction

In the meat industry there is increasing interest in developing tools for process automation. The traditional manual slaughtering procedures give rise to a labour-intensive working environment with physically demanding tasks and repetitive work performed under pressure. The goals of efficient automated processing include safer and faster production, better hygiene, more uniform quality of the end products, and in the end, better returns for abattoirs.

Existing automation tools in pig meat production include systems for classifying and sorting carcasses, as well as robotics for evisceration, carcass cutting, boning and trimming various parts. Technologies currently used here are mostly computer vision and ultrasonics [75, 90]. An upcoming technology in automation is the use of computed tomography (CT) to achieve detailed information on the raw materials. Both in measuring general tendencies of populations, but also for on-line use in the abattoirs.

One hurdle in the development of the robotics is to handle the large biological variation present in the raw material — automatically adapting the processing to each individual subject. Within this area, an important topic is prediction of subject behaviour during handling, e.g. fixing a piece of meat for cutting can induce tissue deformations making it difficult for the machine to perform accurate cuts.

In this paper we use CT images as guidance in the development of a tool for processing pig backs to produce bacon with a given fat-layer thickness; homogeneous products from inhomogeneous raw materials. Figure 8.1 shows a 3-dimensional model of a pig back created from a CT image. Figure 8.1(a) shows the model with a distinction between the meat and the rind (facing down). Figure 8.1(b) shows the model after a 'virtual cut' has been performed, leaving only the rind. From the model we can see that the transition between fat and meat is far from smooth, thus a robot trimming the fat layer must be able to adjust to the shape of each individual subject [12].

Initial stages of the development process have identified the need for information on the tissue deformations caused by handling the pig back. Pressure from the knives trimming the rind tends to cause lateral movement in the loin muscle, making it difficult to perform accurate cuts. We study a simplified version of

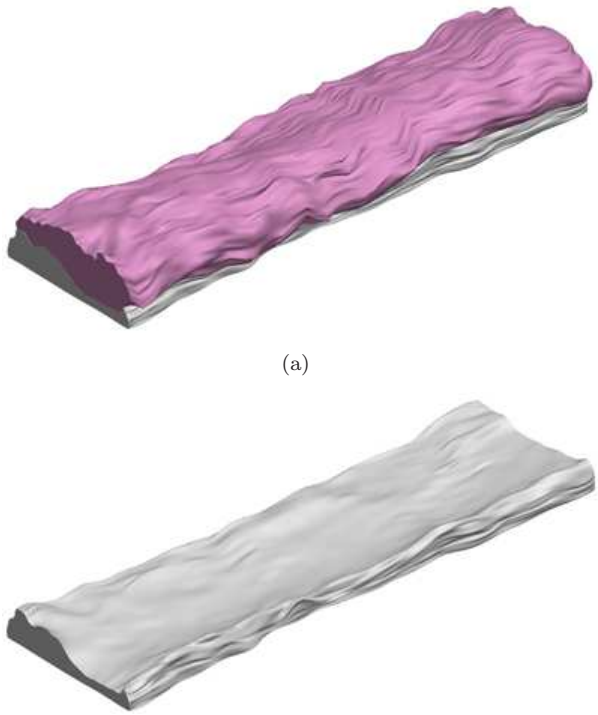

(a)

(b)

Figure 8.1: 3D model of a pig back created from a CT scan. (a) Model distinguishing between the loin and streaky (top) and the rind (bottom). (b) 'Virtual cut' showing only the rind layer; the variation of the contours in the transition between meat and rind is evident.

this by applying pressure from a single bolt on the skin surface and examining the induced tissue deformation in the area around the loin.

Tissue deformation modelling is a widespread area of research within medical imaging, e.g. haptic interfaces with realistic feedback used in simulation tools for surgical training.

A widely used approach for implementing these models is the use of finite element methods with material properties determined from both *in vivo* and *ex vivo* experiments. A thorough overview of such continuum-mechanical models is presented by Famaey and Sloten in [32] in relation to applications in virtual surgery and surgical robotics. Another approach is the use of basis functions to model tissue deformations — a method related to image registration, forming the warp function as sums of smooth basis functions. Wachowiak et al. [117] describe an application to needle insertion simulation in prostate brachytherapy using radial basis functions with compact support.

Recently, Mosbech et al. [79] presented a method for accurate quantification of soft tissue deformation, they proposed a technique based on CT images of soft tissue with inserted steel markers. We use this method in our data-driven analysis of tissue deformation. Markers are placed inside the tissue and the tissue is subjected to deformation. The resulting marker movements are monitored using CT imaging, enabling automatic generation of accurate landmarks. The observed landmark displacements are then used to analyse the induced soft tissue deformation.

8.2 Data Acquisition

For the experiments we used 10 pig backs of varying size and composition (quantity of fat and meat). In each subject a number of steel markers were inserted with a syringe through the skin. The steel markers had a diameter of 0.5 mm. The insertions were performed such that the markers resembled a 3-dimensional lattice of approximately 180 mm $\times$ 40 mm $\times$ 70 mm. The number of inserted markers varied between 113 and 140 because of different subject sizes.

We mounted the bolt for inducing the tissue deformation on a nylon plate. Each pig back subject was put on the plate with the rind-side facing down. The subject was aligned, such that the bolt was positioned on the skin in the middle of the lattice of injected markers. On the meat-side of the subject we placed a soft cushion to prevent the subject from being dislodged unintentionally. For each subject we did two consecutive CT scans; one without any deformation

induced by the bolt, and one pressing the bolt 20 mm against the skin surface.

The images were acquired with approximately isotropic voxels; 0.9375 mm × 0.9375 mm, with a slice thickness of 1 mm. Figure 8.2 shows examples of the image data.

8.3 Methods

Compared to the surrounding soft tissue, the steel markers lead to very high intensities in the CT images. The positions can therefore be extracted accurately by intensity thresholding.

For each subject this gives two point sets of size n in $d = 3$ dimensions; $\mathcal{P}$ and $\mathcal{Q} \in \mathbb{R}^{n \times d}$, holding marker positions retrieved from the two images with and without deformation, respectively.

To automatically achieve point-correspondences *within* each subject, we apply the Hungarian Algorithm [69], matching point pairs in the two sets by minimising the sum of the Euclidean distances.

As the 10 resulting sets of pairs differ in both size and marker positions, no point-correspondences can be established *between* subjects. Thus the tissue deformations contained in the marker displacements are difficult to compare across subjects. To facilitate comparison we parameterise the marker displacements, bringing them into a common reference frame.

The parameterisation can be regarded as a task from point-based registration; determining a geometrical transformation aligning point-pairs by estimating displacements. We formulate this alignment of two corresponding points $\mathbf{p}_i \in \mathcal{P}$ and $\mathbf{q}_i \in \mathcal{Q}$ as a function ϕ of parameters $\mathbf{x} \in \mathbb{R}^{d \cdot n_k}$

$$\phi(\mathbf{p}_i, \mathbf{x}) = \mathbf{p}_i + \mathbf{u}(\mathbf{p}_i, \mathbf{x}) \tag{8.1}$$

modelling the displacements by the parametric transformation $\mathbf{u} : \left(\mathbb{R}^d, \mathbb{R}^{d \cdot n_k}\right) \rightarrow \mathbb{R}^d$.

The transformation is composed of a sum of basis functions ψ defined on a set of knot points $\mathcal{C} \in \mathbb{R}^{n_k \times d}$ all within the spatial range of $\mathcal{P}$. For a single point the displacement in one direction is the sum of n_k basis functions

$$u(\mathbf{p}_i, \mathbf{x}) = \sum_{j=1}^{n_k} x_j \psi(r_j), \tag{8.2}$$

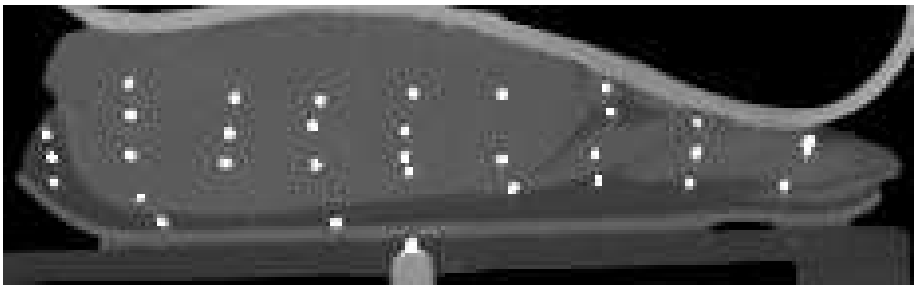

(a)

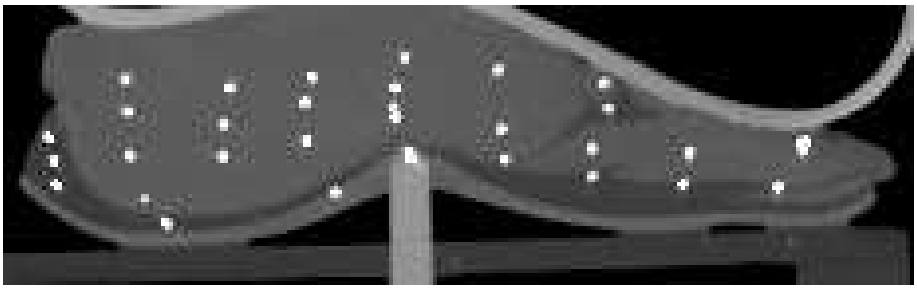

(b)

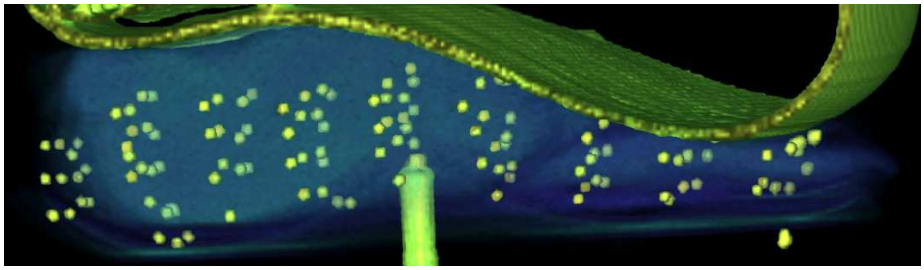

(c)

Figure 8.2: (a) and (b) MIPs of the slices around the bolt showing the subject without and with deformation. The high intensity of the markers makes them distinguishable from the low-intensity soft tissue. The high intensity band at the top is the air-filled soft cushion. (c) Three-dimensional visualisation of the deformed image, the view is slightly rotated and the opacity of the soft tissue has been decreased to illustrate the marker grid structure.

where $r_j = \|\mathbf{p}_i - \mathbf{c}_j\|$; the Euclidean distance between the point $\mathbf{p}_i \in \mathcal{P}$ and knot $\mathbf{c}_j \in \mathcal{C}$.

As basis functions we use a certain type of radial basis function with compact support $\psi_{d,k} \in C^{2k}(\mathbb{R})$ as introduced by Wendland [119]. In [37] Fornefett et al. describe an application of these functions to model deformations in relation to registration of medical images. For dimension $d = 3$ and smoothness $k = 2$ the Wendland-basis function is formulated as

$$\psi_{3,2} = (1 - r)_+^6 (35r^2 + 18r + 3). \tag{8.3}$$

In this univariate polynomial, the compact support is controlled by $(1 - r)_+^l = (1 - r)^l$ for $0 \leq r \leq 1$ and 0 for $r > 1$. A parameter $a > 0$ can be applied for scaling this locality; $\psi(r) \equiv \psi(r/a)$. That is, the global effect of ψ increases with a, as all points within distance a from a particular knot are affected.

The optimal vector of parameters $\mathbf{x} \in \mathbb{R}^{n_k}$ to represent one direction of the tissue deformation contained in all pairs in $\mathcal{P}$ and $\mathcal{Q}$ for one subject is determined by minimising a sum of n squared pair-wise Euclidean distances between observations and estimates

$$\underset{\mathbf{x}}{\operatorname{argmin}} \sum_{i=1}^{n} \|\mathbf{q}_i - \phi(\mathbf{p}_i, \mathbf{x})\|^2. \tag{8.4}$$

With (8.1) and (8.2) we can construct the estimates as a linear system of equations

$$\hat{\mathbf{q}} = \mathbf{p} + \mathbf{A}\mathbf{x}, \tag{8.5}$$

where $\mathbf{p}, \hat{\mathbf{q}} \in \mathbb{R}^n$ and $\mathbf{A}$ is an $n \times n_k$ matrix of basis function values $\{A\}_{ij} = \psi_{d,k}(||\mathbf{p}_i - \mathbf{c}_j||)$. The system can be expanded to estimate displacements in all three dimensions;

$$\hat{\mathbf{q}} = \mathbf{p} + \begin{bmatrix} \mathbf{A} & \mathbf{0} & \mathbf{0} \\ \mathbf{0} & \mathbf{A} & \mathbf{0} \\ \mathbf{0} & \mathbf{0} & \mathbf{A} \end{bmatrix} \mathbf{x}, \tag{8.6}$$

with $\mathbf{p}, \hat{\mathbf{q}} \in \mathbb{R}^{d \cdot n}$ and parameters $\mathbf{x} \in \mathbb{R}^{d \cdot n_k}$. This can be solved using standard optimisation techniques, e.g. by minimising the cost function equivalent to (8.4) w.r.t. $\mathbf{x}$

$$f = \frac{1}{2} \left(\mathbf{q} - (\mathbf{p} + \mathbf{A}_0\mathbf{x})\right)^T \left(\mathbf{q} - (\mathbf{p} + \mathbf{A}_0\mathbf{x})\right) \tag{8.7}$$

where $\mathbf{A}_0$ is the block diagonal matrix of (8.6).

This parametric representation of the observed marker displacements enables estimation of the tissue deformation between the markers. Applying the same basis function parameters and set of knot points, the $\mathbf{A}$ matrix of (8.5) is computed with respect to these new points of interest (e.g. all voxel positions). The

parameters can then be plugged into (8.6) for computing the displacements. Figure 8.3 shows an example.

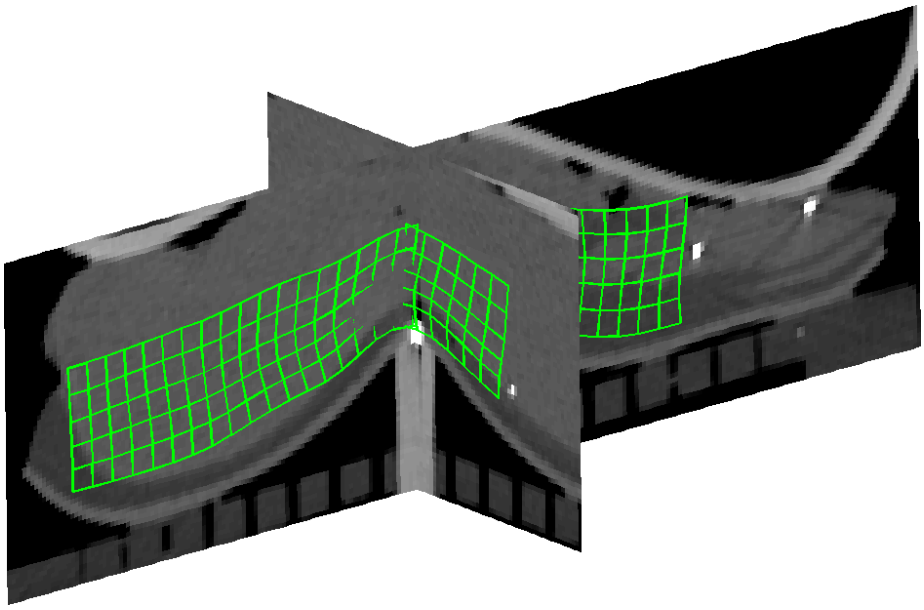

Figure 8.3: A mesh of points with 5 mm spacing deformed under the estimated parameters. The mesh is superimposed on two planes of the CT image. As the deformation is three-dimensional, part of the grid is disappears into the image slice from this perspective.

8.4 Analysis

As mentioned earlier, the $N = 10$ tissue deformations are comparable by means of their parameter vectors, when the same parameterisation has been applied on all subjects. This implies using the same values of a, d and k, but also a common knot set-up $\mathcal{C}$. To handle this knot-setup, a steel marker placed on the tip of the pressure bolt is used as origin for consistent positioning of the knot-grid on all subjects.

We analyse the variability of the estimated parameters by applying principal component analysis (PCA), building a general model with methods from statistical shape modelling [23].

Regarding each of the estimated parameter vectors as an observation of a random variable, we estimate the mean

$$\bar{\mathbf{x}} = \frac{1}{N}\sum_{s=1}^{N}\mathbf{x}_s, \tag{8.8}$$

and calculate the covariance matrix of the parameters with the mean subtracted

$$\mathbf{\Sigma} = \frac{1}{N-1}\sum_{s=1}^{N}(\mathbf{x}_s - \bar{\mathbf{x}})(\mathbf{x}_s - \bar{\mathbf{x}})^T. \tag{8.9}$$

The eigenvectors and eigenvalues of $\mathbf{\Sigma}$ are then estimated, and the eigenvalues are sorted non-increasing; $\lambda_1 \geq \lambda_2 \geq \cdots \geq \lambda_{d\cdot n_k}$. The corresponding eigenvectors are gathered in a matrix forming an orthonormal basis; $\mathbf{P} = [\mathbf{P}_1\mathbf{P}_2\cdots\mathbf{P}_{d\cdot n_k}]$. These vectors are the principal modes forming the model for approximating a parameter vector; adding the mean and a linear combination of modes

$$\mathbf{x} = \bar{\mathbf{x}} + \mathbf{P}'\mathbf{b}', \tag{8.10}$$

where $\mathbf{P}'$ is a subset of $\mathbf{P}$ containing the l first modes, and $\mathbf{b}' \in \mathbb{R}^l$ is the model parameters.

Using leave-one-out cross-validation, N models are estimated — each from $N-1$ observations. We assess the generality of the model by considering the simplest model consisting of the mean deformation parameters only. Instead of applying the transformations on regular grids as shown in figure 8.3, we apply them to the set of marker positions corresponding to the parameter set left out in building the model. In this way we can estimate the prediction error of the model, comparing estimated and observed displacements. This yields an absolute error of 1.41 ± 0.87 mm — comparable to the voxel size of the images.

To examine the effects of the modes in detail, the zero-mean parameter vector is projected onto the full set of modes

$$\mathbf{b} = \mathbf{P}^T(\mathbf{x} - \bar{\mathbf{x}}), \tag{8.11}$$

the deformation parameters are then reconstructed using only the model parameters and modes of interest as in (8.10).

We take an approach slightly different from the model formulated in (8.10) and (8.11). No cross-validation is applied, and the mean is disregarded, as its effect on the deformations is common for all observations. In the PCA model the amount of the data set's variation represented by the ith mode is proportional to the relative size of the ith eigenvalue. The graph in figure 8.4 relates the number of modes in the model to the percentage of variance explained. We

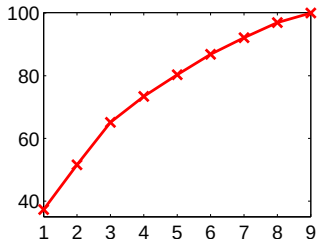

Figure 8.4: Graph showing the percentage of variance explained by the principal modes. The nine first modes are used to explain all of the variance, as the model is built from 10 observations.

show only the first nine modes — explaining the full variance — as the model is built from 10 observations.

The three first modes cover approximately two-thirds of the total variance. With the approach described above, we examine the effect on the tissue deformation of each of the modes individually. Figure 8.5 shows an example of the results; using the reconstructed deformation parameters, we calculate displacements for a grid of points — covering the range of the knots and markers — and visualise them as arrows superimposed on the corresponding image slice.

For the first three modes, the estimated displacements show no general tendencies in the *streaky*-part of the backs (rightmost on the example in figure 8.5). As this part exhibits a highly variable anatomical structure throughout the 10 subjects, it is difficult for the model to generalise these deformations.

Regarding the estimated point displacements in the loin muscle, the first mode — explaining 37 % of the total variance — shows a relation to the degree of lateral movement for all subjects. The movement appears to be most profound in the tissue around the tip of the pressure bolt, but on some subjects it propagates even further into the muscle. As mentioned in the introduction, this lateral movement is of particular interest in the development of automated tools for precise rind trimming. The movement complicates the process of producing a product with a given fat layer thickness.

We focus the analysis on this first principal mode and examine the resulting displacements of points within the loin muscle and in the rind layer beneath it. The points are selected by means of manual segmentations of the loin muscle.

Existing carcass grading systems are capable of performing measurements of the fat and loin muscle thickness [21], so it is sensible to use these two measurements

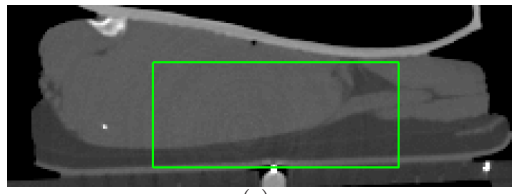

(a)

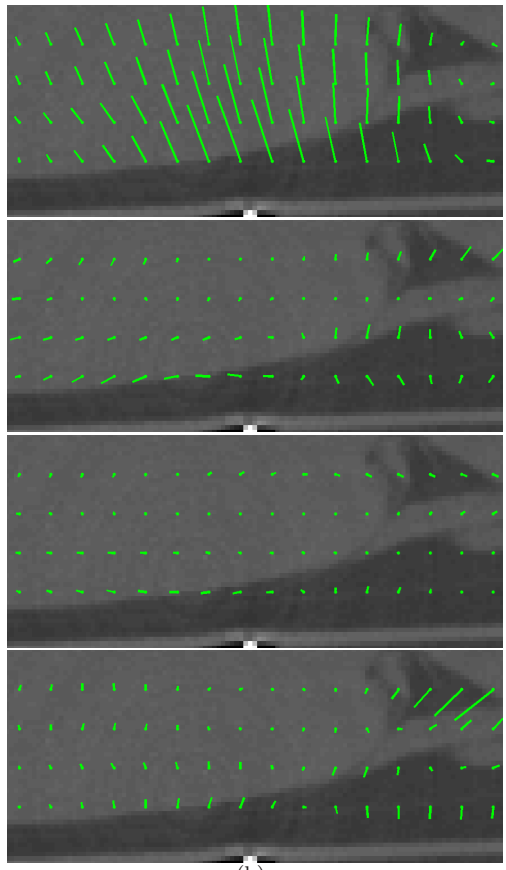

(b)

Figure 8.5: The effect of the mean and each of the three first principal modes. (a) The displacements are illustrated on a single slice zoomed to a region around the pressure bolt containing parts of the streaky (right) and loin muscle (left). (b) Four slices; the displacements are estimated for a grid of points and shown as lines superimposed on the image (from top to bottom; mean, modes 1, 2 and 3). For illustrative purposes the lines corresponding to the three single modes have been magnified by a factor of five.

to characterise the carcass composition of the subjects — that is, for each subject we also perform a manual segmentation to assess the mean fat layer thickness. Figure 8.6 relates the estimated lateral movements to the ratio between loin size and mean fat layer thickness. For subjects 2 and 9 — with notable positive displacement means — the loin muscle is not moving to the right, since the left-directed deformation contained in the mean is disregarded in the analysis. From the figure we see, that the lateral movement differs clearly from the rest on the most lean and fat subjects. This indicates the possibility of sorting the pig backs by means of the loin-fat ratio and discriminating the processing — e.g. by applying uneven pressure on the meat side to compensate for the lateral movement of the muscle.

8.5 Conclusion

This paper described an efficient method for data-driven modelling deformation of soft tissue. The model is based on three-dimensional computed tomography images of 10 pig carcasses subjected to deformation. The tissue deformation is accurately quantified by steel markers inserted into the carcass. The observed displacements from each subject are transformed into a common reference frame with a parametric representation of radial basis functions with compact support.

The derived parameters are compared using principal component analysis, forming a tissue deformation model. The generalisation of the model is assessed by estimating marker displacements from the mean parameters using leave-one-out cross-validation by subject. Across all subjects the model achieves an absolute error of 1.41 ± 0.87 mm. The first principal mode of the model covers 37% of the total variance in the data. This mode is associated with the lateral movement of the loin muscle. The magnitude of this movement is compared with measurements of carcass composition; the ratio between loin size and mean fat layer thickness. The comparison shows a link; lean carcasses exhibit a higher degree of lateral loin muscle movement compared to more fatty carcasses.

In pig meat production, the presented method can provide valuable knowledge in relation to developing tools for automated processing. Our analyses are of particular interest in relation to trimming the rind of pig backs producing a product with a given fat layer thickness.

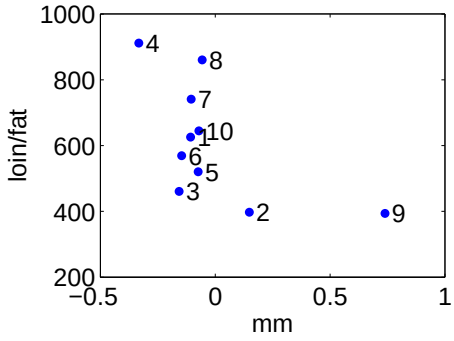

(a)

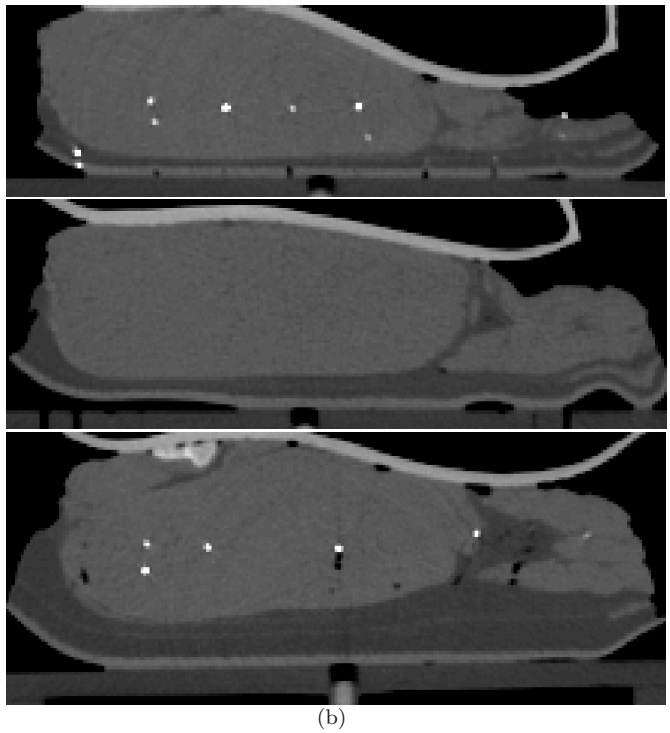

(b)

Figure 8.6: Analysing the first principal mode regarding displacements estimated for points within the loin muscle and in the fat layer beneath it. (a) Plot relating lateral movement (x-axis) and ratio between the manual measurements of loin size and mean fat layer thickness (y-axis). (b) Illustrating three different carcass compositions resulting in different lateral loin muscle movements. From top to bottom the slices are subjects 4, 1 and 9.

Chapter 9

BASE-CT: Bayesian Adaptive Structure Enriched Computed Tomography

Thomas Hammershaimb Mosbech, Daniela Calvetti, Erkki Somersalo, Lars Bager Christensen and Bjarne Kjær Ersbøll

Abstract

We present a method for computed tomography image reconstruction from sparse data; fan-beam X-ray projections acquired from a limited number of source positions. Reconstruction from a reduced amount of data can lead to lower radiation dose and cost — matters of high relevance for both medical and industrial applications. We formulate the inverse problem of tomographic reconstruction using Bayesian statistics, and compensate for the paucity of the subject-specific data by including a priori belief about the image content using an adaptive hyperprior. The image is reconstructed as the maximum a posteriori estimator, but the statistical formulation also allows an assessment of the image uncertainty by means of random sampling from the posterior distribution. The performance is illustrated on phantom data and an industrial imaging application; scanning pig carcasses for slaughtering.

9.1 Introduction

X-ray computed tomography (CT) is an imaging modality to acquire high contrast three-dimensional images of internal structures [65, 81, 82] which is very

popular in medical examination and industrial applications.

A CT image is a map of the attenuation factor distribution affecting X-rays traversing the object of interest, reconstructed from projections along source-detector lines. If a sufficiently large number of projections, covering the full angular range is available, it is possible to reconstruct the X-ray attenuation map analytically from the theory of line integrals [98]. The implementation of this approach via filtered back projection (FBP) [65] is the method of choice in most of the current full angle CT scanners.

However, complete projection data is not always available, or its acquisition may be too slow for some specific applications, hence the data may consist of few projections, and the projection angles may be limited. In medical applications, the use of few projections is an alternative to lowering the X-ray intensities, when reducing the radiation dose for the patient is of concern. In industrial applications, this acquisition scheme is attractive because of its speed, which usually translates into reduced cost.

When incomplete projection data are collected, the images reconstructed via FBP are contaminated by artifacts [99], therefore alternative approaches are needed. In this paper, we are concerned with the CT X-ray image reconstruction from few projections with the projection angles sparsely distributed over full angle. The paucity of data increases the ill-posedness of the reconstruction, because the number of unknowns in a finely discretized pixel image is typically much larger than number of observations. Our main motivation for adopting a statistical framework when solving this inverse problem is the possibility to augment the quantitative data with qualitative information about the sought solution.

In the statistical approach to the solution of inverse problems all unknown parameters to be estimated are regarded as random variables, hence described in terms of probability density functions rather than actual values. It is therefore natural to express any *a priori* belief about them through what is known in Bayesian terms as a prior probability density function. This is effectively a mean of compensating for the paucity, or poor quality, of data, and the approach has been shown to be quite effective in a variety of applications. The theoretical foundations of statistical inverse problems and several examples can be found in [17, 62].

The design of informative priors, that are also computationally efficient, is an important and challenging topic which has received a lot of attention recently. The construction of informative priors tends to be based on notions which are believed to be true about image content; this may include intensity ranges or particular structural features. A review of prior formulations in the context

of computed tomography along these guidelines can be found in [108], where the connection between specific types of priors and Tikhonov regularization is discussed. Of particular interest is the total variation (TV) penalty and its Markov random field characterization: the solution is expected to have a blocky structure, as is the case in [107], where an iterative image reconstruction algorithm based on the minimization of the image TV is presented.

In the Bayesian approach to the CT few projection problem in [56], a prior which is a mixture of gamma densities is applied to image reconstruction with few data, while Chen et al. [22] propose a reconstruction method for low-dose CT which combines Bayesian statistics with Markov random field (MRF) theory to design an adaptive-weighting nonlocal prior. In [58] it is shown that a prior based on the L_0 norm can be very effective for CT reconstruction from very sparse data.

In this work we follow the Bayesian approach to statistical inversion, and formulate an algorithm for CT image reconstruction from sparse projection data, referred to as the Bayesian adaptive structure enriched computed tomography (BASE-CT). With this Bayesian paradigm, the complete description of the reconstructed image is given by its posterior density, which is the conditional probability of the image given the measured data. This approach, which provides the entire posterior density function, allows us to produce single image estimates, if so desired. A popular choice in this regard is the *maximum a posteriori* (MAP) estimate, namely the most probable image according to the posterior. The added benefit of having the solution as a density, rather than a single image, is that sampling from the posterior provides a mean to assess the uncertainty that propagates onto the reconstructed image [18, 19]. The uncertainty estimation is addressed in this article.

The paper is organized as follows: section 9.2 reviews the basic concepts of CT, and formulates the image reconstruction as an inverse problem. In section 9.3 we set up the framework for the statistical inversion. More specifically, we construct a parameter dependent prior that is particularly effective for images known to contain well-defined structures of homogeneous intensities but whose location, size or form are unknown. The MAP-estimator of the reconstructed image is computed using an iterative algorithm which at each step updates the MAP estimate and the hyperparameters defining the prior. Additionally, we explore the joint posterior density of the image and the hyperparameters with a stepwise Gibbs-sampling algorithm. Section 9.4 illustrates the performance of BASE-CT by means of computed examples: phantom data and images of pig meat for an industrial application in the abattoir. The paper is concluded by section 9.5 with discussions and closing remarks.

9.2 Computed Tomography

The use of computerized tomography for non-invasive imaging of the inner structures of objects has enjoyed vast popularity since its introduction a few decades ago. The modality aims at reconstructing the absorption coefficients of the body at each spatial location from measured attenuations of X-rays having passed through the object from different directions through a system of emitters and detectors. An X-ray, emitted from a *source*, traverses the object of interest, and its strength on the opposite side is recorded as the number of photons which hit a *detector* (Figure 9.1). Given a series of such measurements, CT produces in the form of an image an estimate of the spatial distribution of the mass absorption coefficient function μ across a defined domain Ω. The domain can be chosen to cover the entire object or only a certain portion — referred to as global and local CT, respectively [108]. In this work we focus on the global variant.

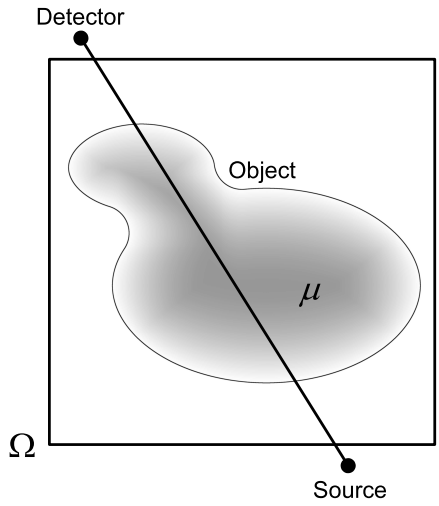

Figure 9.1: X-ray travelling from source to detector through the object of interest. The grayscale illustrates the mass absorption coefficient μ. The rectangle shows the image domain Ω.

9.2.1 Attenuation Model

In this article, we limit the CT problem to a plane intersecting the object of interest. Given an X-ray of intensity I along a line passing through the object,

the intensity attenuation dI which results when the ray travels along a segment $d\ell$ in a material with mass absorption $\mu \geq 0$, ignoring the effect of scattering and deflection of the ray from the material, can be described by the formula

$$dI = -I\mu d\ell. \tag{9.1}$$

An X-ray with initial intensity I_0, which has passed along the line segment L through the object, reaches the detector with the intensity I given by

$$I = I_0 \exp\left(-\int_L \mu(p) d\ell(p)\right), \tag{9.2}$$

where $\mu = \mu(p)$ and $p \in \Omega$ (see Figure 9.1). During the calibration phase of the scanner, I_0 is estimated by measuring the intensity of the ray at the detector when no object is present. The logarithmic transformation of the ratio of the intensities can be expressed as the integral of the mass absorption function

$$-\log\left(\frac{I}{I_0}\right) = -\int_{I_0}^{I} \frac{dI}{I} = \int_L \mu(p) d\ell(p). \tag{9.3}$$

Assuming this ray attenuation model, the tomographic image reconstruction problem can be recast as an integral geometry problem of estimating a function from values of line integrals through the domain of interest.

From the full continuous set of integral values and corresponding line orientations, also referred to as the complete Radon transform data [98], it is possible to compute analytically the unique mass absorption density. A very popular method for the solution of this problem is FBP, based on the theory of Radon and Fourier transforms of the integral data along with image filtering. The details of the method have been well described in the literature; see e.g. [9, 62, 64, 65].

In practice, the measurements will come from a finite number of source/detector pairs; sometimes, the application itself can further reduce the amount of projection data available. Modern medical CT scanners measure around 2 million rays, sufficient for reconstructing a single two-dimensional slice using FBP [65].

Because the analytical approach is known to suffer from serious shortcomings when the data is significantly incomplete, as is the case for the application considered here, as shown in [99], and illustrated in section 9.4, it is necessary to formulate the problem in terms of a discrete observation model and seek an approximate solution augmenting the data by complementary information. Before introducing the discrete model we present the type of X-ray projection data used in this work.

9.2.2 Projection Data

The applications targeted in this work are concerned with CT reconstruction from a series of *fan-beam* projections. Each projection consists of X-rays emitted from a point source, and the measurements of the corresponding attenuated fan-shaped beam of rays measured by an array of equally spaced detectors along an arc. A schematic picture of the fan beam data collection set-up is shown in Figure 9.2(a).

In conventional fan-beam scanners, the source and detector array are mounted on opposite sides of a gantry, which rotates to acquire the sequence of projections from different directions. Recent advance in the development of X-ray tubes have spawned stationary source acquisition techniques [120], where multiple sources and detectors are located at fixed positions around the object. An advantage of this method is that it does not require gantry motion, instead switching rapidly among the X-ray sources, each one creating a fan-projection of the object from a different angle. The lack of mechanical motion enables a more robust set-up, especially suitable for handling high throughput of industrial applications.

The increase in number of detectors does not change the radiation dose, so the main draw-back is a one-time installation expense. A reduction in the number of projections acquired by a stationary scanner, on the other hand, can both reduce the radiation exposure and the cost of the scan, without considering that each additional fan of X-rays is an expense during operation as well as wear on the X-ray tube. Here we focus on image reconstruction from projection data with *sparsity* with respect to the number of source positions. Figure 9.2(b) and (c) show schematic drawings of source positions for full data and the sparse data considered. In the following we assume that projection data from n_s X-ray source positions are acquired and we use one fixed fan-width, chosen such that all projections cover the object entirely. For each projection angle we measure n_d attenuated rays; the $n_d \times n_s$ matrix of projections data is referred to as a *sinogram* (Figure 9.3(b)).

The fan-beam projection model can be extended to three dimensions by acquiring series of projections, where the object is moved along the z-direction relative to the source, e.g. by a motorized table or conveyor belt. The movement can be performed in steps between acquiring several sinograms with geometrical set-up as described above, or continuously such that the relative source positions follow a helical trajectory around the object. In the present work we limit the presented reconstruction technique to two dimensional image slices.

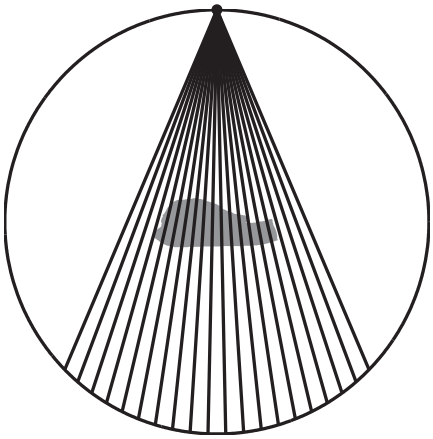

(a) Fan-beam.

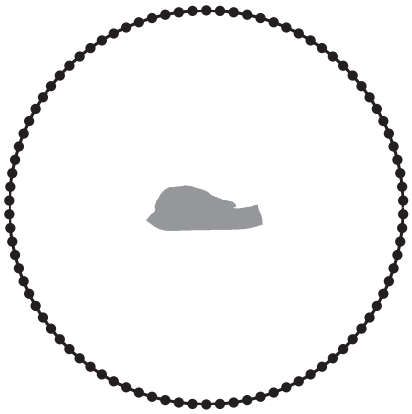

(b) Full data.

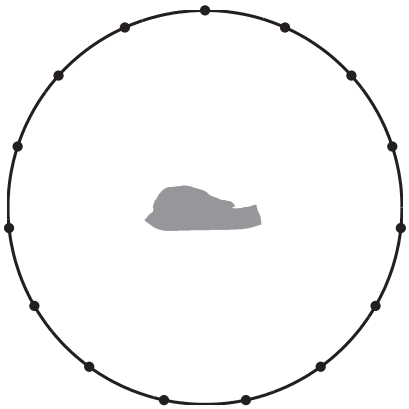

(c) Sparse data.

Figure 9.2: Geometric illustration of projection data. (a) A single fan-beam projection; The lines illustrate rays emitted from a point source, hitting an arc-shaped array of 20 equally spaced detectors after passing through the object. (b) and (c) Source position set-ups for acquisition of full data and sparse data, respectively.

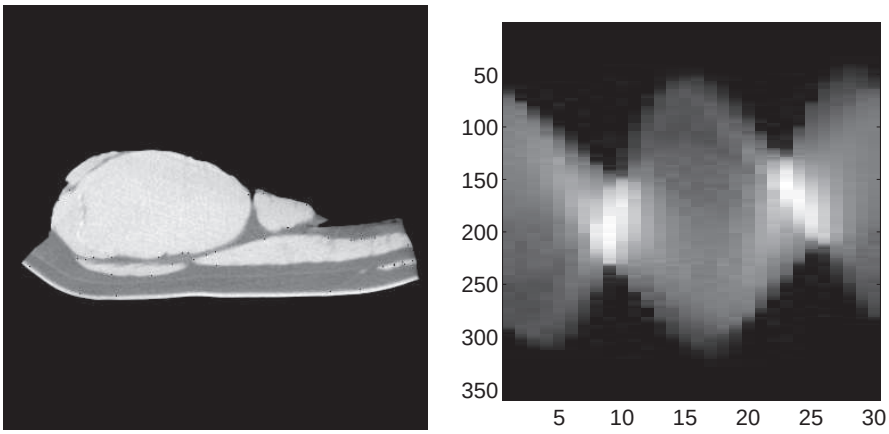

(a) Pig back. (b) Sinogram.

Figure 9.3: CT image data. (a) Pig back, as used for the application in section 9.4.2. (b) Corresponding simulated fan-beam sinogram (fan opening angle 45°, measuring $n_d = 360$ rays in each of the $n_s = 30$ source positions).

9.2.3 Discrete Model

To recast the problem in a discrete setting, we discretize the planar domain Ω using an $m \times n$ regular grid of image pixels $P_{i,j}$, as illustrated in Figure 9.4, and we assume that the mass absorption coefficient μ remains constant in each pixel

$$\mu(p) = \mu_{i,j},\ p \in P_{i,j},\ 1 \le i \le m,\ 1 \le j \le n. \tag{9.4}$$

For computational convenience, we will switch back and forth between a matrix and a vector representation of the $\mu_{i,j}$'s, where the vector $x \in \mathbb{R}^N$, with $N = n{\cdot}m$, contains the matrix entries in column-wise ordering. Whenever convenient, we will collect the sinogram entries into a vector $b \in \mathbb{R}^K$, $(K = n_s{\cdot}n_d)$, following the same convention.

The kth column b_k of the sinogram matrix holds the measurements of the attenuated kth X-ray fan beam. In the expression of the integral along the line L_k through Ω from the kth source to one of the detectors, if $|L_k \cap P_{i,j}|$ denotes the length of the intersection of L_k and the pixel $P_{i,j}$, we can express the domain of integration as a finite sum of contributions from individual pixels, arriving at

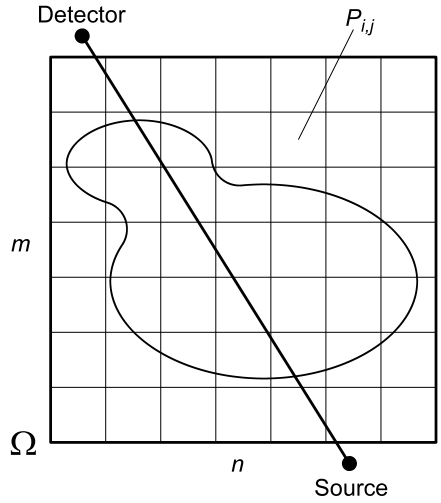

Figure 9.4: The spatial domain Ω is partitioned into $m \times n$ pixels, and the attenuation coefficient μ is discretized as a piecewise constant function in each pixel.

the discrete formulation

$$b_k = \int_{L_k} \mu(p)dp = \sum_{i=1}^{n}\sum_{j=1}^{m} |L_k \cap P_{i,j}|\, \mu_{i,j} = \sum_{s=1}^{N} A_{k,s}x_s. \tag{9.5}$$

Organizing the lengths of the intersections between the K source to detector lines and the N pixels into the matrix $A \in \mathbb{R}^{K\times N}$, we can write the discrete problem in the form

$$b = Ax, \tag{9.6}$$

which is known as the *discrete Radon transform* of the vector x. Therefore the CT image reconstruction problem can be regarded as the inverse problem of estimating N unknowns given a system of K linear equations. Due to the way it is formed, the system matrix A is typically very large and extremely sparse, because each ray intersects a very small fraction of the pixels.

Iterative methods, for which a factorization of the system matrix is not needed, are the natural choice for solving large sparse systems of equations. In the context of image reconstruction, the algebraic reconstruction technique (ART), introduced by Gordon et al. in 1970 [44] has enjoyed vast popularity. The method is a version of the classical Kaczmarz method of projections for solving a linear system of equations [61], which iteratively updates the approximate

solution by projecting it onto a sequence of hyperplanes corresponding to sums of ray. For the details we refer to, e.g., [100].

The disproportionately large ratio of unknowns to measurements or, equivalently, the large null space of the matrix A, is a problem for the computation of a stable and meaningful solution, worsened by the ill-conditioning of the problem and by the errors in the model and measurement. To overcome the ill-posedness and to take advantage judiciously of the null space of A, it is necessary to introduce complementary information about the problem and the expected solution, a technique commonly referred to as regularization in the inverse problems community. In the next section we modify our discrete formulation of the problem to account for errors and we introduce the Bayesian approach that we propose for the solution of the CT inverse problem from few projections.

9.3 A Bayesian Framework for the CT Inverse Problem

In the context of Bayesian inverse problems, all unknown parameters are regarded as random variables, where the randomness is not intended as an intrinsic property of the unknowns, but rather a reflection of our uncertainty about their values. Within this paradigm, both the measured X-ray projections, which are affected by uncertainties due to both measurement errors and model limitations, and the reconstructed image are regarded as random variables. In the sequel we will denote random variables by letters in uppercase and their corresponding realizations in lowercase. Probability density functions are generally denoted by π, with a subscript when appropriate.

In general, the Bayesian solution of an inverse problem amounts to infer on the unknown of primary interest, X, from measurement of another variable, B, assuming a model linking the two and in the light of what are the believed properties of X [17]. Since in this context both X and B are random variables, the natural way to describe them is via probability density functions.

The *likelihood* is the probability density function of B assuming that $X = x$ is known, denoted as $\pi_{\text{likelihood}}(b \mid x)$. The shape of the likelihood is strongly affected by the characteristics of the noise, as will be explained below. The *prior* probability density function, $\pi_{\text{prior}}(x)$, expresses in probabilistic terms what are the perceived characteristics of X prior to taking the data into consideration. In our particular application, where the matrix A has a large null space, the prior provides additional information which can be used to mine the null space of A for meaningful contributions. The *posterior*, $\pi_{\text{posterior}}(x)$, is the probability density

function of X conditioned on the current realization of the data, $\pi_{\text{posterior}}(x) = \pi(x \mid b)$, and can be interpreted as the correction of the prior in the light of the likelihood. It follows from basic probability rules and Bayes' formula that

$$\pi(x \mid b)\pi(b) = \pi_{\text{likelihood}}(b \mid x)\ \pi_{\text{prior}}(x). \tag{9.7}$$

Since the marginal density $\pi(b)$ of B is independent of x, and it only contributes to scaling the posterior, it is often neglected, and the relation between prior, likelihood and posterior is expressed in the form.

$$\pi(x \mid b) \propto \pi_{\text{likelihood}}(b \mid x)\ \pi_{\text{prior}}(x). \tag{9.8}$$

The posterior density is the Bayesian solution of the inverse problem. Once the posterior has been determined, there are a few options available. The realization of X which has the highest probability in the sense that it maximizes the posterior distribution function, the MAP estimate, is a very popular choice and often the computationally least costly. A drawback of summarizing a distribution with a single point estimator is that the latter does not convey any information about the spread of the density, which in turn provides us with a mean to assess how much variability it should be expected in the solutions. If uncertainty quantification is important in the application at hand, a large sample generated by drawing realizations from the posterior density can be used to study the variability that the posterior distribution allows.

We now reformulate the discrete tomographic reconstruction model in the Bayesian framework, encode our qualitative a priori belief about the structure of the scanned object, and write the likelihood model for the CT fan beam problem. We also propose a fast and robust computational method to estimate the MAP attenuation image, and illustrate how the posterior can be used for uncertainty quantification of the solution in some regions of particular interest.

In actual applications, the CT projection model (9.6) should account for errors in the measured data and model limitations, the aggregate of which will be referred to as noise. Assuming that the noise is additive and independent of the image that we want to estimate, we have the noisy discrete model

$$b = Ax + e. \tag{9.9}$$

Recasting the problem in probabilistic terms, where $E \in \mathbb{R}^K$ and $X \in \mathbb{R}^N$ and random variables, we have the stochastic extension of (9.9)

$$B = AX + E. \tag{9.10}$$

In CT the data consist of photon counts, hence the data can naturally be regarded as Poisson distributed. However, unless low dose measurements are used,

the photon count is high, it is reasonable, and computationally advantageous, to resort to a Gaussian approximation; see: appendix of [108]. Therefore, assuming that the noise in each data entry is independent, zero-mean Gaussian noise model with variance σ^2, $E \sim \mathcal{N}(0, \sigma^2 I)$, the likelihood of the observed data can be written as

$$\pi_{\text{likelihood}}(b \mid x) \propto \pi_{\text{noise}}(b - Ax) \propto \exp\left(-\frac{1}{2\sigma^2}\|b - Ax\|^2\right). \tag{9.11}$$

Observe that to approximate Poisson distribution by a Gaussian, it would be natural to assume that the mean and variance coincide, and sometimes, a smoothed version of the data is used as a variance estimator. A white noise approximation adopted here can be justified when the attenuation does not vary dramatically in the sinogram data.

In the CT application that we are targeting here, it is known that the scanned object consists of well-separated regions with different X-ray attenuation coefficients, so it is reasonable to expect that the reconstructed image has clearly distinct areas of homogeneous intensities, with sharp transitions in between. Therefore a good prior, accounting for the structure of the object, should favor little change in intensity within same tissue regions, and allow sharp changes of intensity at the boundaries between different tissues. In mathematical terms this means that we expect the spatial derivatives to be small inside a uniform region, and very high at the transition between one region and the other. Following [18], let L_1 and L_2 be the finite difference matrices for the horizontal and vertical first order partial derivatives with zero boundary conditions. We express the expected small horizontal and vertical partial derivatives of X by writing

$$L_* X \sim \mathcal{N}(0, D_\theta), \tag{9.12}$$

$$\pi(L_* x) \propto \exp\left(-\frac{1}{2} x^T \left(L_*^T D_\theta^{-1} L_*\right) x\right), \tag{9.13}$$

with L_* denoting either L_1 or L_2. This smoothness condition is equivalent to modeling the partial derivatives as zero-mean multivariate Gaussian variables with covariance matrices $D_\theta = \text{diag}(\theta_1, \ldots, \theta_N)$, where $\theta_j > 0,\ j = 1, \ldots, N$. The vector θ conveys the expected variability of the intensity derivatives at the different pixels. Since the values θ_j act as weights in (9.13), they affect the location of the edges in the reconstructed image. Setting the variance equal at all pixels $\theta_j = \theta_0$ is tantamount to expecting the image to be equally smooth everywhere, while a larger than average value θ_j, would convey the expectation that the first order derivatives at pixel x_j may take on a large value. If the location and magnitude of edges were known ahead of time, they could be used to set the values of the θ_js. In general, however, the information available prior to the reconstruction is qualitative, in the sense that sharp edges are expected

between different tissue types in an otherwise smooth image, with no information about position, magnitude or number.

In agreement with the statistical framework, since θ is a vector of unknown parameters, we consider it as a realization of a random variable Θ which should be added to the list of variables, that we want to estimate. The joint prior density of X and Θ is

$$\pi(x,\theta)_{\text{prior}} = \pi_{\text{prior}}(x \mid \theta)\pi_{\text{hyper}}(\theta). \tag{9.14}$$

Because the uncertainty carried into the problem by Θ affects the unknown at another layer, we refer to it as a hyperparameter vector and refer to its probability density function $\pi_{\text{hyper}}(\theta)$ as a *hyperprior*. The role of Θ in this hierarchical formulation of the CT inverse problems is very important, as we will see later.

Let's assume for the moment that $\Theta = \theta$ is fixed, and that the values of the horizontal and vertical partial derivatives are independent. Then

$$\pi_{\text{prior}}(x \mid \theta) = \pi(L_1 x,\ L_2 x \mid \theta) = \pi(L_1 x \mid \theta)\pi(L_2 x \mid \theta). \tag{9.15}$$

Relaxing the condition on the hyperparameter θ and adding it to the list of the unknowns, implies that the normalizing factor of (9.13) which depends on θ must be explicitly accounted for, hence

$$\pi(L_* x \mid \theta) = \frac{|L_*|}{(2\pi)^{N/2}|D_\theta|^{1/2}} \exp\left(-\frac{1}{2}x^T \left(L_*^T D_\theta^{-1} L_*\right) x\right), \tag{9.16}$$

from which we arrive at the following conditionally Gaussian prior formulation

$$\begin{aligned} \pi_{\text{prior}}(x \mid \theta) &= \frac{|L_1||L_2|}{(2\pi)^N |D_\theta|} \exp\left(-\frac{1}{2}x^T C_\theta x\right) \\ &\propto \left(\prod_{j=1}^{N} \theta_j^{-1}\right) \exp\left(-\frac{1}{2}x^T C_\theta x\right), \end{aligned} \tag{9.17}$$

where $C_\theta = L_1^T D_\theta^{-1} L_1 + L_2^T D_\theta^{-1} L_2$.

The last step that needs to be addressed in the design of the CT-prior is how to choose a hyperprior. Since the edges are expected to be distinct and the variation of the intensity across an edge sudden, while we have no information about their presumed location, the θ_j's should be mutually independent and identically distributed. Moreover, since the image is expected to consist of large homogeneous regions, only at few pixels we may expect the values of the derivatives to be large. Therefore the hyperprior should be a distribution which favors small values, but allow a few outliers.

The gamma distribution [7]

$$\Theta_j \sim \text{Gamma}(\alpha, \theta_0), \tag{9.18}$$

with the density

$$\pi_{\text{hyper}}(\theta) \propto \prod_{j=1}^{N} \theta_j^{\alpha-1} \exp\left(-\frac{\theta_j}{\theta_0}\right), \tag{9.19}$$

which is shown in Figure 9.5, seems to qualitatively correspond to this description. The mode of the density near zero corresponds to the understanding that the image is mostly made of smooth regions, and the right tail allows intensity jumps if needed.

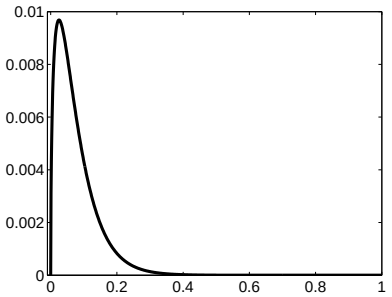

Figure 9.5: Example of density function for the gamma distribution.

With this choice of hyperprior, the joint prior for X and Θ is

$$\pi_{\text{prior}}(x, \theta) \propto \left(\prod_{j=1}^{N} \theta_j^{-1}\right) \exp\left(-\frac{1}{2} x^T C_\theta x\right) \left(\prod_{j=1}^{N} \theta_j^{\alpha-1} \exp\left(-\frac{\theta_j}{\theta_0}\right)\right). \tag{9.20}$$

The introduction of an additional layer does not change the form of the likelihood, but the posterior needs to be adjusted as follows

$$\pi_{\text{post}}(x, \theta \mid b) \propto \exp\left(-\frac{1}{2\sigma^2}\|b - Ax\|^2 - \frac{1}{2} x^T C_\theta x + (\alpha - 2)\sum_{j=1}^{N} \log \theta_j - \sum_{j=1}^{N} \frac{\theta_j}{\theta_0}\right), \tag{9.21}$$

where $C_\theta = L_1^T D_\theta^{-1} L_1 + L_2^T D_\theta^{-1} L_2$.

9.3.1 A Representative Realization from the Posterior: the MAP Estimate

If we want to produce a single image from the posterior distribution, one possible choice is to compute the realization maximizing the posterior probability density. The MAP estimate of (x, θ) is the minimizer of the negative logarithm of the density, which in the present case is given by

$$\begin{aligned} F(x,\theta) &= -\log(\pi_{\text{post}}(x,\theta \mid b)) \\ &= \frac{1}{2\sigma^2}\|b - Ax\|^2 + \frac{1}{2}x^T C_\theta x - (\alpha - 2)\sum_{j=1}^{N}\log\theta_j + \sum_{j=1}^{N}\frac{\theta_j}{\theta_0}. \end{aligned} \tag{9.22}$$

In [7, 18], an efficient alternating algorithm for finding the minimizer of objective functions with a similar structure has been proposed. The algorithm sequentially updates one of the two unknowns x and θ, while keeping the other fixed:

1. Initialize $k = 1$ and $\theta^0 = \text{diag}(\theta_0)$.
2. Update $x^k = \text{argmax}\{\pi_{\text{post}}(x, \theta^{k-1} \mid b)\}$.
3. Update $\theta^k = \text{argmax}\{\pi_{\text{post}}(x^k, \theta \mid b)\}$.
4. Update $k = k + 1$ and return to step 2.
   Repeat until convergence.

When $\theta = \theta^k$ is fixed in step 2, $F(x, \theta)$ becomes a quadratic function of x, whose minimizer is the least squares solution of the linear system

$$Mx = r, \quad M = \begin{bmatrix} \sigma^{-1}A \\ D_\theta^{-1/2}L_1 \\ D_\theta^{-1/2}L_2 \end{bmatrix}, \quad r = \begin{bmatrix} \sigma^{-1}b \\ 0 \\ 0 \end{bmatrix}. \tag{9.23}$$

which can be computed by the conjugate gradient method for least squares (CGLS) iterative method [11, 52]. When $k = 1$, the update of x corresponds to applying the first order smoothness penalty with equal weight on all pixels.

In step 3, when $x = x^k$ is fixed, the first term in (9.22) is independent of θ. Since we have assumed that the θ_j's are independent from each other, the update of θ can be done element wise by solving $\frac{\partial F}{\partial \theta_j} = 0$ for $j = 1, \ldots, N$, which leads to

$$-\frac{1}{2}\frac{[L_1x]_j^2 + [L_2x]_j^2}{\theta_j^2} + \frac{1}{\theta_0} + (\alpha - 2)\frac{1}{\theta_j} = 0, \tag{9.24}$$

where $[L_* x]_j^2$ denotes the square of the derivative at pixel j in the pertinent direction. The solution of this second order polynomial equation can be computed analytically, therefore we have a closed-form expression for the update of the entries of θ,

$$\theta_j = \theta_0 \left(\eta + \sqrt{\frac{[L_1 x]_j^2 + [L_2 x]_j^2}{2\theta_0} + \eta^2} \right), \tag{9.25}$$

with $\eta = \frac{1}{2}(\alpha - 2)$.

Figure 9.6 shows the images of the vector x and the corresponding hyperparameter θ in the first four steps of the iterative procedure to compute the MAP estimate for a CT-reconstruction from a simulated sinogram of 30 fan-beam projections each with 360 rays covering an opening angle of 45°. The first iterate of the image ($k = 1$) is a smoothed out approximation of the true target, which is not surprising, since it corresponds to a Tikhonov regularized estimate with a homogenous first order smoothness penalty. When $k = 2$, the edges between different tissue types start to be already rather sharp, while the estimate maintains the smooth characteristics inside homogeneous regions. The improvement from $k = 3$ to $k = 4$ is rather minimal, therefore suggesting that the algorithm reaches convergence in few iterations.

9.3.2 Uncertainty Quantification

The MAP estimator, although a useful summary of the Bayesian solution to the inverse problem, gives no indication of the uncertainties of the estimate, and to quantify the uncertainties, one typically needs to resort to Markov chain Monte Carlo (MCMC) sampling methods. In the present hierarchical formulation of the problem, sampling must comprise both variables X and Θ. MCMC sampling in imaging applications is challenging because of the high dimensionality of the problem. As we are estimating both the reconstructed images and hyperparameter, the curse of dimensionality is even more aggravated. However, one is often only interested in evaluating the uncertainty within a given spatial region of interest (ROI) defined on the image, e.g. containing certain features of interest [18].

In the example shown in section 9.4.2.1 the ROI comprises an area around the interface detected by the MAP estimate between meat and fat. In the present industrial application, the location of this transition is of particular importance, as the image is used to guide a cutting robot trimming the rind to a given thickness.

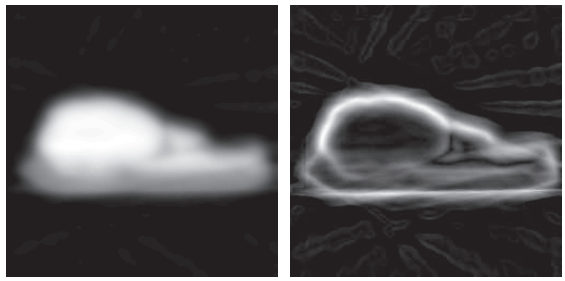

(a) $k = 1$.

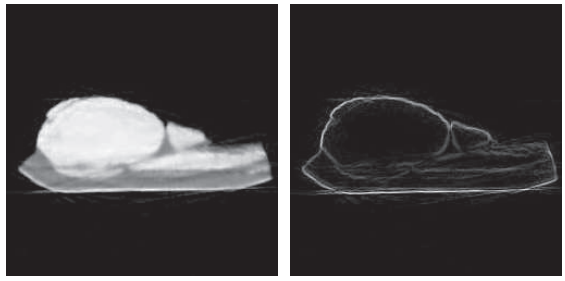

(b) $k = 2$.

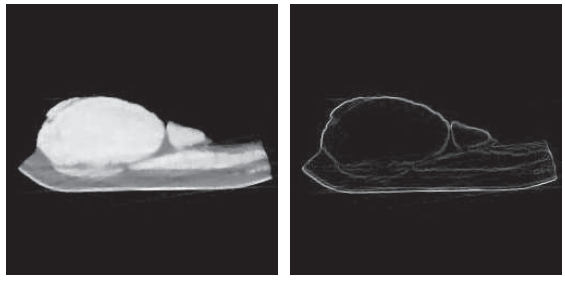

(c) $k = 3$.

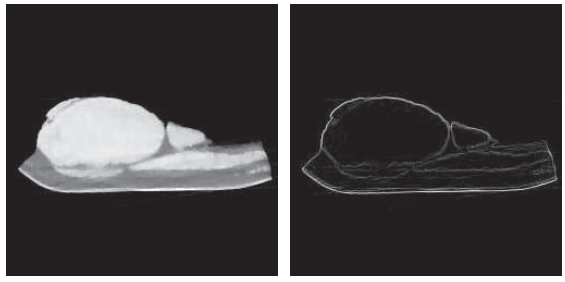

(d) $k = 4$.

Figure 9.6: Intermediate estimates for image x and hyperprior θ of the first four consecutive iterations of the two-step reconstruction. The reconstruction is based on the simulated sinogram in Figure 9.3(b).

To organize effectively the sampling over the ROI, let $I = \{1, 2, \ldots, N\}$ denote the index set of the pixels in the whole image, and the ROI be defined as the k pixels with indices $I_{\text{ROI}} = \{i_1, i_2 \ldots, i_k\} \subset I$. The image $X \in \mathbb{R}^N$, after permuting the indices, is partitioned in two $X = [X'; X'']$, such that $X' = [X_{i_1}; X_{i_2}; \ldots; X_{i_k}] \in \mathbb{R}^k$ contains the pixels of the ROI, and $X'' \in \mathbb{R}^{N-k}$ contains the pixels in the complement. The hyperparameter is partitioned in the same way $\Theta = [\Theta'; \Theta'']$.

With this partitioning and the MAP estimator $(x_{\text{MAP}}, \theta_{\text{MAP}}) = ([x'_{\text{MAP}}; x''_{\text{MAP}}], [\theta'_{\text{MAP}}; \theta''_{\text{MAP}}])$, we can write the posterior density of the variables in the ROI conditioned on the complement as well as the observations b as

$$\pi(x', \theta' \mid b, x''_{\text{MAP}}, \theta''_{\text{MAP}}) \propto \pi(x, \theta \mid b)\big|_{x''=x''_{\text{MAP}}, \theta''=\theta''_{\text{MAP}}}. \tag{9.26}$$

The MCMC sampling over the ROI can be done with a block form of the Gibbs sampler [74]. As with the iterative MAP estimation, we adopt the two-step approach for the Gibbs sampler, fixing alternately one of the parameters x' and θ', while updating the other by drawing from the conditional density. More precisely, the algorithm is described as follows:

1. Initialize $k = 0$, $x^0 = x_{\text{MAP}}$ and $\theta^0 = \theta_{\text{MAP}}$.
2. Draw x' from the conditional distribution $\pi(x' \mid b, \theta^k, x''_{\text{MAP}})$.
   Update $x^{k+1} = [x'; x''_{\text{MAP}}]$.
3. Draw θ' from the conditional distribution $\pi(\theta' \mid b, x^k, \theta''_{\text{MAP}})$.
   Update $\theta^{k+1} = [\theta'; \theta''_{\text{MAP}}]$.
4. Update $k = k + 1$.
   Repeat from step 2 until the desired sample size is reached.

For updating x in step 2, let M and r be the arrays defined in (9.23), with $\theta = \theta^k$, and let $M = [M', M'']$ be the column partitioning of M corresponding to the ROI and its complement. The factor in the posterior distribution conditioned on $\theta = \theta^k$ depending on x is

$$\pi(x' \mid b, \theta^k, x''_{\text{MAP}}) \propto \exp\left(-\frac{1}{2}\|M'x' + M''x''_{\text{MAP}} - b\|^2\right), \tag{9.27}$$

suggesting that a random draw for x' can be accomplished by solving in the least squares sense the problem

$$M'x' = b - M''x''_{\text{MAP}} + \xi, \quad \xi \sim \mathcal{N}_k(0, I). \tag{9.28}$$

The latter problem is solved using the CGLS algorithm.

For the random draw of the hyperparameters θ in the ROI, we exploit the mutual independency of the components θ_i in the posterior distribution. The posterior distribution of θ_j is

$$\pi(\theta_j) \propto \exp\left(-\frac{1}{2}\frac{[L_1 x]_j^2 + [L_2 x]_j^2}{\theta_j^2} + (\alpha - 2)\log\theta_j - \frac{\theta_j}{\theta_0}\right),\ j \in I_{\text{ROI}}, \quad (9.29)$$

and the component-wise draws are performed with the inverse probability density algorithm (see [17]). In practice, to avoid numerical instabilities, we restrict the probability distribution function for $\theta_{\min} < \theta_j < \theta_{\max}$, such that the value of π is negligible outside the interval. To find reasonable bounds, observe that a small value of θ_j will cause the first term of (9.29) to dominate, whereas the last term dominates for a large value of θ_j. We therefore define the limits

$$\theta_{\min} = \frac{[L_1 x]_j^2 + [L_2 x]_j^2}{2\log(1/d)} \text{ and } \theta_{\max} = \theta_0 \log(1/d), \quad (9.30)$$

for a small threshold value d. Observe that $\theta_{\min}$ is pixel specific while $\theta_{\max}$ is the same across the ROI.

For each pixel, we divide the interval into m equally sized sub-intervals with division points $t_0 < t_1 < \cdots < t_m$, with $t_0 = \theta_{\min}$ and $t_m = \theta_{\max}$, and define the non-normalized cumulative distribution function and its corresponding discrete approximation,

$$\Phi_j = \int_{t_0}^{t_j} P(t)dt \approx \sum_{i=0}^{j} P(t_i). \quad (9.31)$$

The sampling of a single θ_j comprises of drawing t from a uniform distribution $U(0, \Phi_m)$, and going *backwards* to find the corresponding bin index as $i = \min\{k \mid 1 \le k \le m, \Phi_k > t\}$, the generated random sample of the hyperprior being $\theta_j = t_i$.

The uncertainty over the ROI needs to be interpreted and visualized from the variability of the sample thus generated. Finding a suggestive way of visualizing the variability may be a challenging task.

9.4 Computed Examples

In this section we illustrate the performance of the BASE-CT reconstruction method with three computed examples. In the first example, which utilizes

phantom data, we compare the reconstruction obtained with BASE-CT with those produced by other popular methods: FBP, ART and TV regularization. The second and third examples address the applicability of BASE-CT for industrial imaging in a modern pig slaughterhouse. All computations were performed using MATLAB [76] on a personal computer equipped with a 64-bit 2.5 GHz dual-core processor and 4.0 GB of RAM. In all three computed examples, to avoid committing the most obvious *inverse crime* [62], we use different A-matrices to generate the sinogram and to estimate the MAP image, which is equivalent to changing pixel size. More precisely, we use 1mm^2 pixels for the reconstruction while in the data generation, the pixel size is $512/800 = 0.64\text{mm}^2$ and $300/391 = 0.77\text{mm}^2$ for the phantom and industrial applications, respectively.

9.4.1 A Proof of Concept Example Using Phantom Data

In the first benchmark example, we use a 800×800 Shepp-Logan phantom [106] with image intensities between 0 and 1 to generate a noiseless sinogram with a sparse set of 40 fan beam projections each consisting of 180 attenuated rays. Figure 9.7 shows the phantom and simulated sinogram. The 512×512 pixel image reconstructed using the BASE-CT methods is presented in Figure 9.8(d). For comparison, in Figure 9.8(a-c) we show three reconstructions, corresponding to the FBP, ART and TV methods, respectively, implemented following [76, 100, 107], respectively.

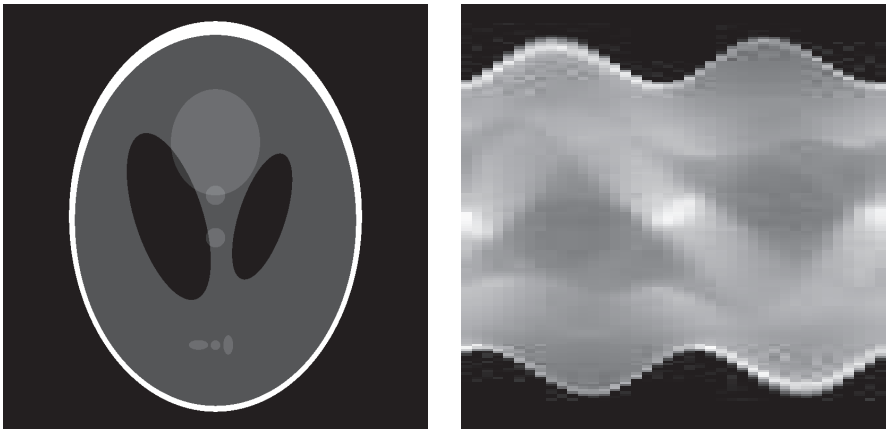

(a) Shepp-Logan phantom.

(b) Simulated sinogram ($n_s = 40$, $n_d = 180$).

Figure 9.7: Phantom data.

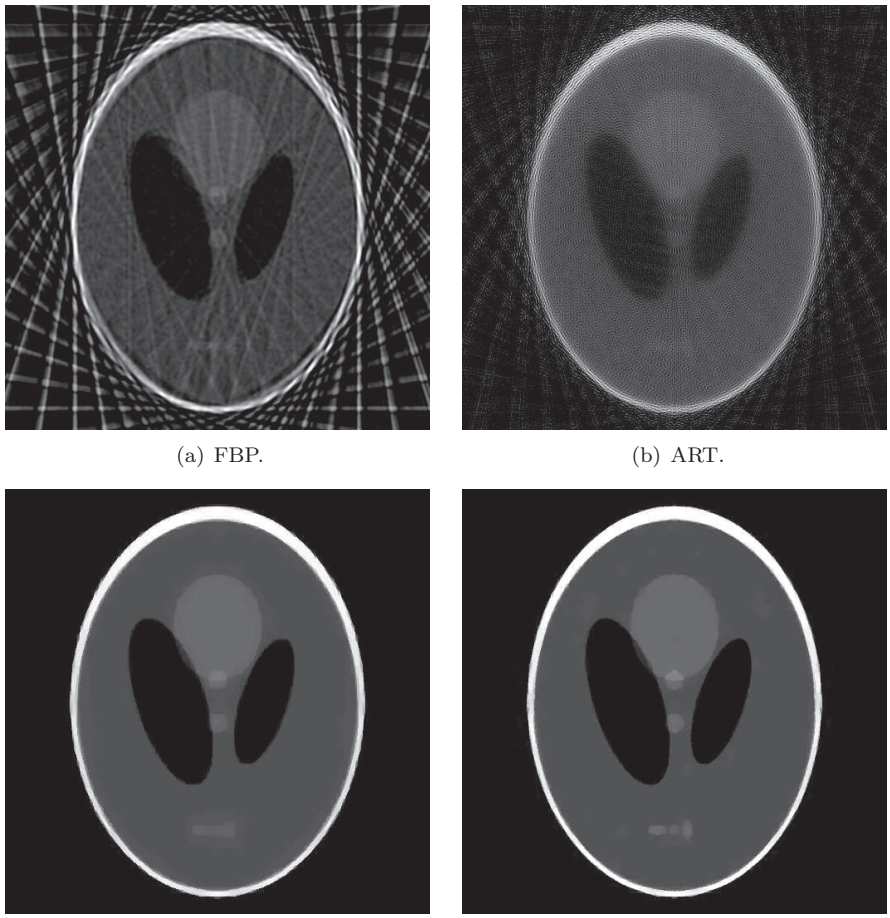

(a) FBP. (b) ART.

(c) TV. (d) BASE-CT.

Figure 9.8: Phantom data reconstructions.

As expected, the MAP-estimate of the hyperparameter θ, shown in Figure 9.9, attains values of large magnitude at the boundaries between regions with different attenuation properties.

Figure 9.9: BASE-CT hyperprior.

The reconstructions obtained with both TV and BASE-CT are significantly better than those obtained with FBP and ART that produce the characteristic streak artifacts (FBP) or a fuzzy background (ART). Upon closer examination, it is clear that the TV regularization favors a higher degree of blocky structures than BASE-CT, a feature that becomes evident in a horizontal cross-section profile through the lower part of the phantom (Figure 9.10). The phantom contains three small separate inclusions, and the method based on TV reconstructs tends to lump them together into a single inclusion with higher intensity, while BASE-CT is able to form three separate regions.

9.4.2 A Pig Slaughterhouse Application

Competition in the meat industry has moved the processing from small local facilities into large centralized slaughterhouses. This development has stressed to the limit traditional manual slaughtering techniques, which would lead to physically demanding and repetitive procedures in the new labor-intensive working environment.

Consequently, the industry has become increasingly more interested in developing tools for process automation, in hope that more efficient automated processing leads to safer and faster production, better hygiene, an improved utilization

(a) Profile position.

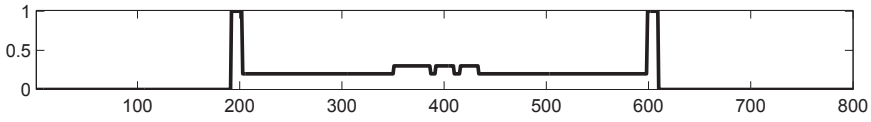

(b) Original intensities.

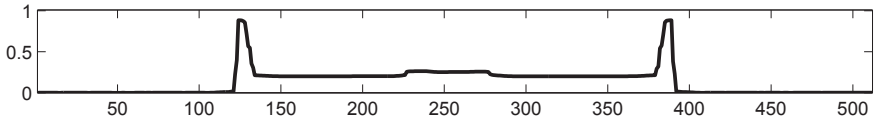

(c) TV.

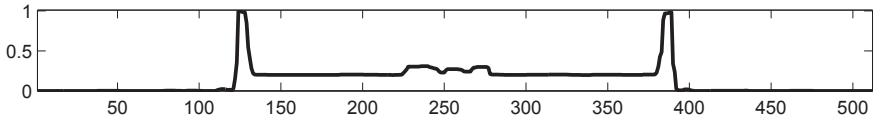

(d) BASE-CT.

Figure 9.10: A closer look at a horizontal profile through the phantom.

of the carcasses, and a more uniform quality of the end products.

In pig meat production, existing automation tools include measuring systems for carcass classification and sorting, as well as robotics for carcass cutting, evisceration, boning and trimming various parts. An important key in the automated processing is individual adaption by means of subject specific information; to create homogeneous products from inhomogeneous raw materials. Current techniques are based on image analysis coupled with imaging hardware including ultrasonic sensors and computer vision systems [16, 97, 118].

CT is already widespread in medical and industrial applications, providing high contrast 3D images of internal structures. In the context of automated meat processing, these images give detailed characteristics of the raw materials, e.g. for determining accurate cut-paths for robotics. CT has also proven highly suitable for robust estimation of the lean meat percentage (LMP) in pig carcasses [115] — a quantity useful for grading and sorting the raw materials for optimal utilization.

9.4.2.1 Fat-layer Thickness

The first industrial application that we consider is aimed at an automatic cutting tool for pig backs to produce bacon with a given fat-layer thickness, for which it is necessary to identify the transition between fat and meat tissue in the CT image to guide the automated cutting.

The corresponding manual procedure is physically demanding and repetitive; the layer is repeatedly trimmed and measured until the wanted thickness is achieved.

Furthermore, the yield can be improved by accurately automating the cutting; if too much fat is cut off, the slaughterhouse loses profit as the product is sold by weight and an established target percentage of fat and meat, and meat is more valuable than fat. On the other hand, trimming too little fat will result in dissatisfied customers and possible losses in future sales. Furthermore, trimming the fat-layer in one piece, results in less waste as it makes the fat valuable as a separate by-product.

In the following example we study the accuracy of the fat-layer measurements to assess the suitability of the BASE-CT reconstruction method for the cutting-application. Using the uncertainty quantification approach described in section 9.3.2, we draw from the posterior a sample of 10000 realizations of a ROI containing the transition between rind and meat.

The selected ROI does not include the skin, as it is reasonable to assume that its location does not change, since the pig back would be placed skin-side down on a conveyer belt for the scanning in the slaughterhouse. For each sample image, the fat thickness is measured along a fixed set of profiles, mimicking what would be preformed manually. For each profile, the position of the boundary between lean and fat is measured along the line segment, thus reducing the dimensionality of the problem regarded to one. Figure 9.11 shows the MAP reconstructed image with ROI-borders and the profiles and the MAP-image with edge-position histograms superimposed.

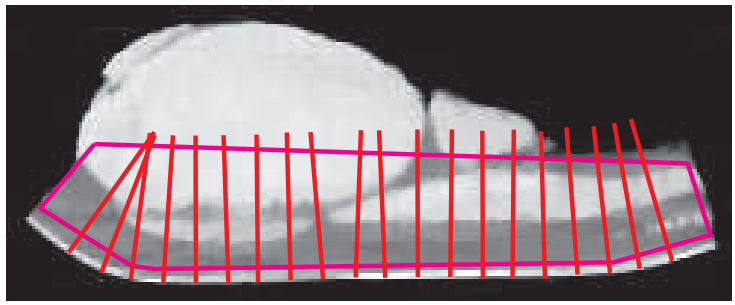

(a) BASE-CT MAP-estimate image with lines and polygon illustrating the 20 measurement profiles and the ROI, respectively.

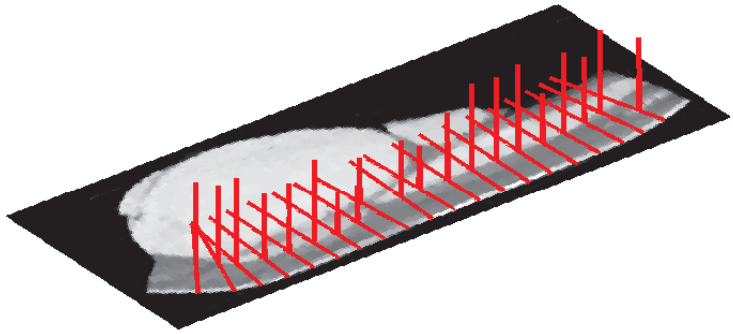

(b) Histograms of edge positions located on the 10000 samples.

Figure 9.11: Accuracy of fat-layer thickness by random sampling.

The position of the transition between lean and fat is quite stable over the sample, and the corresponding histograms are very narrow, suggesting that the MAP-estimate is a very good representative of the entire distribution. Figure 9.12 shows the envelops centered at the sample mean and extending three standard deviations on each side for the 3rd and 7th profiles from the left in Figure 9.11. By looking at the corresponding histograms, also shown in the picture,

it is clear that the 3rd profile is much more narrowly determined than the 7th. This may be due to the fact that the 3rd profile is closer to the left edge of the pig back, where some of the X-rays used to reconstruct this area pass through fewer attenuating pixels.

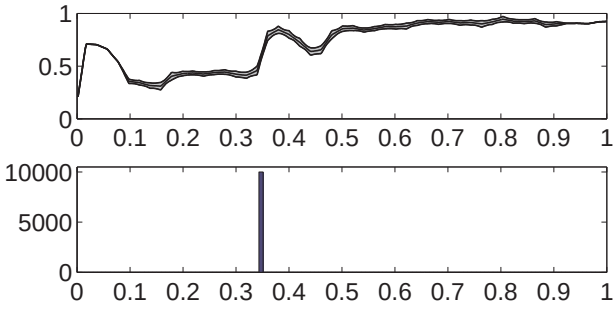

(a) 3rd profile.

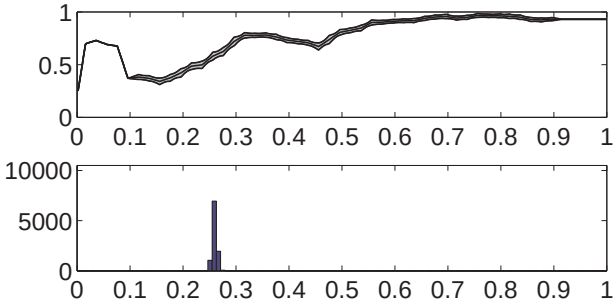

(b) 7th profile.

Figure 9.12: Top; mean ± three standard deviations of intensities in profiles from the 10000 samples. Bottom; histogram of measured edge-positions. The x-axes refer to relative position on the profile ($x = 0$ is at the skin).

9.4.2.2 Lean Meat Percentage

In our second industrial application example, we use CT images to measure the LMP of the carcass, an indicator used for grading and sorting it for further processing.

Measuring the LMP can currently be automated using ultrasound or optical sensors which are calibrated towards a common manual standard dissection method of half pig carcasses [16]. However, the accuracy and precision of these calibra-

tions are limited by that of the dissection method, and studies have reported significant differences between butchers performing the dissections [84].

Extending the concept of tissue-classification by CT, from a reference in calibration of existing tools [115] to online CT and accurate LMP-measurements of every single carcass, could therefore further improve the processing.

To study the suitability of BASE-CT in this context, we perform tissue classification by intensity thresholding. Figure 9.13 shows tissue labels on the original and our reconstructed image, we achieve a good correspondence between the two sets of labels, with LMPs of 56.32% and 56.15%. The thin line of white-labelled

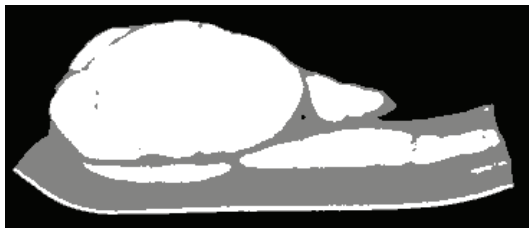

(a) Original.

(b) BASE-CT.

Figure 9.13: Tissue labels. White; meat, grey; fat.

pixels seen in the bottom corresponds to the skin-layer, by convention, this is considered part of the fat-tissue class, accounted for in the LMP-calculations. The reason why the layer is barely visible on the labels corresponding to BASE-CT is that since for the sampling the reconstructing is computed at a lower resolution (300×300 pixels versus the 391×391 pixels of the original image) to reduce the computations, the skin layer is often less than a pixel wide, hence invisible in our classifications.

To evaluate the reliability of our measurements we generate a sample of 3000 images of the entire pig back from the posterior; the sample man LMP is 56.00% and the sample standard deviation 0.17%.

In Figure 9.14 we plot of the calculated LMPs corresponding to the 3000 draws which show that the values across the sample are very tightly clustered around the sample mean, suggesting that the MAP-estimate image is very reliable.

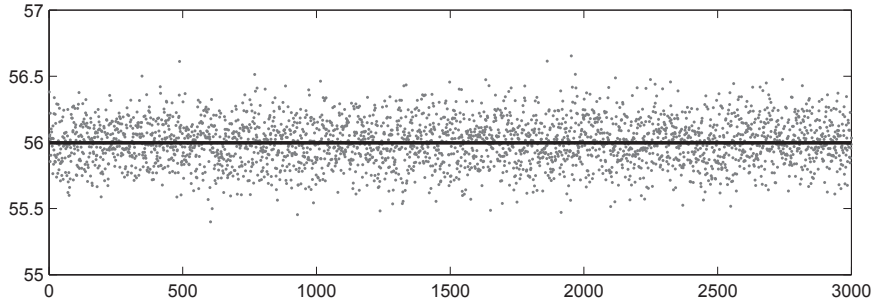

Figure 9.14: LMP values corresponding to a sequence of 3000 random draws from the posterior distribution. Horizontal line corresponds to the sample mean 56.00%.

9.5 Conclusion

In this work we present BASE-CT: A method for CT X-ray image reconstruction from few projections. The algorithm follows the Bayesian approach to statistical inversion, formulating the inverse problem using probability density functions. This way, the solution is the posterior density of the image, from where we estimate the image as the most probable instance, given the measured data. Furthermore, we assess the uncertainty present in the image estimate, by means of random sampling from the posterior density. As a most important property of BASE-CT, the statistical framework allows us to augment the qualitative data with quantitative information to compensate for the paucity of data. We include this a priori knowledge in a hierarchical construction of the prior density function; controlling it by effectively adapting a hyperprior as part of the image estimation.

Our tests on phantom data show that BASE-CT performs remarkably better than the classic tomographic reconstruction methods FBP and ART. In comparison to TV regularization, we see a slight improvement in the ability to capture the most detailed image structures. The potential of the method is demonstrated in connection with two tasks from industrial imaging in abattoirs. The accurate measurements of relevant information from the reconstructed images exhibit a high degree of certainty. A robust and fast image acquisition scheme with low running cost is of primary interest for automation in the high throughput en-

vironment of the abattoir. In this context, our results appear very promising, opening up for efficiently combining the BASE-CT reconstruction from sparse projection data with a stationary scanner set-up.

Chapter 10

Can Anisotropic Images Be Upsampled?

Mads Fogtmann Hansen, Thomas Hammershaimb Mosbech, Hildur Ólafsdóttir, Michael Sass Hansen and Rasmus Larsen

Abstract

This paper presents a novel method for upsampling anisotropic medical gray-scale images. The resolution is increased by fitting an image function, modeled by cubic B-splines, to the slices. The method simulates the observed slices with an image function and iteratively updates the function by comparing the simulated slices with observed slices. The approach handles partial voluming by modeling the thickness of the slices. The formulation is ill-posed, and thus a prior needs to be included. Correspondences between adjacent slices are established using a symmetric registration method with a free-form deformation model. The correspondences are then converted into a prior that penalizes gradients along lines of correspondence. Tests on the Shepp-Logan phantom show promising results, and the approach performs better than methods such as cubic interpolation and one-way registration-based interpolation.

10.1 Introduction

Image interpolation plays an important role in many medical image analysis applications by closing the gap between the true continuous nature of an image and the practical discrete representation of an image. Uniform tensor splines

(UTS), e.g. tricubic interpolation, is the method of choice for most applications due to the regular sampling of discrete images. A potential problem with this approach is the inherent assumption of a smooth transition between neighboring voxels.

The idea of *registration-based interpolation* was introduced as a solution to the problem [94]. Here, correspondences between neighboring slices are determined by one-way registrations in 2D. The interpolation is then performed along these lines of correspondence to achieve a smooth transition, rather than using the usual lateral neighborhood.

The method was extended by utilizing both a forward and backward registration — a weighted sum of two non-symmetric displacement fields — for the interpolation [38].

Recently, [89] proposed a method to improve the method even further. The paper presents an interpolation based on weighting both intensity and deformation by the inter-slice distance of the interpolation point. The method combines both a forward and backward interpolation into a less time-consuming algorithm in comparison to [94] by using an approximation to the inverse deformation, while still reporting sufficiently accurate results.

The quality of registration-based interpolation is highly dependent on the quality of the correspondences obtained. This can be somewhat questionable as there may not exist a one-to-one mapping between adjacent slices. That is, structures may disappear between two slices, and in these situations one must rely on the *nice* behavior of the chosen registration scheme. Another previously untouched problem in registration-based interpolation is the partial volume effect; image artifacts occurring as part of the image digitalization, where images are formed by slices of thick volumetric blocks rather than infinitely thin 2D planes.

As an alternative to the common registration-based interpolation we propose fitting a *parametric function* to the thick slices, accounting for the partial volume effect by incorporating the thickness of a slice. Furthermore, we use symmetric registration between adjacent slices to form a prior to stabilize the ill-posed problem.

As the idea behind the method is to identify the underlying image rather than interpolating the thick slice voxels, we say the method *upsamples* the anisotropic image under reasonable constraints.

10.2 Methods

The goal of our method is to obtain a better approximation of the true 3D image R given a slice-based representation defined by the set of K slices $\{S^1, S^2, \ldots, S^K\}$. Here, a slice is a 2D planar view of a 3D image integrated over a given thickness. That is, the expected value of the (i, j)th voxel of the kth slice image S^k_{ij} is given by

$$E[S^k_{ij}|R] = \int_{V_{ij}} R(\boldsymbol{x})dv, \tag{10.1}$$

where V_{ij} is the volume element covered by the (i, j)th voxel. When this volume contains a mixture of multiple tissue values, the partial volume effect occurs. This is particularly evident for thicker slices — images with more anisotropic voxels.

10.2.1 Upsampling Strategy

Our strategy for upsampling is to iteratively update an approximation $\tilde{R}$ of the true image R by comparing the current approximation with the observed slices. To do this we formulate the quality of match as

$$\mathcal{M}[\tilde{R}, \{S^k\}_{k=1\ldots K}] = \sum_{k=1}^{K}\sum_{i=1}^{M}\sum_{j=1}^{N} m(E[S^k_{ij}|\hat{R}], S^k_{ij}), \tag{10.2}$$

where $m(\cdot)$ is a measure of similarity between voxels in the observed and simulated slices. Here, we use cubic B-splines as the parametric representation of $\tilde{R}$

$$\tilde{R}(\boldsymbol{x}, \boldsymbol{p}) = \langle \boldsymbol{b}(x_3) \otimes \boldsymbol{b}(x_2) \otimes \boldsymbol{b}(x_1), \boldsymbol{p} \rangle, \tag{10.3}$$

where $\boldsymbol{p}$ are the image parameters, and $\boldsymbol{b}$ are the B-splines. The most suitable measure of similarity is dependent on the underlying noise model of the data. For intensities in magnetic resonance images (MRI) with a high signal-to-noise ratio, the noise is approximately Gaussian [45]. Thus, assuming i.i.d. the squared difference in intensities optimally defines the similarity between observation and simulation

$$m(E[S^k_{ij}|\hat{R}], S^k_{ij}) = (E[S^k_{ij}|\hat{R}] - S^k_{ij})^2. \tag{10.4}$$

Given this parametric representation of $\tilde{R}$, it is possible to obtain a continuous representation of R by minimizing (10.2) with respect to the parameters. This can reduce the partial volume effect. Unfortunately, the minimization is unlikely to produce a better approximation to the true R as the problem is ill-posed.

Thus, more information needs to be added in order to solve the problem properly. We seek to handle this this by including a prior $\mathcal{S}$ in the cost function. That is, a new approximation $\tilde{R}$ is obtained by solving

$$\min_{\tilde{R}} \mathcal{M}[\tilde{R}, \{S^k\}_{k=1\ldots K}] + \beta \mathcal{S}_{\boldsymbol{v}}[\tilde{R}], \tag{10.5}$$

where the coefficient β governs the effect of the prior.

In this work, we specifically consider a penalty term that penalizes high image gradients in certain directions. We write the prior as the inner product between the gradient image and a vector field $\boldsymbol{v}$, i.e.

$$\mathcal{S}_{\boldsymbol{v}}[\tilde{R}] = \int_{\Omega} \langle \nabla \tilde{R}(\boldsymbol{x}), \boldsymbol{v}(\boldsymbol{x}) \rangle^2 d\boldsymbol{x}, \tag{10.6}$$

That is, $\boldsymbol{v}$ determines the direction and magnitude of the penalty — resulting in less regularization where the two are approximately orthogonal and/or of low magnitude. We call $\boldsymbol{v}$ the *penalization vector field*. The following section presents a procedure for constructing this vector field.

10.2.2 Constructing a Penalization Vector Field

Inspired by [38, 89, 94] we obtain the penalization vector field by non-rigid registration of neighboring slices. We apply a symmetric registration between slices, assuming that the point $\boldsymbol{\phi}_1(\boldsymbol{x}) = \boldsymbol{x} - \boldsymbol{u}(\boldsymbol{x})$ in slice S^1 corresponds to the point $\boldsymbol{\phi}_2(\boldsymbol{x}) = \boldsymbol{x} + \boldsymbol{u}(\boldsymbol{x})$ in slice S^2. The concept is illustrated in figure 10.1. The penalization vector field is then composed by a half slice thickness τ, the displacement $\boldsymbol{u}$ and a scale factor γ

$$\boldsymbol{v}(\boldsymbol{x}) = \gamma(\boldsymbol{x}) \frac{[\tau,\ \boldsymbol{u}(\boldsymbol{x})]^{\mathrm{T}}}{\| [\tau,\ \boldsymbol{u}(\boldsymbol{x})]^{\mathrm{T}} \|}. \tag{10.7}$$

The squared difference similarity measure drives the registration as we assume that intensities in adjacent slices are directly comparable, and that the noise is i.i.d., i.e.

$$\mathcal{D}[S^1, S^2; \boldsymbol{u}] = \int_{\Omega} \left(S^2 \circ \boldsymbol{\phi}_2(\boldsymbol{x}) - S^1 \circ \boldsymbol{\phi}_1(\boldsymbol{x}) \right)^2 d\boldsymbol{x}, \tag{10.8}$$

with $S^i(\boldsymbol{\phi}_i(\boldsymbol{x})) = S^i \circ \boldsymbol{\phi}_i(\boldsymbol{x})$.

The free-form deformation model [102] is used to model the deformation $\boldsymbol{u}$ in order to reduce the dimensionality of the problem. Hence,

$$\boldsymbol{u}(\boldsymbol{x}; \boldsymbol{w}) = \langle \boldsymbol{b}(x_2) \otimes \boldsymbol{b}(x_1), \boldsymbol{w} \rangle, \tag{10.9}$$

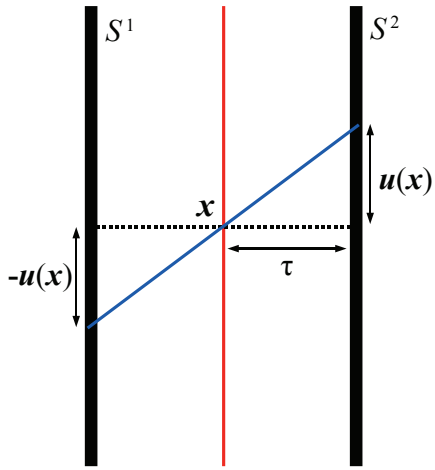

Figure 10.1: Illustration of slice registration setup and direction of penalization vector field

where $\boldsymbol{w}$ are the deformation parameters, and $\boldsymbol{b}$ are the B-splines.

To ensure a homeomorphic deformation we adapt the Riemannian elasticity energy [93] in the registration process. The elasticity energy of a deformation field $\boldsymbol{\phi}$ is given by

$$\mathcal{S}_{rie}(\boldsymbol{\phi}) = \int_{\Omega} \mu \ \mathrm{tr}(\boldsymbol{E}_0(\boldsymbol{x})^2) + \frac{\lambda}{2}\mathrm{tr}(\boldsymbol{E}_0(\boldsymbol{x}))^2 d\boldsymbol{x} \tag{10.10}$$

where $\boldsymbol{E}_0 = \frac{1}{2}\log((\boldsymbol{I} + \nabla\boldsymbol{\phi})^T(\boldsymbol{I} + \nabla\boldsymbol{\phi}))$ is the Hencky strain tensor.

Thus, correspondences between adjacent slices are identified by solving

$$\min_{\boldsymbol{w}} \mathcal{D}[S^1, S^2; \boldsymbol{u}] + \alpha(\mathcal{S}_{rie}(\boldsymbol{\phi}_1) + \mathcal{S}_{rie}(\boldsymbol{\phi}_2)), \tag{10.11}$$

where α determines the amount of regularization introduced by the elasticity term.

Homogeneous areas in the image (e.g. background) contain no information to guide the registration. Therefore, one should be cautious when putting great confidence in the local correspondences estimated here. To address this issue we introduce an information score e for each registration point. This is included by means of the scale factor γ of the penalization vector field (10.7).

We base e on the edge information available in the slice around each position, as edges *within* slices are valuable in the registration. For a point $\boldsymbol{x}$ we filter

around the position in the two neighboring image slices $\boldsymbol{\phi}_1(\boldsymbol{x})$ and $\boldsymbol{\phi}_2(\boldsymbol{x})$ with the first order derivative of a 1D Gaussian kernel [20]

$$G'_\sigma(x)\frac{\partial G_\sigma(x)}{\partial x} = \frac{-x}{\sigma}\frac{1}{\sigma\sqrt{2\pi}}\exp -\frac{x^2}{2\sigma^2}. \tag{10.12}$$

The kernel covers n pixels on each side of the pixel and has a standard deviation of $\sigma = n/3$.

The score is then computed as the absolute value of the sum of the two

$$e(\boldsymbol{x}) = \left|G'_\sigma * \left(S^1 \circ \boldsymbol{\phi}_1(\boldsymbol{x})\right) + G'_\sigma * \left(S^2 \circ \boldsymbol{\phi}_2(\boldsymbol{x})\right)\right|. \tag{10.13}$$

This means that both slices must contain edge information around the matching point in order for the correspondence to be regarded as strong.

The scale factor is then computed as the score divided by a parameter ϵ plus the similarity measure of (10.8)

$$\gamma(\boldsymbol{x}) = \frac{e(\boldsymbol{x})}{\epsilon + \left(S^2 \circ \boldsymbol{\phi}_2(\boldsymbol{x}) - S^1 \circ \boldsymbol{\phi}_1(\boldsymbol{x})\right)^2}. \tag{10.14}$$

where the value of ϵ is related to the intensity level of the image. As mentioned earlier, the penalization vector field is then constructed by multiplying the correspondence directions from the registration by these scale factors.

10.3 Experiments

In this section we present a study in 2D comparing our proposed upsampling approach using the prior of the penalization vector field (UPWP) against the standard cubic interpolation (CI) [66] and the one-way registration-based interpolation (RBI) [94]. For reference we also include a reconstruction performed using our method without the prior (UPNP).

From a 250×250 isotropic-sampled Shepp-Logan phantom [106] we create a downsampled anisotropic image by averaging every five columns together. Figures 10.2(a,b) show the isotropic and anisotropic phantom. That is, the columns act as the thick slices in the context described in the previous section. Figure 10.2(c) displays the registration-based line correspondences superimposed on the anisotropic phantom. For the registration the knot spacing of the B-splines was four pixels and the regularization weight was 10^{-2}. A penalization vector field was extracted from the registration. The columns were filtered using

(a) Phantom

(b) Downsampled phantom

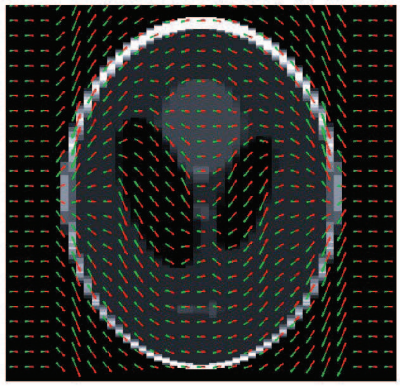

(c) Downsampled phantom with correspondences from the registration

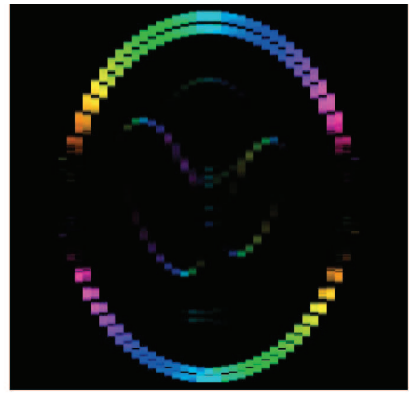

(d) Penalization vector field

(e) Color-map for penalization vector field field. The color shows the direction and the brightness shows the magnitude.

Figure 10.2: Visualization of phantom data, symmetric registration and the penalization vector field.

	CI	RBI	UPNP	UPWP
MSE	0.0143	0.0073	0.0080	0.0045

Table 10.1: Mean squared error between reconstructions and isotropic phantom for the four reconstruction methods.

the derivative of a 1D Gaussian kernel with standard deviation $\frac{5}{3}$. The resulting field is displayed in Figure 10.2(d).

Four reconstructions were obtained from the anisotropic-sampled phantom using CI, RBI and our UPNP and UPWP without and with the penalization vector field shown in Figure 10.2(d). Figure 10.3 contains these reconstructions. For quantitative comparison we computed the mean squared error (MSE) between pixel values in the isotropic-generated phantom and the reconstructions. Table 10.1 lists the results. From Figure 10.3 and Table 10.1 we acknowledge that UPWP provides the most visually pleasing result as well as the lowest MSE. Finally, we see from Figure 10.3(b) that the RBI approach provides visually nice interpolation in areas with good registration, and unsatisfactory interpolation in areas lacking correspondences — areas where structures runs approximately parallel to the slices. This problem and the method's ability to recover from partial volume effects of the upsampling approach explain the lower MSE of our UPWP.

10.4 Conclusion

This paper presented a novel approach for improving the resolution of anisotropic medical images. The method relies on a prior constructed upon registrations of neighboring slices. As such, the quality of the prior is undoubtedly dependent on the quality of the registrations. However, unlike the registration-based interpolation method, it is possible to limit the effect of mis-registrations by reducing the length of the penalization vector field in areas with little information or poor fit.

The preliminary tests presented in the paper showed promising results, motivating further investigation and validation.

(a) Cubic interpolation

(b) One-way registration [94]

(c) Upsampling without prior

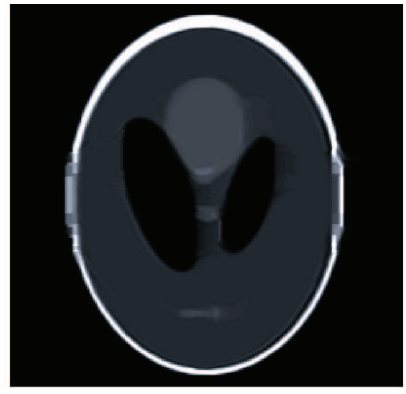

(d) Upsampling with prior

Figure 10.3: Reconstructions

List of Figures

Bibliography

[1] H.O. Altamar, R.E. Ong, C.L. Glisson, D.P. Viprakasit, M.I. Miga, S.D. Herrell, and R.L. Galloway. Kidney Deformation and Intraprocedural Registration: A Study of Elements of Image-Guided Kidney Surgery. *Journal of Endourology*, 25(3):511–517, March 2011.

[2] I. Amenabar, A. Mendikute, A. López-Arraiza, M. Lizaranzu, and J. Aurrekoetxea. Comparison and analysis of non-destructive testing techniques suitable for delamination inspection in wind turbine blades. *Composites Part B: Engineering*, 2011.

[3] J. Ashburner and K.J. Friston. Nonlinear spatial normalization using basis functions. *Human brain mapping*, 7(4):254–266, 1999.

[4] J. Ashburner, C. Hutton, R. Frackowiak, I. Johnsrude, C. Price, and K. Friston. Identifying global anatomical differences: deformation-based morphometry. *Human Brain Mapping*, 6(5-6):348–357, 1998.

[5] Danish Meat Association. History. http://danishmeat.eu/DMRI/About_DMRI/History.aspx. (Accessed April 2011).

[6] S.G. Azevedo, H.E. Martz, and D.J. Schneberk. Potential of computed tomography for inspection of aircraft components. In *Proceedings of SPIE, Nondestructive Inspection of Aging Aircraft*, volume 2001, pages 47–57, 1993.

[7] J.M. Bardsley, D. Calvetti, and E. Somersalo. Hierarchical regularization for edge-preserving reconstruction of PET images. *Inverse Problems*, 26(035010):035010, 2010.

[8] EC Beckmann. CT scanning the early days. *British journal of radiology*, 79(937):5–8, 2006.

[9] M. Bertero and P. Boccacci. *Introduction to inverse problems in imaging*. IOP Publishing, 1998.

[10] B.T. Bethea, A.M. Okamura, M. Kitagawa, T.P. Fitton, S.M. Cattaneo, V.L. Gott, W.A. Baumgartner, and D.D. Yuh. Application of haptic feedback to robotic surgery. *Journal of Laparoendoscopic & Advanced Surgical Techniques*, 14(3):191–195, 2004.

[11] Å. Bjlörck. *Numerical methods for least squares problems*. Society for Industrial Mathematics, 1996.

[12] Per Black. Millimeterpræcis afsværing af svinekamme med robot. *Danish Meat Association, Ny viden om slagteri og forædling*, 2, April 2009.

[13] F.L. Bookstein. Principal warps: Thin-plate splines and the decomposition of deformations. *Pattern Analysis and Machine Intelligence, IEEE Transactions on*, 11(6):567–585, 1989.

[14] C.V.C. Bouten. Literature review in behalf of the research project Etiology of pressure sores, conducted by the department of Computational and Experimental Mechanics of the Eindhoven University of Technology, in co-operation with the department of Movement Sciences of the University of. Technical report, Department of Computational and Experimental Mechanics, Eindhoven University of Technology, 1996.

[15] D.M. Brienza, P.E. Karg, and C.E. Brubaker. Seat cushion design for elderly wheelchair users based on minimization of soft tissue deformation using stiffness and pressure measurements. *Rehabilitation Engineering, IEEE Transactions on*, 4(4):320–327, 1996.

[16] H. Busk, E.V. Olsen, and J. Brøndum. Determination of lean meat in pig carcasses with the autofom classification system. *Meat Science*, 52(3):307 – 314, 1999.

[17] D. Calvetti and E. Somersalo. *Introduction to Bayesian scientific computing: Ten lectures on subjective computing*. Springer Verlag, 2007.

[18] D. Calvetti and E. Somersalo. Hypermodels in the Bayesian imaging framework. *Inverse Problems*, 24:034013, 2008.

[19] D. Calvetti and E. Somersalo. Subjective knowledge or objective belief? an oblique look to Bayesian methods. In *Proceedings of Sandia CSRI Workshop on Large-Scale Inverse Problems and Quantification of Uncertainty*. John Wiley & Sons, 2009.

[20] J. Canny. A computational approach to edge detection. *IEEE Transactions Pattern Analysis and Machine Intelligence*, 8(6):679–698, 1986.

[21] Carometec Food Technology. AutoFom – Fully Automatic Ultrasonic Carcass Grading for Pork Slaughterhouses. www.carometec.com.

[22] Y. Chen, D. Gao, C. Nie, L. Luo, W. Chen, X. Yin, and Y. Lin. Bayesian statistical reconstruction for low-dose X-ray computed tomography using an adaptive-weighting nonlocal prior. *Computerized Medical Imaging and Graphics*, 33(7):495–500, 2009.

[23] T. F. Cootes, D. H. Cooper, C. J. Taylor, and J. Graham. Active shape models – their training and application. *Computer Vision and Image Understanding*, 61(1):38–59, December 1995.

[24] A. M. Cormack. Representation of a function by its line integrals, with some radiological applications. *Journal of Applied Physics*, 34(9):2722–2727, sep 1963.

[25] A. M. Cormack. Representation of a function by its line integrals, with some radiological applications. ii. *Journal of Applied Physics*, 35(10):2908–2913, oct 1964.

[26] N. Cressie. The origins of kriging. *Mathematical Geology*, 22(3):239–252, 1990.

[27] S. De, Y.J. Lim, M. Manivannan, and M.A. Srinivasan. Physically realistic virtual surgery using the point-associated finite field (PAFF) approach. *Presence: Teleoperators and Virtual Environments*, 15(3):294–308, 2006.

[28] H. Delingette, X. Pennec, L. Soler, J. Marescaux, and N. Ayache. Computational models for image-guided robot-assisted and simulated medical interventions. *Proceedings of the IEEE*, 94(9):1678–1688, 2006.

[29] S. G. H. Erbou. *Modeling the Biological Diversity of Pig Carcasses*. PhD thesis, Technical University of Denmark, 2008.

[30] S. G. H. Erbou and B. K. Ersbøll. From ct to shape model. Technical report, Technical University of Denmark, 2008.

[31] S.G.H. Erbou, M. Vester-Christensen, R. Larsen, L.B. Christensen, and B.K. Ersbøll. Comparison of sparse point distribution models. *Machine Vision and Applications*, pages 1–10, 2010.

[32] N. Famaey and J. V. Sloten. Soft tissue modelling for applications in virtual surgery and surgical robotics. *Computer Methods in Biomechanics and Biomedical Engineering*, 11(4):351–366, August 2008.

[33] J.M. Fitzpatrick, J.B. West, and C.R. Maurer Jr. Predicting error in rigid-body point-based registration. *Medical Imaging, IEEE Transactions on*, 17(5):694–702, 1998.

[34] P. Folkmann. Innovation and advanced technology behind a new machine for automatic cutting of pork middles. Danish Meat Association, http://danishmeat.eu/DMRI/Automation/Carcass_cutti/Publications/Innovation_an.aspx. (Accessed April 2011).

[35] Agriculture & Food. Statistics pigmeat 2009, June 2010.

[36] M. Fornefett, K. Rohr, and H. S. Stiehl. Elastic Registration of Medical Images using Radial Basis Functions with Compact Support. *Proceedings of the IEEE Computer Society Conference on Computer Vision and Pattern Recognition, 1999*, 1:402–407, 1999.

[37] M. Fornefett, K. Rohr, and H. S. Stiehl. Radial basis functions with compact support for elastic registration of medical images. *Image and Vision Computing*, 19:87–96, 2001.

[38] D. Frakes, L. Dasi, K. Pekkan, H. Kitajima, K. Sundareswaran, A. Yoganathan, and M. Smith. A New Method for Registration-based Medical Image Interpolation. *IEEE Transactions on Medical Imaging*, 27(3):370–377, 2008.

[39] P. E. Frandsen, K. Jonasson, H. B. Nielsen, and O. Tingleff. *Unconstrained optimization*. Informatics and Mathematical Modellingm Technical University of Denmark, 2004.

[40] L. Frederiksen, K. Højlund, D. M. Hougaard, T. H. Mosbech, R. Larsen, A. Flyvbjerg, J. Frystyk, K. Brixen, and M. Andersen. Testosterone therapy decreased subcutaneous fat and adiponectin in ageing men. *European Journal of Endocrinology*, 2011. (Manuscript submitted, March 2011).

[41] S. Geman and D. Geman. Stochastic relaxation, Gibbs distributions, and the Bayesian relation of images. *IEEE Transactions on Pattern Analysis and Machine Intelligence*, 6:721–741, 1984.

[42] C.L. Gilchrist, J.Q. Xia, L.A. Setton, and E.W. Hsu. High-Resolution Determination of Soft Tissue Deformations Using MRI and First-Order Texture Correlation. *IEEE Transactions on Medical Imaging*, 23(5), 2004.

[43] B. Godske. Slagterirobot skal skære lige til benet (in danish). *Ingeniøren — Produktion*, 6 June 2008.

[44] R. Gordon, R. Bender, and G.T. Herman. Algebraic Reconstruction Techniques (ART) for three-dimensional electron microscopy and X-ray photography. *Journal of theoretical Biology*, 29(3):471–481, 1970.

[45] H. Gudbjartsson and S. Patz. The Rician Distribution of Noisy MRI Data. *Magnetic Resonance in Medicine*, 34(6):910–914, 1995.

[46] F. Hansen. Round cutting of hind legs. Danish Meat Association, http://danishmeat.eu/DMRI/Automation/Boning/Publications/Round_cutting.aspx.

[47] M. F. Hansen, T. H. Mosbech, H. Olafsdottir, and R. Larsen. Can anisotropic images be upsampled? In *5th International Conference on Computer Vision Theory and Applications, VISAPP*, 2010.

[48] M.F. Hansen. *The virtual knife*. PhD thesis, Technical University of Denmark, 20089.

[49] M.F. Hansen, L.B. Christensen, and R. Larsen. Virtual cutting atlas. Technical report, Technical University of Denmark, 2008.

[50] M.F. Hansen and R. Larsen. Validation of virtual cuts. Technical report, Technical University of Denmark, 2008.

[51] M.S. Hansen, R. Larsen, B. Glocker, and N. Navab. Adaptive parametrization of multivariate b-splines for image registration. In *Computer Vision and Pattern Recognition, 2008. CVPR 2008. IEEE Conference on*, pages 1–8. IEEE, 2008.

[52] P.C. Hansen. *Discrete inverse problems: insight and algorithms*. Society for Industrial Mathematics, 2010.

[53] L. Hinrichsen. Manufacturing technology in the Danish pig slaughter industry. *Meat science*, 84(2):271–275, 2010.

[54] G.N. Hounsfield. Computerized transverse axial scanning (tomography): Part 1. Description of system. *British Journal of Radiology*, 46(552):1016, 1973.

[55] R.D. Howe and Y. Matsuoka. Robotics for surgery. *Annual Review of Biomedical Engineering*, 1(1):211–240, 1999.

[56] T. Hsiao, A. Rangarajan, and G. Gindi. Joint-MAP Bayesian tomographic reconstruction with a gamma-mixture prior. *Image Processing, IEEE Transactions on*, 11(12):1466–1477, Dec 2002.

[57] T. Hu. *Reality-based soft tissue probing: experiments and computational model for application to minimally invasive surgery*. PhD thesis, Drexel University, 2006.

[58] Y. Hu, L. Xie, L. Luo, J.C. Nunes, and C. Toumoulin. L0 constrained sparse reconstruction for multi-slice helical CT reconstruction. *Physics in Medicine and Biology*, 56:1173, 2011.

[59] A. Hyvarinen. Survey on independent component analysis. *Neural Computing Surveys*, 2(4):94–128, 1999.

[60] S. A. Jackson, R. M. Thomas, and S. N. Harrison. *Cross-sectional imaging made easy*. Churchill Livingstone, 2005.

[61] S. Kaczmarz. Angenäherte auflösung von systemen linearer gleichungen. *Bull. Int. Acad. Polon. Sci. A*, 355:357, 1937.

[62] J.P. Kaipio and E. Somersalo. *Statistical and computational inverse problems*. Springer Verlag, 2005.

[63] H. Kaiser. The varimax criterion for analytic rotation in factor analysis. *Psychometrika*, 23:187–200, 1958.

[64] A. C. Kak and M. Slaney. *Principles of Computerized Tomographic Imaging*. IEEE Press, New York, 1988.

[65] W. Kalender. *Computed Tomography: Fundamentals, System Technology, Image Quality, Applications*. Publicis Corporate Publishing, 2nd edition, 2005.

[66] R. G. Keys. Cubic Convolution Interpolation for Digital Image Processing. *IEEE Transactions on Acoustics Speech and Signal Processing*, 29(6):1153–1160, 1981.

[67] N. C. Kjærsgaard. *Optimization of the Raw Material Use at Danish Slaughterhouses*. PhD thesis, Technical University of Denmark, 2008.

[68] D.G. Krige. A statistical approach to some basic mine valuation and allied problems on the Witwatersrand. *Journal of the Chemical, Metallurgical and Mining Society of South Africa*, 1951.

[69] H. W. Kuhn. The hungarian method for the assignment problem. *Naval Research Logistics Quarterly*, 2:83–97, 1955.

[70] U. Kuhnapfel, H.K. Cakmak, and H. Maass. Endoscopic surgery training using virtual reality and deformable tissue simulation. *Computers & Graphics*, 24(5):671–682, 2000.

[71] F. Liang, C. Liu, and R. J. Carroll. *Advanced Markov Chain Monte Carlo Methods: Learning from Past Samples*. John Wiley & Sons, 2010.

[72] D. Lim, F. Lin, R.W. Hendrix, B. Moran, C. Fasanati, and M. Makhsous. Evaluation of a new sitting concept designed for prevention of pressure ulcer on the buttock using finite element analysis. *Medical and Biological Engineering and Computing*, 45(11):1079–1084, 2007.

[73] J. A. Little, D. L. G. Hill, and D. J. Hawkes. Deformations Incorporating Rigid Structures. *Computer Vision and Image Understanding*, 66(2):223–232, 1997.

[74] J. S. Liu. *Monte Carlo strategies in scientific computing*. Springer Verlag, 2008.

[75] K. B. Madsen and J. U. Nielsen. *Meat processing: Improving quality*, chapter 14. Woodhead, 2002.

[76] MATLAB. *version 7.9.0 (R2009b)*. The MathWorks Inc., Natick, Massachusetts, 2009.

[77] T. H. Mosbech, D. Calvetti, E. Somersalo, L. B. Christensen, and B. K. Ersbø ll. Base ct: Bayesian adaptive structure enriched computed tomography. *SIAM Journal on Imaging Sciences*, 2011. (Manuscript submitted, April 2011).

[78] T. H. Mosbech, B. K. Ersbø ll, and L. B. Christensen. An efficient data-driven tissue deformation model. In *Computer Vision Workshops (ICCV Workshops), 2009 IEEE 12th International Conference on*, pages 1771–1777, 2009.

[79] T. H. Mosbech, B. K. Ersbøll, and L. B. Christensen. Quantification and validation of soft tissue deformation. In X. P. Hu and A. V. Clough, editors, *SPIE Medical Imaging 2009: Biomedical Applications in Molecular, Structural, and Functional Imaging*, volume 7262, page 72621D. SPIE, 2009.

[80] T. H. Mosbech, K. Pilgaard, A. Vaag, and R. Larsen. Automatic segmentation of abdominal adipose tissue in MRI. In *Proceedings of the 17th Scandinavian Conference on Image Analysis, SCIA*, volume 6688 of *Lecture Notes in Computer Science*, pages 501–511. Springer, 2011.

[81] F. Natterer. *The mathematics of computerized tomography*. Society for Industrial Mathematics, 2001.

[82] F. Natterer and F. Wubbeling. *Mathematical methods in image reconstruction*. Society for Industrial Mathematics, 2001.

[83] J. U. Nielsen. Automation in pig slaughtering, cutting and boning. Danish Meat Association, http://danishmeat.eu/DMRI/Automation/Slaughterline/Publications/13633Automati.aspx (Accessed April 2011).

[84] P.M. Nissen, H. Busk, M. Oksama, M. Seynaeve, M. Gispert, P. Walstra, I. Hansson, and E. Olsen. The estimated accuracy of the EU reference dissection method for pig carcass classification. *Meat Science*, 73(1):22–28, 2006.

[85] A.M. Okamura. Methods for haptic feedback in teleoperated robot-assisted surgery. *Industrial Robot: An International Journal*, 31(6):499–508, 2004.

[86] H. Ólafsdóttir. *Analysis of Craniofacial Images using Computational Atlases and Deformation Fields*. PhD thesis, Technical University of Denmark, 2008.

[87] H. Ólafsdóttir, T.A. Darvann, B.K. Ersbø ll, N.V. Hermann, E. Oubel, R. Larsen, A.F. Frangi, P. Larsen, C.A. Perlyn, G.M. Morriss-Kay, and S. Kreiborg. Craniofacial statistical deformation models of wild-type mice and Crouzon mice. *Proceedings of SPIE Medical Imaging 2007: Image Processing*, 2007.

[88] H. Ólafsdóttir, M. Hansen, K. Sjöstrand, T. Darvann, N. Hermann, E. Oubel, B. Ersbø ll, R. Larsen, A. Frangi, P. Larsen, C. A. Perlyn, G. M. Morriss-Kay, and S. Kreiborg. Sparse statistical deformation model for the analysis of craniofacial malformations in the crouzon mouse. In *Proceedings of the 17th Scandinavian Conference on Image Analysis, SCIA*, volume 4522 of *Lecture Notes in Computer Science*, pages 112–121. Springer, 2007.

[89] H. Ólafsdóttir, H. Pedersen, M. S. Hansen, M. Lyksborg, S. Darkner, and R. Larsen. Registration-based Interpolation Applied to Cardiac MR. *Proceedings of SPIE Medical Imaging 2010: Image Processing*, 2010.

[90] E. V. Olsen. Den nye AutoFOM DK sikrer mere præcis kødprocentmåling og sortering (in danish). *Danish Meat Association, Ny viden om slagteri og forædling*, 2, April 2009.

[91] C. W. J. Oomens, O. F. J. T. Bressers, E. M. H. Bosboom, C. V. C. Bouten, and D. L. Bader. Can loaded interface characteristics influence strain distributions in muscle adjacent to bony prominences? *Computer Methods in Biomechanics and Biomedical Engineering*, 6(3):171–180, July 2003.

[92] F. Peeters, B. Jr Verbeeten, and H.W. Venema. Nobel Prize for medicine and physiology 1979 for A.M. Cormack and G.N. Hounsfield. *Nederlands Tijdschrift Voor Geneeskunde*, 123(51):2192–2193, Dec 1979.

[93] X. Pennec, R. Stefanescu, V. Arsigny, P. Fillard, and N. Ayache. Riemannian Elasticity: A Statistical Regularization Framework for Nonlinear Registration. *Proceedings of the 8th International Conference on Medical Image Computing and Computer-Assisted Interventation (LNCS)*, 3750:943–950, 2005.

[94] G. Penney, J. Schnabel, D. Rueckert, M. Viergever, and W. Niessen. Registration-based Interpolation. *IEEE Transactions on Medical Imaging*, 21(7):922–926, 2004.

[95] K. Pilgaard, T. H. Mosbech, L. Grunnet, H. Eiberg, E. Vallentin G. Van Hall, T. Larsen, R. Larsen, P. Poulsen, and A. Vaag. Differential non-genetic impact of birth weight versus 3rd trimester growth velocity on glucose metabolism and abdominal adiposity as determined by magnetic resonance imaging in young healthy twins. *Journal of Clinical Endocrinology & Metabolism, JCEM*, 2011.

[96] T. Poulsen. Svineproducenter går deres egne vej (in danish). *FoodCulture*, 9, 2005.

[97] G. Purnell. Robotic equipment in the meat industry. *Meat Science*, 49(Supplement 1):S297 – S307, 1998. Meat Consumption and Culture 44th International Congress of Meat Science and Technology.

[98] J. Radon. Über die Bestimmung von Funktionen durch ihre Integralwerte längs gewisser Mannigfaltigkeiten. *Berichte Sächsische Akademie der Wissenschaften, Leipzig, Mathematisch-Physikalische Klasse*, 69:262–277, 1917.

[99] R. Rangayyan, A.P. Dhawan, and R. Gordon. Algorithms for limited-view computed tomography: an annotated bibliography and a challenge. *Applied optics*, 24(23):4000–4012, 1985.

[100] R.M. Rangayyan. *Biomedical Image Analysis*. CRC, 2005.

[101] D. Rueckert, A.F. Frangi, and J.A. Schnabel. Automatic construction of 3-D statistical deformation models of the brain using nonrigid registration. *Medical Imaging, IEEE Transactions on*, 22(8):1014–1025, 2003.

[102] D. Rueckert, L. I. Sonoda, C. Hayes, D. L. G. Hill, M. O. Leach, and D. J. Hawkes. Nonrigid Registration using Free-Form Deformations: Application to Breast MR Images. *IEEE Transactions on Medical Imaging*, 18(8):712–21, 1999.

[103] D. Rueckert, LI Sonoda, C. Hayes, D.L.G. Hill, M.O. Leach, and D.J. Hawkes. Nonrigid registration using free-form deformations: application to breast MR images. *Medical Imaging, IEEE Transactions on*, 18(8):712–721, 1999.

[104] K. Sandberg and J. G. Salin. Liquid water absorption in dried Norway spruce timber measured with CT scanning and viewed as a percolation process. *Wood Science and Technology*, 2010.

[105] D.L. Schmoldt, L.G. Occena, A.L. Abbott, and N.K. Gupta. Nondestructive evaluation of hardwood logs: CT scanning, machine vision and data utilization. *Nondestructive Testing and Evaluation*, 15(5):279–309, 1999.

[106] L. A. Shepp and B. F. Logan. The Fourier reconstruction of a head section. *IEEE Transactions on Nuclear Science*, 21(3):21–43, 1974.

[107] E.Y. Sidky, C.M. Kao, and X. Pan. Accurate image reconstruction from few-views and limited-angle data in divergent-beam CT. *Journal of X-Ray Science and Technology*, 14(2):119–139, 2006.

[108] S. Siltanen, V. Kolehmainen, S. Järvenpää, JP Kaipio, P. Koistinen, M. Lassas, J. Pirttilä, and E. Somersalo. Statistical inversion for medical x-ray tomography with few radiographs: I. General theory. *Physics in Medicine and Biology*, 48:1437, 2003.

[109] J. L. Skytte. Estimation of fat layer thickness profiles in carcass midsections. Master's thesis, Technical University of Denmark, 2010.

[110] D. Stoyanov, A. Darzi, and G.Z. Yang. Dense 3D depth recovery for soft tissue deformation during robotically assisted laparoscopic surgery. *Medical Image Computing and Computer-Assisted Intervention–MICCAI 2004*, pages 41–48, 2004.

[111] N. Suzuki, A. Hattori, T. Ezumi, A. Uchiyama, T. Kumano, A. Ikemoto, Y. Adachi, and A. Takatsu. Simulator for virtual surgery using deformable organ models and force feedback system. *Studies in health technology and informatics*, 50:227–333, 1998.

[112] M. Tada, N. Nagai, and T. Maeno. Material properties estimation of layered soft tissue based on MR observation and iterative FE simulation. *Medical Image Computing and Computer-Assisted Intervention–MICCAI 2005*, pages 633–640, 2005.

[113] C. Then, J. Mengera, G. Benderotha, M. Alizadehd, T. J. Vogla, F. Hubnera, and G. Silbera. Analysis of mechanical interaction between human gluteal soft tissue and body supports. *Technology and Health Care*, 16:61–67, 2008.

[114] J. Troccaz. Computer and Robot-Assisted Medical Intervention. *Springer Handbook of Automation*, pages 1451–1466, 2009.

[115] M. Vester-Christensen, S.G.H. Erbou, M.F. Hansen, E.V. Olsen, L.B. Christensen, M. Hviid, B.K. Ersbøll, and R. Larsen. Virtual dissection of pig carcasses. *Meat Science*, 81(4):699–704, 2009.

[116] M. Vester-Christension. *Image Registration and Optimization in the Virtual Slaughterhouse*. PhD thesis, Technical University of Denmark, 2008.

[117] M. P. Wachowiak, X. Wang, A. Fenster, and T. M. Peters. Compact support radial basis functions for soft tissue deformation. In *ISBI*, pages 1259–1262. IEEE, 2004.

[118] I. Wadie, N. Maddock, G. Purnell, K. Khodabandehloo, A. Crooks, A. Shacklock, and D. West. Robots for the meat industry. *Industrial Robot: An International Journal*, 22(5):22–24, 1995.

[119] H. Wendland. Piecewise polynomial, positive definite and compactly supported radial functions of minimal degree. *Advances in Computational Mathematics*, 4(1):389–396, December 1995.

[120] J. Zhang, G. Yang, Y. Cheng, B. Gao, Q. Qiu, YZ Lee, JP Lu, and O. Zhou. Stationary scanning x-ray source based on carbon nanotube field emitters. *Applied Physics Letters*, 86:184104, 2005.

[121] J. Zhang, G. Yang, YZ Lee, S. Chang, JP Lu, and O. Zhou. Multiplexing radiography using a carbon nanotube based x-ray source. *Applied physics letters*, 89:064106, 2006.

[122] H. Zou, T. Hastie, and R. Tibshirani. Sparse principal component analysis. *Journal of computational and graphical statistics*, 15(2):265–286, 2006.